UNIVERSITE PARIS-SUD XI
FACULTÉ DES SCIENCES D'ORSAY

MEMOIRE

pour l'obtention de
L'HABILITATION A DIRIGER DES RECHERCHES

Top Quark Precision Measurements with the D0 Detector

présentée par
Viatcheslav Sharyy

Soutenue le 29 janvier 2015 devant le jury

Prof. W. Bernreuther	(rapporteur)
Dr. M. Besançon	(examinateur)
Dr. A-I. Etienvre	(examinateur)
Dr. E. Kajfasz	(rapporteur)
Dr. A. Lucotte	(rapporteur)
Prof. A. Stocchi	(examinateur)

Introduction

For 24 years the Tevatron proton-antiproton collider was the collider with the highest collision energy in the world. It was in operation from 1988 to 1996 with a center-of-mass energy of 1.8 TeV (Run I) and after numerous upgrades from 2002 to September 2011 with a center-of-mass energy of 1.98 TeV (Run II). Two collaborations, D0 and CDF, exploited the Tevatron facility and realized a vast physics program. The principal directions of this program are the Higgs boson search, search for non-standard phenomena, precise measurement of W boson mass, heavy flavor physics, QCD and top quark physics. One of the main Tevatron achievements is the discovery in 1995 of the heaviest known elementary particle, the top quark. From 1995 and up to now, both, D0 and CDF collaborations, have studied the top quark in great detail.

This manuscript describes my 11 years research in the D0 experiment. In the beginning of the Run II data taking period, my main contribution was the operation of the D0 calorimeter, development of the calorimeter on-line monitoring software, an extensive study of the external and internal sources of noise and development of the system of the data quality monitoring and selection [1]. Another important contribution to experiments with the D0 detector was the work on the off-line treatment of data events prior to the physics analysis. It particular, I contributed to the development of the common analysis environment, used to select and process events in the standard and certified way by most of the physics analysis at D0 [2]. In addition to my personal contribution, I participated in the design, planning and coordination of this activity as a convener of the common samples physics group in 2007—2009 and V+jets group in 2009—2010. The activity related to the detector operation and to the development of the common analysis environment is described in chapter 1.

In 2004 I started studies of the top quark, mainly in the dilepton final state. In particular, I worked on the selection and separation of top quark-antiquark ($t\bar{t}$) events from the background events, the $t\bar{t}$ production cross-section measurement, [3–7], search for non SM decays of the top quark, e.g. search for a charged higgs boson, [7], measurement of the ratio of the branching fractions, [8]. With increase in the integrated luminosity, the precise measurement of the top quark properties became possible: the measurement of the top quark mass, [9], asymmetry in the angular distributions of the top quark, [10, 11]. In addition, I am involved in the coordination of the top quark group activity, development of the analyses strategy, presentations and publications of results, combinations of the Tevatron measurements, as a dilepton subgroup convener in 2007 – 2009 and as a top group convener from 2011 and up to now. These studies and results of the measurements are presented in the chapter 2.

My current D0 activity is focused on publishing the legacy measurements at the Tevatron: $t\bar{t}$ asymmetry, the spin correlation strength, measurement of the top quark mass in the dilepton channel, measurement of $t\bar{t}$ production cross section.

Bibliography

[1]V. Shary, "Data quality monitoring for the D0 calorimeter", Proceedings of 11th International Conference on Calorimetry in High-Energy Physics, Perugia, Italy, 205–209 (2004).

[2]V. Shary, "Computing tools and analysis architecture: The Tevatron experience", Nucl. Phys. Proc. Suppl. **177-178**, 18th Hadron Collider Physics Symposium 2007 (HCP 2007), 121–125 (2008).

[3]V. Abazov et al., "Measurement of the $t\bar{t}$ production cross-section in $p\bar{p}$ collisions using dilepton events", Phys. Rev. **D76**, 052006 (2007), arXiv:`0706.0458 [hep-ex]`.

[4]V. Abazov et al., "Measurement of the $t\bar{t}$ production cross section and top quark mass extraction using dilepton events in $p\bar{p}$ collisions", Phys.Lett. **B679**, 177–185 (2009), arXiv:`0901.2137 [hep-ex]`.

[5]V. Abazov et al., "Combination of $t\bar{t}$ cross section measurements and constraints on the mass of the top quark and its decays into charged Higgs bosons", Phys. Rev. **D80**, 071102 (2009), arXiv:`0903.5525 [hep-ex]`.

[6]V. M. Abazov et al., "Measurement of the $t\bar{t}$ production cross section using dilepton events in $p\bar{p}$ collisions", Phys.Lett. **B704**, 403–410 (2011), arXiv:`1105.5384 [hep-ex]`.

[7]T. A. Aaltonen et al., "Combination of measurements of the top-quark pair production cross section from the Tevatron Collider", Phys. Rev. **D89**, 072001 (2014), arXiv:`1309.7570 [hep-ex]`.

[8]V. Abazov et al., "Precision measurement of the ratio $\mathrm{B}(t \to Wb)/\mathrm{B}(t \to Wq)$ and Extraction of V_{tb}", Phys. Rev. Lett. **107**, 121802 (2011), arXiv:`1106.5436 [hep-ex]`.

[9]V. M. Abazov et al., "Precise measurement of the top quark mass in the dilepton channel at D0", Phys. Rev. Lett. **107**, 082004 (2011), arXiv:`1105.0320 [hep-ex]`.

[10]V. M. Abazov et al., "Measurement of the asymmetry in angular distributions of leptons produced in dilepton $t\bar{t}$ final states in $p\bar{p}$ collisions at $\sqrt{s}$=1.96 TeV", Phys.Rev. **D88**, 112002 (2013), arXiv:`1308.6690 [hep-ex]`.

[11]V Abazov et al., "Measurement of forward-backward asymmetry in $p\bar{p} \to t\bar{t}$ production in the dilepton final states using a matrix element technique", D0 Conference Note 6445 (2014).

Contents

1 Tools for the precision measurements **7**
1.1 D0 detector . . . 7
1.1.1 D0 Calorimeters . . . 7
1.2 Calorimeter Data Quality . . . 13
1.2.1 Calorimeter On-line Monitoring. . . . 13
1.2.2 Off-line Calorimeter Data Quality Checks . . . 14
1.2.3 The Calorimeter Data Quality Strategy . . . 17
1.3 Common Analysis Tools . . . 20
1.3.1 Data handling . . . 20
1.3.2 Physics Analysis . . . 20

2 Top Quark Studies **25**
2.1 Introduction . . . 25
2.2 Events Selection . . . 28
2.2.1 Object Identification . . . 28
2.2.2 Events Selection . . . 29
2.2.3 Estimation of the $t\bar{t}$ Efficiency and Background Contribution . . . 30
2.3 Cross Section Measurements . . . 34
2.4 Matrix Element Method . . . 38
2.5 Mass Measurement . . . 43
2.6 Asymmetry . . . 53
2.6.1 Introduction . . . 53
2.6.2 Asymmetry in Lepton Distributions . . . 54
2.6.3 Asymmetry in Distribution of Top Quark . . . 57
2.6.4 Overview and discussion . . . 59

Conclusion **73**

Chapter 1

Tools for the precision measurements

1.1 D0 detector

The D0 experiment was proposed in 1983 to study the $p\bar{p}$ collisions at the center-of-mass energy of 1.8 TeV. Between 1992 and 1996 the D0 detector [1] was used for numerous studies including the top quark search, discovery and measurement of the top quark mass [2, 3]. This period is usually referred by the Tevatron community as the Run I. After the end of the data taking the essential upgrade of the Tevatron complex has been undertaken. In the same time the D0 detector also has been upgraded to take advantage of the Tevatron increased energy of 1.96 TeV and a higher instantaneous luminosity [4]. From 2001 and up to 2011 (so-called Run II) the Tevatron reached the instantaneous luminosity of $4.3 \cdot 10^{32}$ cm^{-2}s^{-1} and delivered more than 11 fb^{-1} of integrated luminosity for each experiment (Fig. 1.1).

The D0 detector, Fig. 1.2, is a typical particle physics detector made of a several sub-detectors. The central-tracking system is used to measure the transverse momentum (p_T) of charged particles. It consists of a silicon microstrip tracker and a central fiber tracker, both located within a 2 T superconducting solenoidal magnet, with designs optimized for tracking and vertexing at pseudorapidities[1] $|\eta_{\text{det}}| < 3$ and $|\eta_{\text{det}}| < 2.5$, respectively. A liquid-argon and uranium calorimeter measures the energy of charged and neutral particles. It has a central section covering pseudorapidities $|\eta_{\text{det}}|$ up to ≈ 1.1, and two end calorimeters that extend the coverage to $|\eta_{\text{det}}| \approx 4.2$, with all three housed in separate cryostats. An outer muon system, at $|\eta_{\text{det}}| < 2$, is used for the muon identification. it constructed from layers of tracking detectors and scintillation trigger counters in front of 1.8 T toroid, followed by two similar layers after the toroid. A schematic view of the detector is shown in Figure 1.2.

1.1.1 D0 Calorimeters

The D0 calorimeters [4, 5] were designed to work in the absence of the magnetic field for the Run I of the Tevatron. The calorimeters themselves are unchanged from Run I, [1], see Fig. 1.3. The central calorimeter (CC) covers $|\eta_{\text{det}}| \lesssim 1.1$ and the two end-cap calorimeters (EC), north and south, extend the coverage to $|\eta_{\text{det}}| \lesssim 4$. Each calorimeter contains an electromagnetic (EM) section closest to the interaction region followed by fine

[1] In the following η_{det} denotes detector pseudorapidity defined as $\eta_{\text{det}} = -\ln(\tan\frac{\theta}{2})$, where θ is the polar angle relative to the center of the detector. η denotes pseudorapidity of the particle, defined as $\eta = -\ln(\tan\frac{\theta_{PV}}{2})$, where the polar angle of the particle θ_{PV} is calculated relative to the primary vertex of the event.

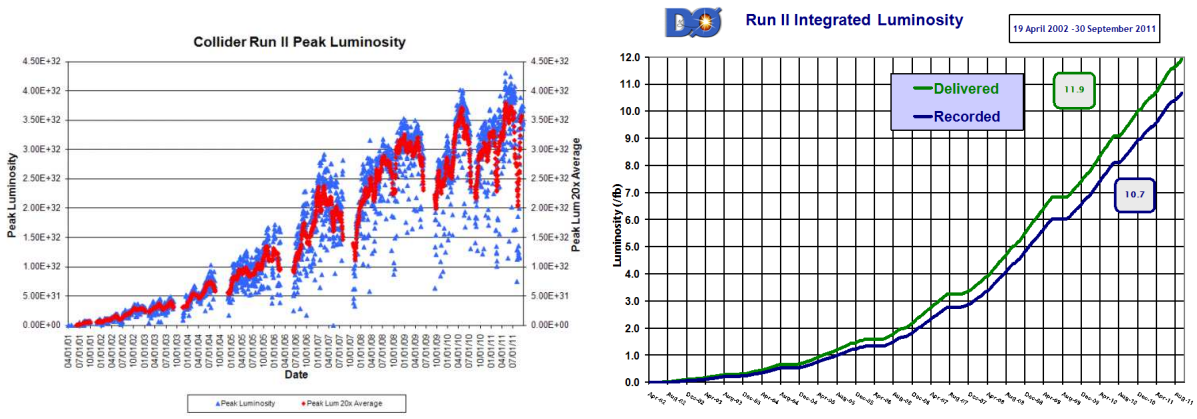

(a) Instantaneous luminosity (b) Integrated luminosity

Figure 1.1: Tevatron luminosity as a function of time.

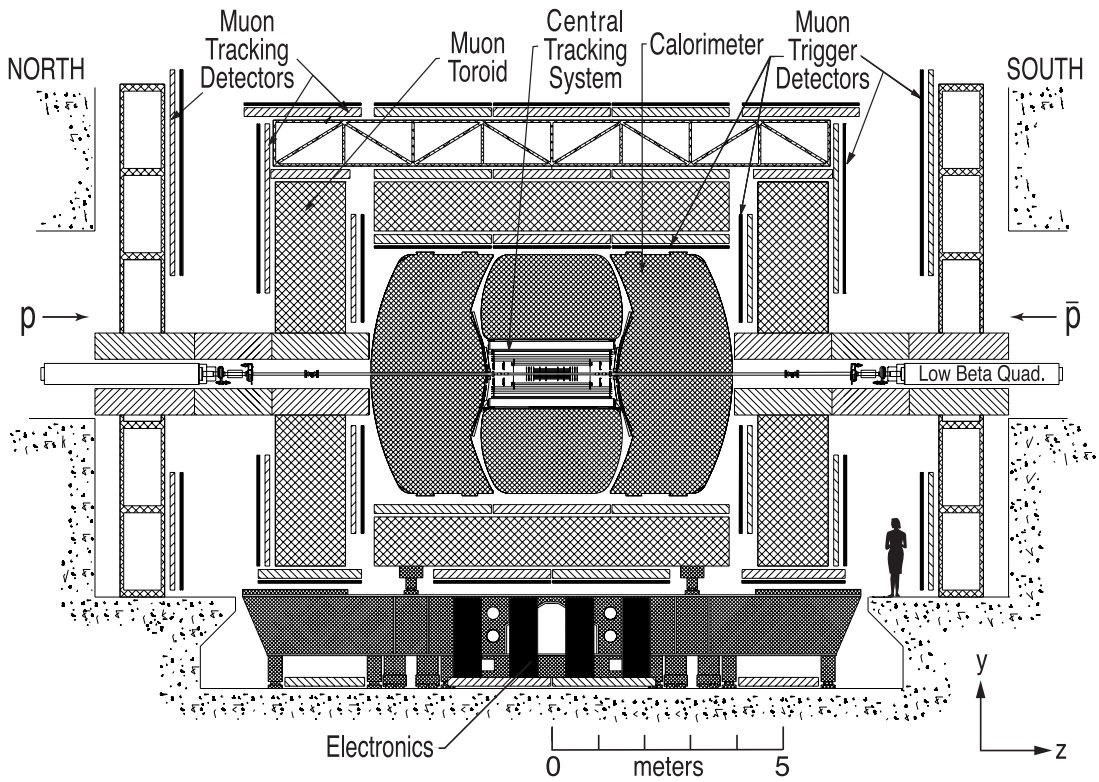

Figure 1.2: D0 detector.

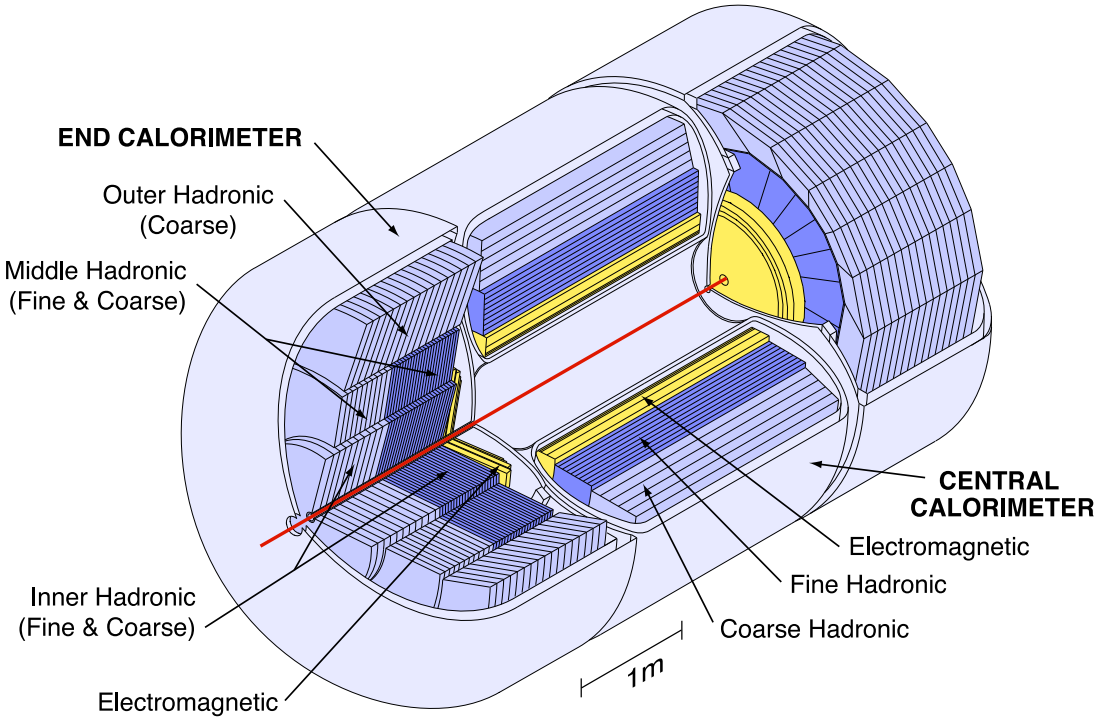

Figure 1.3: D0 calorimeters.

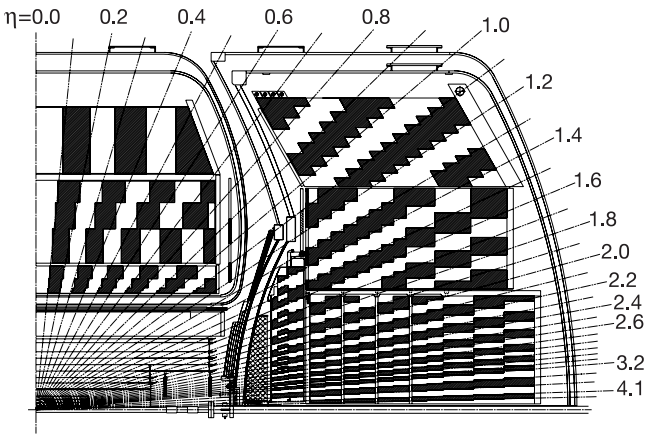

Figure 1.4: D0 calorimeter layers structure.

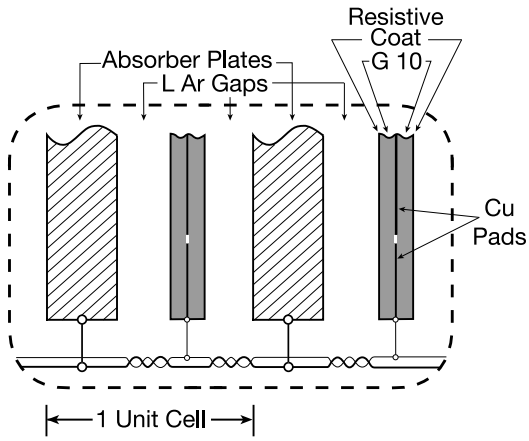

Figure 1.5: Schematic view of the calorimeter cell.

and coarse hadronic sections.

Different absorber plates are used in different locations. The EM sections use thin plates (3 or 4 mm in the CC and EC, respectively), made from nearly pure depleted uranium. The fine hadronic sections are made from 6-mm-thick uranium-niobium 2% alloy. The coarse hadronic modules contain relatively thick (46.5 mm) plates of copper (in the CC) or stainless steel (EC). The schematic view of a calorimeter cell is shown in Fig. 1.5. The typical electric field is about +2.0 kV, applied to the resistive surfaces of the signal boards, while the metal absorber plates are connected to ground. The electron drift time across the 2.3 mm liquid argon gap is approximately 450 ns. Calorimeter readout cells form pseudo-projective towers as shown in Fig. 1.4, with each tower subdivided in depth. There are four separate depth layers for the EM modules in the CC and EC. The layers thickness are approximately 1.4, 2.0, 6.8, and $9.8X_0$[2]. in CC and approximately 1.6, 2.6, 7.9, and $9.3X_0$ in EC. The amount of material before the first EM layer is about $4.0X_0$

[2] X_0 stands for radiation (electromagnetic) interaction length.

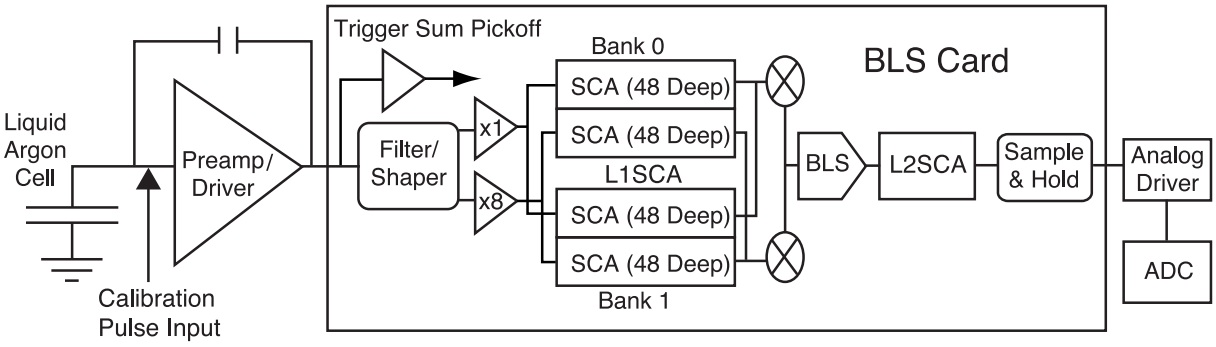

Figure 1.6: Readout chain of the D0 calorimeter.

at $\eta_{\rm det} = 0$ and about $4.4X_0$ at $\eta_{\rm det} = 2.0$. The thickness of the fine hadronic modules in CC is about 1.3, 1.0, and $0.76\lambda_I$[3] and about $3.2\lambda_I$ for a single CC coarse hadronic module. In the inner EC module, four fine hadronic layers have the thickness of about $1.1\lambda_I$ and the coarse hadronic part is $4.1\lambda_I$. In the middle EC module, four fine hadronic layers have the thickness of about $0.9\lambda_I$ and the coarse hadronic one is $4.4\lambda_I$. The outer hadronic EC modules are made from stainless steel plates, the maximum thickness is $6.0\lambda_I$. The transverse sizes of the readout cells are comparable to the transverse sizes of showers: 1.2 cm for EM showers and about 10 cm for hadronic showers. Towers in both EM and hadronic modules are $\Delta\eta_{\rm det} = 0.1$ and $\Delta\phi = 2\pi/64 \approx 0.1$. The third EM layer is located at the EM shower maximum and is segmented twice as finely in both $\eta_{\rm det}$ and ϕ to allow more precise location of EM shower centroids.

There are 47 032 calorimeter electronic channels to be read out. The readout contains three mains components: charge preamplifiers located on the cryostats, baseline subtractor and storage circuitry (BLS) and analog-to-digital converters (ADC), see Fig. 1.6. The signal from the readout chain then enters the data acquisition system for the Level 3 trigger decision and storage to tape. Electron drift time across the 2.3 mm liquid-argon gap remains approximately 450 ns at 2.0 kV for Run II, which provides a challenge for signal charge integration with beam crossings occurring every 396 ns. The calorimeter electronics were designed to maintain the good signal-to-noise ratio in the high instantaneous luminosity environment of the original Tevatron Run II design, with a minimum bunch crossing time of 132 ns.

The signals after preamplification are routed from the calorimeter over approximately 25 m of twisted-pair cable to the BLSs located below the cryostats. The BLSs use switched capacitor arrays (SCA) as analog storage devices to hold the signal for about 4 μs until the Level 1 trigger decision is made, and for an additional 2 μs until the Level 2 trigger decision is made. They also provide a baseline subtraction to remove any low-frequency noise or pileup from the signal. In addition, faster shaped analog sums of the signals are picked off to provide prompt inputs to the calorimeter trigger system for both the Level 1 and Level 2 calorimeter trigger decisions. To minimize the effects of pile-up[4], only two-thirds of the charge collected by the preamplifier circuit, corresponding to the first 260 ns of signal collection from the gap, is used in the shaper circuit. Shaped signals are sampled every 132 ns. To subtract the baseline, the signal earlier by 396 ns is subtracted by the BLS circuitry. Only cells with a signal of 1.5 times the standard deviation of the electronic noise after baseline subtraction are read out from the calorimeter. This defines the on-line zero suppression mode of the calorimeter readout or "1.5σ zero suppression".

[3] λ_I stands for nuclear interaction length.

[4] Pile-up means that more than one event in the detector are registered either in a single beam crossing due to multiple interactions or in multiple beam crossings.

For further processing, cells with a signal at least 2.5 times the standard deviation of the electronic noise are kept in nominal conditions of data taking (so-called "T42 procedure"). This defines the off-line zero suppression mode or "2.5σ zero suppression".

A BLS board processes signals from the 48 channels from four pseudo-projective calorimeter towers. Each tower corresponds to up to 12 preamplifier signals. There are signal shapers for each channel on the BLS motherboard, and trigger pick-off and summation circuits tap the preamplifier signal prior to the shaper circuitry. The shaped preamplifier signals are fed to daughterboards, one per tower, each of which holds five SCA chips. The SCAs contain an array of 48 capacitors to pipeline the calorimeter signals. The SCA is not designed for simultaneous read/write operations, therefore, two SCA banks are alternately employed to provide the capability to write and read the integrated charges. This scheme provides the 4.2 μs buffering necessary prior to the arrival of the Level 1 trigger decision. There are also two gain paths ($\times 1$ and $\times 8$) to extend the ADC readout dynamic range, thus four of the SCAs are used to store the signals for the 12 channels on a daughtercard until the Level 1 trigger decision has been made. Once a positive Level 1 decision is received, the baseline subtractor circuitry on each daughterboard decides channel by channel which gain path to use and subtracts the stored baseline from the peak signal. It then stores the result in the Level 2 SCA that buffers the data until a Level 2 trigger decision has been made. Once a Level 2 trigger accept is issued, the data are transferred to the ADC across 130 m of twisted-pair cables. The gain information is sent simultaneously on separate digital control cables.

The calorimeter calibration system consists of 12 identical units for the calorimeter. Each unit is composed of one pulser board and its power supply and six active fanout boards. The pulser boards are controlled via a VME I/O register to set the amplitude and the timing of the calibration signal and to enable the channels to be pulsed. A TTL command signal opens one of the 16 switches on a fanout board producing a calibration signal which has been chosen to be close to the triangular shape of a physics signal with a rise time of about 25 ns, falling exponentially with a time constant of approximately 200 ns. Both the pulser board and the active fanout have been shown to provide a pulser signal with a linearity at the per mil level. All of the currents delivered are uniform within 0.2% for all boards and 0.1% within a board. All of the pulse shapes have been measured to estimate systematic effects on the signal amplitude, the timing, and the charge injected. The study of the calorimeter electronics using pulser data shows saturation effects of the SCA chips at the low and high ends of their dynamic range. To correct for these non-linear effects, a universal function has been derived, which is an effective parametrization of the non-linearity induced by the Level 1 and Level 2 trigger SCA chips. After correcting all channels, we measure a linearity of 0.6% (0.4%) FWHM at an equivalent cell energy of 5 GeV(50 GeV) read out from the $\times 8$ ($\times 1$) gain path .

Examples of the final calorimeter performance are shown in Fig. 1.7 for the jet energy resolution, and in Fig. 1.8 for the invariant mass resolution of two electrons in $Z/\gamma^\star \to ee$ process. The constant terms of the EM calorimeter is $C_{EM} = 2.00 \pm 0.07\%$, as determined in [6] and the electron energy resolution is found to be around 3.4% for electrons with an energy of 40 GeV and $\eta = 0.0$.

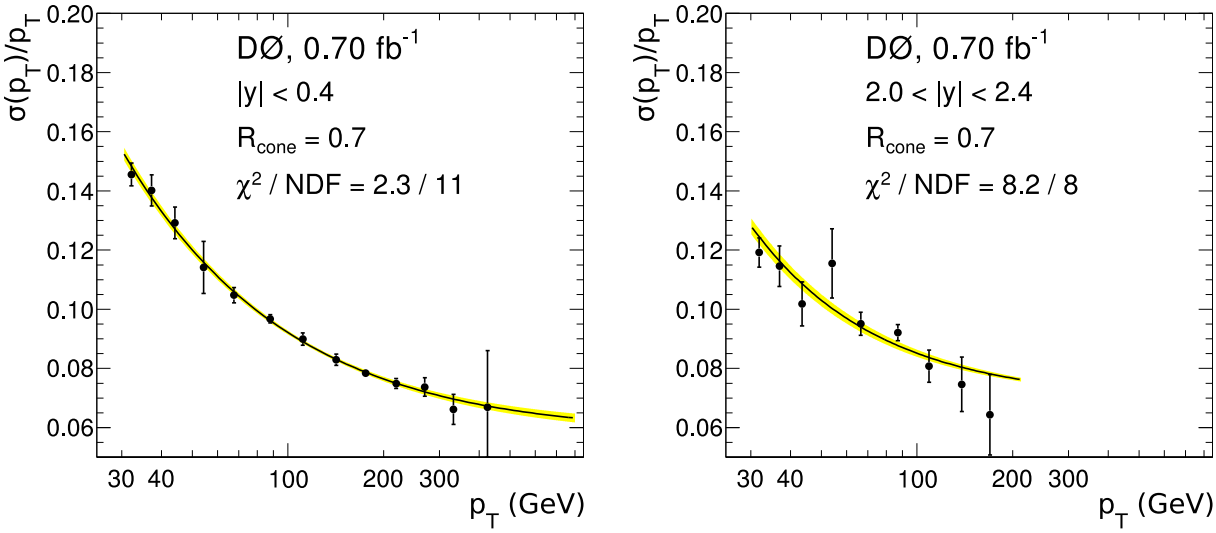

Figure 1.7: Jet energy resolution in data as a function of the jet p_T, in two different rapidity ranges, for jets with the reconstruction cone size of $R = \sqrt{\Delta\eta^2 + \Delta\phi^2} = 0.7$, [6]

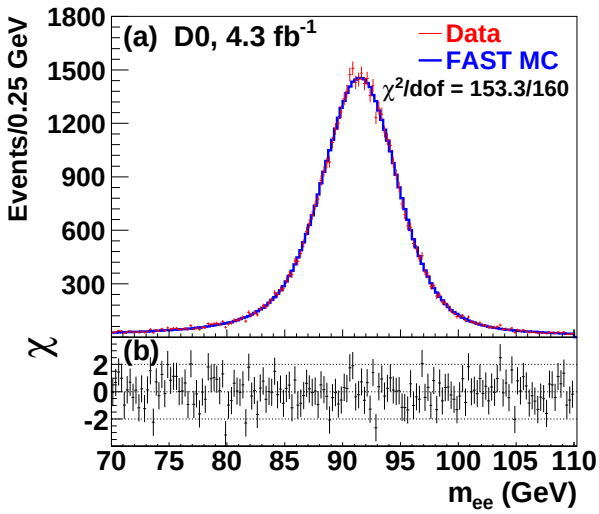

Figure 1.8: The invariant mass of two electrons as reconstructed in the $Z/\gamma^\star \to ee$ events, [7].

1.2 Calorimeter Data Quality

Operation of any detector is unavoidable accompanied by different failures, especially in the beginning of its operation. For the D0 calorimeter, failures could be divided into the following categories.

- Failure of the low voltage or high voltage supply. This makes part of the detector insensitive to the energy deposition, and results in an additional non-efficiency in the detector operation.
- Readout failure. It may manifest itself in many different ways, depending on the failure. Several problems have been identified, namely: hot cells, hot towers, coherent pedestal shift in ADC, checker board patterns, SCA failure, etc.
- External noise problems.

To ensure the high quality of the data collected with the D0 calorimeter we developed the strategy which consists of two parts: the on-line control of the data taking and off-line control and corrections during event processing.

1.2.1 Calorimeter On-line Monitoring.

The essential part of the on-line control is the calorimeter monitoring software. We developed such a software, which was in every-day use from 2004 up to the very end of the D0 data taking in September 2011. The developed program [8] consists of two main parts: an event collector and a graphical user interface (GUI). The event collector connects to the event distributor, saves the selected event parameters to root trees and verifying data quality. The monitoring GUI monitors the energy deposition in all calorimeter cells, makes the on-line graphical maps, visualizes the calorimeter energy deposition maps, builds the related histograms and reports about the quality of the collected events. It also compares signals from two independent readouts: precision readout and trigger readout, and reports any disagreement in the measured values to the shifter. A snapshot of the on-line monitoring program is shown in Fig. 1.9.

Monitoring is one of the most important tasks of the detector operation. The complete detector control needs a large number of histograms (several hundreds for the calorimeter alone). The person on shift is not expected to monitor all these histograms. To reduce the load on a shifter, less than 20 histograms are used during the shift, and the on-line monitoring program is equipped with automatic data quality control. The data quality is checked periodically during the data taking every 200 events. The calorimeter problems mostly affect the jets triggers and triggers based on the EM objects, therefore 4 different data streams are used for the monitoring with a typical storing rate of 4 Hz (10% of the total events to tape rate): zero bias stream, stream with unsuppressed events, stream with events selected by jets triggers, stream with events selected by all other physics triggers, prescaled by a factor of ten. The different data quality checks include: monitoring of the noise rate for each stream using the event based flags from the corresponding identification program (see section 1.2.2), search for towers (EM or hadronic) without signal (manifestation of the power supply failure), monitoring cells or towers for an unusually large signal and/or unusually large occupancy. The results of the monitoring is used to identify the bad runs and luminosity block[5] and saves the

[5]Luminosity block is the smallest logical unit for the luminosity calculation at DO. The duration of a luminosity block is near 1 min. It contains 2500 recorded events on average. The integrated luminosity is near 1 nb^{-1} per block.

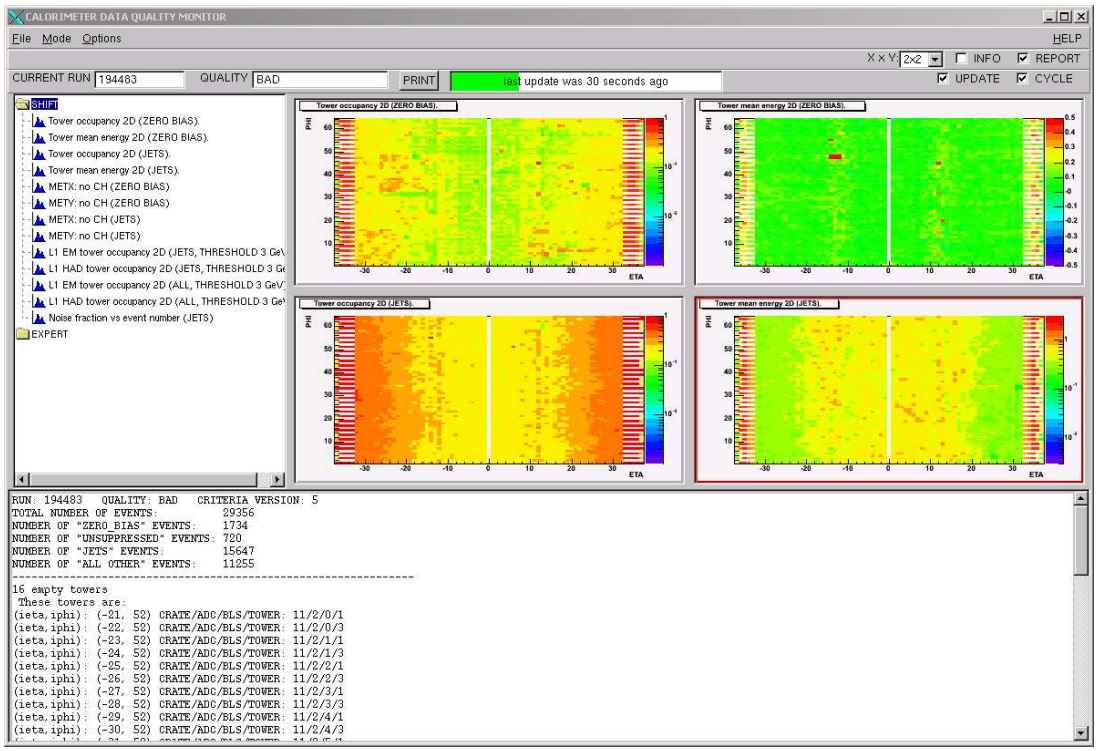

Figure 1.9: A snapshot of the on-line monitoring program for the D0 calorimeter.

corresponding markers in the off-line data quality run database. This database is used in the off-line processing to discard the portion of events with a bad data quality.

1.2.2 Off-line Calorimeter Data Quality Checks

Off-line data quality verification is used to identify any possible failure in the detector operation after on-line checks. This verification is done in several steps. At the first step, two algorithms are used to clean-up the calorimeter energy deposition map. "NADA" algorithm [9] removes isolated cells with a signal in each event, i.e. cells with energy deposition of more than 1 GeV when all neighbour cells don't have any significant energy deposition. This algorithm was initially designed to remove signals from the uranium radioactive decays, but was found to be also useful to remove cells with readout electronic failures, so-called "hot cells".

"T42" algorithm [9] was designed to reduce the influence of external noise and improve resolution in missing transverse energy. This algorithm removes all cells with negative signals[6] and retains only cells with high (more than 4σ) signal and their neighbours with signals between 2.5 and 4σ, where σ is RMS of the electronic noise, measured individually for each channel.

One of the most challenging problems in running the D0 calorimeter is to have good understanding and control over any noise sources which might affect the performance of the calorimeter. During Run II operation, we identified several sources of noise. Once identified, noisy events could be either eliminated from the data set or flagged so that they could be used to estimate the inefficiency due to the data quality selection in the analysis. We developed a dedicated noise and electronics failure identification software, used in the on-line monitoring and off-line data processing. The following problems are considered:

[6]The negative signals could appear because of the analogous base line subtraction from the previous interaction.

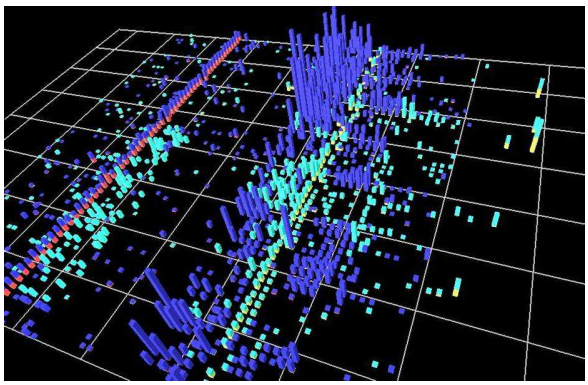

Figure 1.10: A typical "ring of fire" event. The x and y axes are η and ϕ axes of calorimeter. Z axis is an absolute value of the calorimeter EM towers signal in ADC counts. Positive cell signals are indicated in red and negative in blue.

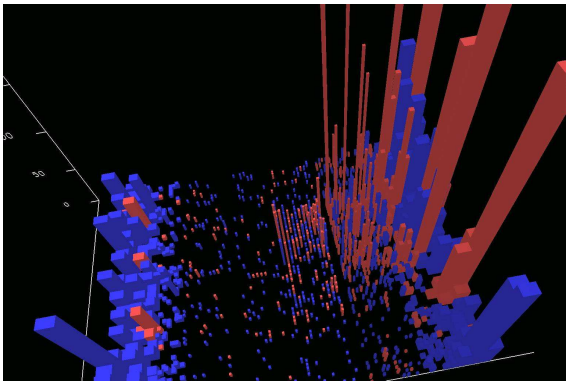

Figure 1.11: A typical "noon noise" event. EM layer 3 is shown. The x and y axes are η and ϕ axes of calorimeter. Z axis is an absolute value of the signals in ADC counts. Positive cell signals are indicated in red and negative in blue.

The "missing crate" problem is a readout problem when the information from one or several ADCs is missing in the event. To detect this problem the occupancy in each crate is calculated. This problem can also be detected using the error word from the ADCs in the calorimeter information chunk. The typical rate of such events is near 0.5%. Such events are removed from the analysis data set. The reduction in efficiency are calculated using the zero bias events[7].

The "ring of fire" noise is an external noise in the calorimeter. Its name originated in the fact that it affects all channels at a given depth in one of the two EC cryostats at the outer edge of the EM module in either layer 3 or 4. Due to the limited space in the inter-cryostat region the high voltage distribution layout for the EM layers is built as a ring electrode. That is why the external noise picked up by this electrode affect all ϕ, see a typical event in Fig. 1.10. The natural criterion for this noise is the number of cells fired in the corresponding rings of EM layer 4. This noise typically affects all events during the noisy spike, so the chosen corrections strategy is to remove the affected luminosity block. The "ring of fire" noise occurred often before the summer shutdown in 2003. During this shutdown a special search allowed to identify the noise origin (the cable to a cryostat temperature sensor) and to remove it. After the shutdown the noise was detected only in special situations: during the solenoid noisy period and when welding in the D0 assembling building was happening.

The name "noon noise" is due to the fact that the noise has often appeared around noon (lunch time) and ended by dinner time. This noise is characterized by large positive and large negative energies in calorimeter cells and affects a large fraction of cells, as it is shown in Fig. 1.11. The online monitoring software clearly indicates that the noisy region is limited to the boundaries of several calorimeter readout crates. While the signal in a single cell is not that large, when summed over a large region of the calorimeter it completely compromises the jet and missing E_T reconstruction. It was found that this noise also correlated with the use of a welding machine in the D0 assembly building. After improving the calorimeter grounding, mainly by removing the accidental shorts to the ground, this noise has disappeared. A study was performed in order to find a suitable parameter to separate the noisy events. The occupancy of the readout crates turned out

[7]Zero Bias events are triggered by the beam crossing tick only. No energy deposition or track presence are required in the detector.

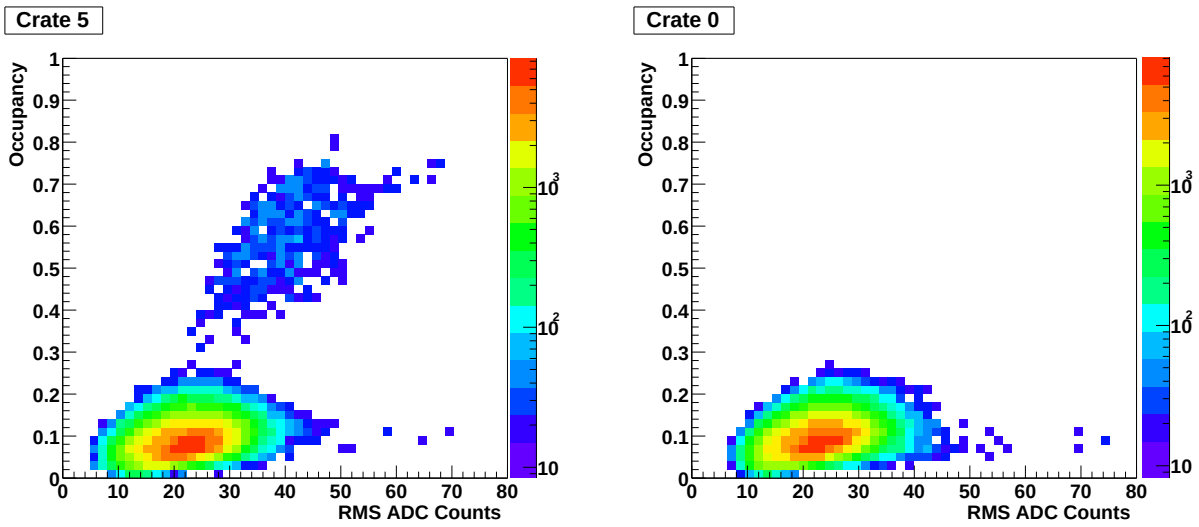

Figure 1.12: On the left (right) the occupancy versus the RMS of ADC counts in crate 5, with noise (crate 0, without noise).

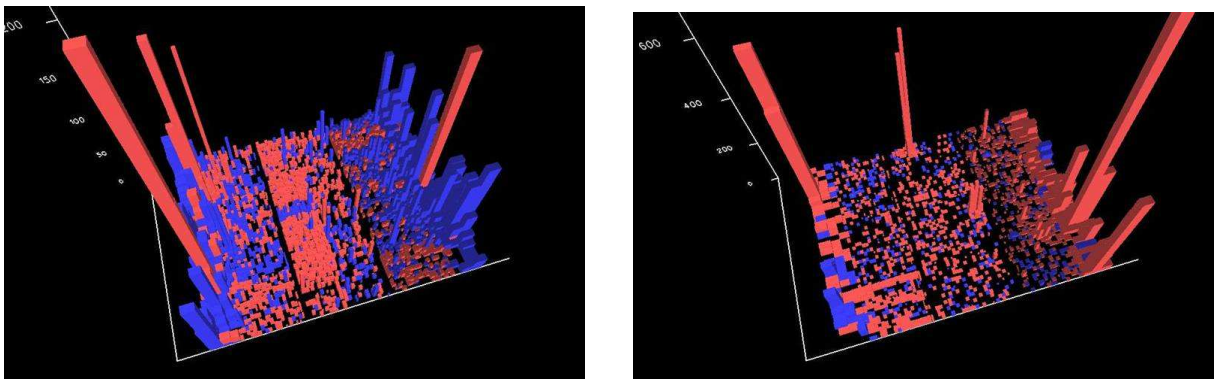

(a) (b)

Figure 1.13: The typical "coherent noise" events. The x and y axes are η and ϕ axes of the calorimeter. Z axis is a EM tower signal in the ADC counts. The red color corresponds to the positive signal in the tower, the blue one is a negative signal.

to be the parameter with the best separation power. In Fig. 1.12, the occupancy of crate five (crate with noise) and zero (crate without noise) versus the RMS of the cell signals in ADC counts in the crate are shown. In this plot the noisy events can clearly be seen at high values of the occupancy. The typical fraction of events that is removed by the "noon noise" selection in the compromised runs, is around 1%, while the inefficiency of this selection for the non-noisy events is around 0.4% (for the run with an instantaneous luminosity of $\sim 50 \cdot 10^{30}\ cm^{-2}s^{-1}$).

The "coherent noise" is a problem which was present during all Run II data taking. It manifests itself as a small and coherent signal in one or several ADCs. The term "noise" here is misleading. In fact, this problem is associated with the calorimeter readout and consists in coherent shifts in the pedestal values for "all" cells in one or several ADCs. It only happened when the level 1 trigger arrives while a previous level 2 accepted trigger is being digitized. The exact cause of this problem was never identified. Event display of two typical "coherent noise" events is shown in Fig. 1.13. Fig. 1.13(b) shows the case of "pure" noisy event which fulfill the trigger condition, the Fig. 1.13(b) shows the case when noise in 2 ADCs accompany the signal of the real particles.

To characterize the noise the following quantities were calculated per ADC after the

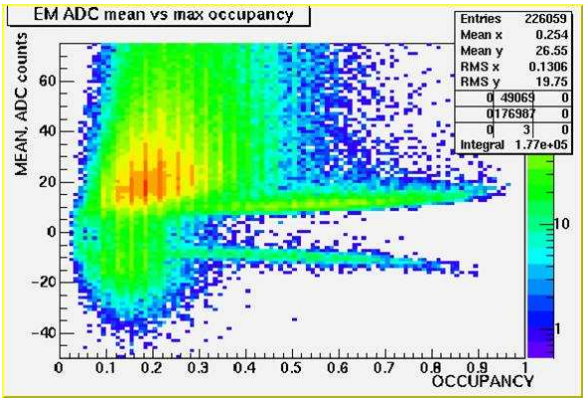

Figure 1.14: The mean signal in ADC counts (y axis) versus ADC occupancy (x axis) for the ADC with maximal occupancy in the event.

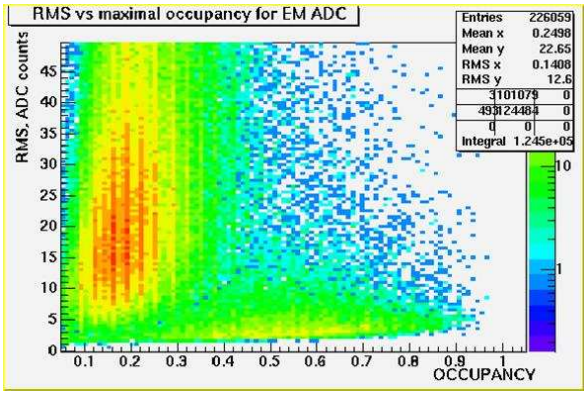

Figure 1.15: The ADC RMS in counts (y axis) versus ADC occupancy (x axis) for the ADC with maximal occupancy in the event.

2.5σ zero suppression procedure.

- The ADC occupancy $= \frac{n}{N}$
- The ADC mean value: $\langle E \rangle = \frac{\sum_{i=1}^{N} E_i}{N}$.
- The ADC RMS $= \sqrt{\frac{\sum_{i=1}^{N}(E_i - \langle E \rangle)^2}{N-1}}$

In these expressions, N is the total number of cells in the selected ADC, n is a number of cells with non zero signal after 2.5σ zero suppression, $i \leq N$ is a cell index, E_i is a signal in the cell i in ADC counts. Fig. 1.14 and 1.15 show the mean ADC value and RMS versus ADC occupancy for the ADC with the maximal occupancy in the event for a selected data taking run. We marked the events as the "coherent noise" event if at least one ADC has occupancy greater or equal to 40% and RMS less or equal to 10 ADC counts or at least 2 ADCs have occupancy greater or equal to 20% and RMS less or equal to 5 ADC counts. The ADC mean value and RMS are calculated after rejecting 10% of the cells with highest absolute signal value. Later, this selection was refined in order to improve the efficiency of the detection.

The event fraction affected by this effect depends on the luminosity and trigger. The typical fraction of such events is not negligible, typically 2-3%. This problem could affect the analysis in different ways: it may increase the number of low energy jets, biasing the missing transverse energy distribution, affect the lepton isolation criteria and degrading the energy resolution for low energy jets. We decided to remove all such events in all analysis. For this, it is important to know the inefficiency of the "coherent noise" removal criteria. At D0, in order to account for the realistic detector noise and beam conditions, the zero bias data events are overlayed to the Monte Carlo (MC) events at the generation stage. This realistically simulates the fraction of events to be removed in the analysis due to the "coherent noise" problem.

1.2.3 The Calorimeter Data Quality Strategy

To following strategy has been used in D0 to ensure the highest possible data quality.

- The on-line monitoring controls and immediately reports to a shifter any obvious hardware failure. The detected failure is repaired as soon as possible, in order to minimize the fraction of data affected by the problem.

- The on-line monitoring also provides the list of runs and luminosity blocks with a "bad" quality.
- This list is completed by the off-line cross-checks, based on the physical quantities, missing E_T, number of reconstructed jets, leptons, etc.
- Bad runs and luminosity blocks are removed from further processing. The integrated luminosity for the analysis is recalculated and accounts for the removed data.
- Two algorithms are used to remove isolated "hot" cells, and reduce the noise in the event. These algorithms improve the energy resolution for jets and missing transverse energy.
- The event quality software flags are used in physics analyses to remove the problematic events and remove the influence of the external noise or readout problems. Correction to the efficiency is accounted for due to the overlay of real events (zero bias) to the MC simulation.

An illustration of the importance of the good data quality is shown in Fig. 1.16, [8]. Without clean-up of the data set, the missing E_T distribution is completely distorted and could not be used for analysis. The application of the data quality strategy allows not only to select good data sets, but also to reduce the data with failures. Fig. 1.17 demonstrate the improvement with time in the quality of the accumulated D0 data set. For example, in the beginning, we lost about 10% of data due to calorimeter problems, but only 3% in the end of the data taking. A similar trend is seen for all D0 subsystems, i.e. in 2003–2004 the portion of data with bad quality was about 15%, but less than 5% after 2009.

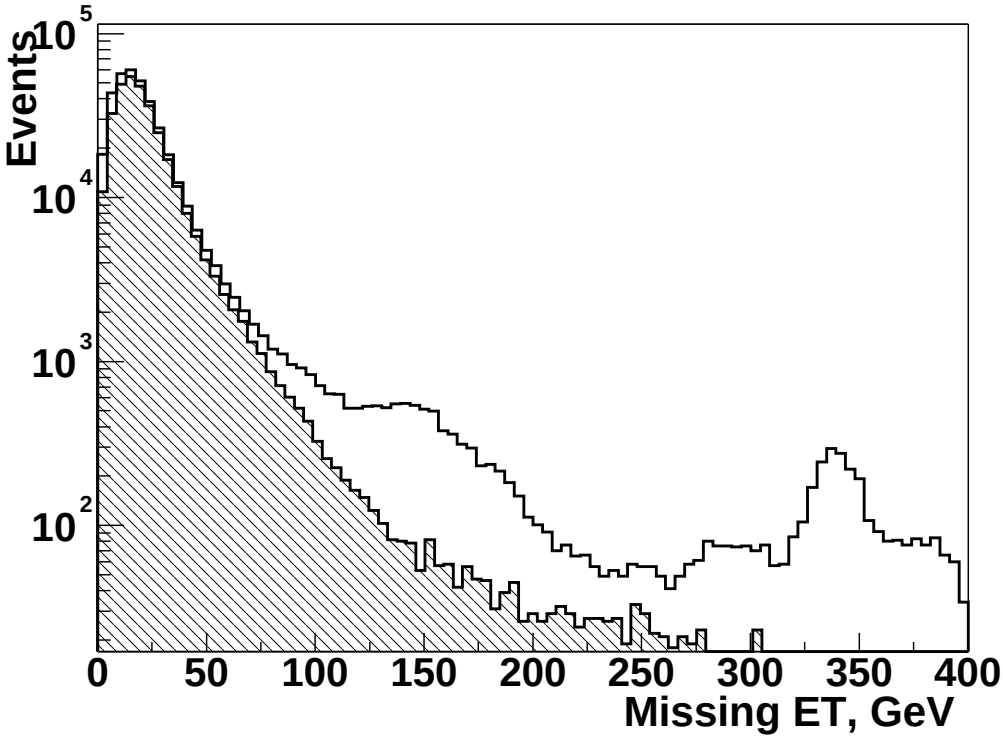

Figure 1.16: Missing E_T distributions in data selected for the new phenomena search before and after the data quality requirements are applied [8]. The white histogram represents all events, The shaded histogram represents the events after selecting "good" data quality events.

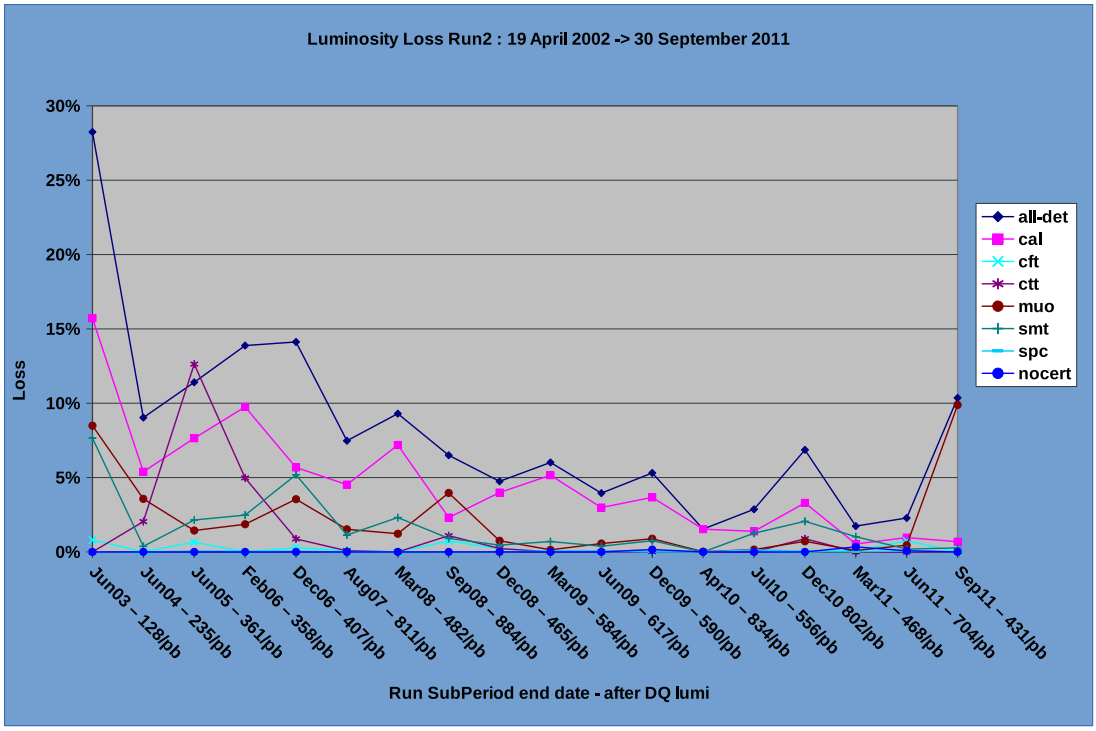

Figure 1.17: The fraction of data with identified data quality problems as a function of time.

1.3 Common Analysis Tools

From 2002 to 2011 the D0 experiment accumulated about 9.7 fb^{-1} of data, with a total size of about 12 billions events or nearly 2000 TBytes of raw data. To make these data available for physics analyses they were reconstructed and saved in the format suitable for analysis. The post-processing of raw data and Monte Carlo event generation increased the data set size in the experiment to $\sim$ 8000 TB. The computing infrastructure of the experiment consists of the following main components: high speed mass storage system (robotic tape archive); Linux disk cache server; Oracle database; reconstruction and analysis farms of Linux nodes operated under Scientific Linux OS with CPU capacities about 8 THz for D0; Linux desktops; 1 Gb internet connection to the central systems, 100Mb to the desktops. Similar, but smaller size installations provided by the collaborating institutes worldwide.

The data life-cycle is organized as follows. The detector raw data are saved on the tape archive, then read back and reconstructed on the reconstruction farm. D0 reconstructed data on a time scale of several days. To optimize the data access during physics analysis the reconstructed data are sorted to 12 output streams which group events with similar final states according to the trigger and offline event selection. Finally the reconstructed data are transformed to the form suitable for physics analysis. In D0 we chose to use ROOT trees [10]. Several times D0 reprocessed the raw data because of the improvements in the reconstruction algorithms and updates in calibrations. In addition to the post-processing data activities, physics analyses and MC events generation and reconstruction consume a significant fraction of the computing resources.

1.3.1 Data handling

The central part of the computing model is the data handling system [11]. The Tevatron collider reached its maximum instantaneous luminosity of about $4 \cdot 10^{32} cm^{-2} sec^{-1}$. The output rates to tapes was 50 – 100 Hz ($\sim$20 MB/sec) and the total amount of data is about 8000 TB. To manage such an amount of data D0 uses the "Sequential Access via Metadata" (SAM) software [12–14] developed by D0 and Fermilab Computer Division. SAM is a client-server software which provides support for the large, highly distributed data sets. This is a file based system, where each file is described by metadata: for example, file production history, list of parentage files (necessary element for the luminosity calculation), file locations (including mass storage system and SAM-managed disks), format of data in the file, parameters used to generate MC events, etc. To access data files the user defines the collection of files, the so-called "dataset", using metadata with command lines or web browser interfaces. SAM is able to manage multiple copies of files located in different places. To optimize the file delivery time the disk cache is used to keep files frequently requested on disk and the file order in the collection is optimized for tape reading. D0 has a very successful experience in using SAM. During the active phase of experience, D0 users routinely consume nearly 800 TB of data per month from SAM.

1.3.2 Physics Analysis

The organization of the physics analysis tools plays a major role in the production of reliable physics results. Obvious requirements to the analysis software are that it should run fast and the analysis format should be compact. For the optimal organization of the analysis efforts one needs to ensure a universal certified selection of physics objects (electron, jets, muons ...) and have the possibility to use a common infrastructure for different type of physics analyses, which are the opposite requirements to the fast and

Skim Name	Main Selections	N events
MUinclusive	at least 1 muon with $p_T > 10$ GeV	2.9G
EMinclusive	at least 1 electron with $p_T > 20$ GeV	1.6G
2EMhighpt	at least 2 electrons with $p_T > 12$ GeV	222M
2MUhighpt	at least 2 muons with $p_T > 8$ GeV	150M
EMMU	1 or more electron and 1 or more muon with $p_T >$ 5 GeV	351M
3JET	at least 3 reconstructed jets with p_T cuts 20, 15, 15 GeV	1.2G
QCD	a set of 1-jet and 2-jets triggers with different p_T cuts	220M
TOPJETTRIG	a set of lepton+jet triggers	291M
NP	a set of triggers based on jets and simplified missing E_T quantities	300M
TAUTRIG	a set of triggers designed for τ-lepton identification	1.0G
JPSI	a set of triggers	31M
ZBMB	events selected by the beam crossing trigger and trigger including both, beam crossing and luminosity counter signal	488M
All events		10G

Table 1.1: Data skims in the D0 experiment, selections applied to the skim and number of selected events. Only the most important selections are indicated for each skim. The skim selection are inclusive, i.e. an event could be selected in several different skims.

compact ones. The absence of a common format leads to an inefficient usage of computer resources and difficulties in software maintenance because of work duplication and limited manpower. In reality it is difficult to reach an idealistic case of one format, e.g. D0 has one ROOT tree based common analysis format (CAF) and one format for B-physics [11]. The processing time in user analysis is typically 0.1 – 0.005 sec/event, and it is limited by I/O speed and proportional to the event size, typically 35 – 60 kB in the case of D0.

D0 analysis format, CAF, is an example of successful realization of a common analysis architecture. Because this format is based on the ROOT tree, one can use C++ classes for objects descriptions and ROOT pointers for the cross-reference between objects. A C++ class is associated to each reconstructed or generated object, e.g. electron, muon, tracks, jets, trigger objects, or to a calculated quantity, e.g. missing E_T, b-tagging, luminosity. The unavoidable disadvantage of the universal format is the big events size, but it is partially compensated by the possibility to skim trees using event selection and the possibility to drop off unnecessary branches during skimming. We divided all data sets in 12 skims, presented in Table 1.1. The production of CAF root trees is coordinated centrally and provides data for physics analyses with minimal delay to the whole collaboration.

We developed the following set of standard tools to analyze events in the common analysis format.

- The certified selection of physics objects: jets, electrons, muons, τ-leptons, tracks, photons, vertex, trigger objects. The certified selection of events with good data quality.

- In order to match the parameters of the simulated objects to data, we apply the

set of MC corrections as a function of the data taking period, energy or p_T, η and ϕ of the simulated object. These corrections include: electron energy and muon p_T smearing, jet energy smearing, corrections for the leptons and jet identification efficiency, reweighting of the simulated instantaneous luminosity distribution, reweighting of the simulated Z-boson p_T distribution, reweighting of the interaction vertex distribution in Z-coordinate.

- Recalculation of parameters: jet energy scale, missing E_T, b-tagging.
- MC tools: identification of the generated objects, matching between generated and reconstructed objects, reweighting of the heavy flavor K-factors in the W+jets and Z+jets simulations, tools for the automatic MC sample normalization as a function of the integrated luminosity and theoretical cross section.
- Tools for the systematic uncertainty studies: reweighting of the proton and antiproton parton density function between different sets, b-quark fragmentation reweighting.
- Utilities: statistical tool to measure the selection efficiency taking into account the MC correction weights, tools to store in ASCII format the sets of the measured efficiencies for the object ID in data and MC and associated meta-data.

The event-by-event processing scheme is realized in the CAFe framework and constructed from standard pieces of code, managed by the ASCII configuration files, see Fig 1.18. The typical processing scheme of one file includes the following steps.

1. Open a CAF file. Open an output file for histograms and skimmed events.
2. Read first event from the CAF file and fill the transient event object.
3. Process the event with the standard piece of code, called processor. The typical processor is a selector, which apply one selection to the events. If an event doesn't fulfill the selection criteria, it is dropped and processing return to the step 2. Any number of processors is allowed. Physicists could write theirs own processors and implement any non-standard selection or correction.
4. Selected events are used to fill ROOT histograms (analysis mode).
5. Selected events could be saved in a new ROOT-tree (skimming mode).
6. Return back to the step 2 and start processing of a new event.
7. The file with histograms and/or skimmed events is closed before closing the input CAF file.

This framework doesn't require any deep knowledge of programming and allows any user to assemble analysis selection and be sure to apply all necessary corrections and standard object identifications with known uncertainties. This framework allows also to save a lot of time in developing analysis code and, even, after the end of the Tevatron era, efficiently continue to analyze data with a limited manpower.

```
############# THIS INSTRUCTION RUNS PROCESSORS IN THE GIVEN ORDER ############

cafe.Run: Stat(eff) BadLBNs(lbns) EventQuality(eventQuality) ElectronSelector(electron)
 MuonSelector(muon)   VertexSelector(vertex) JetSelector(jet)  METSelector(met) Topolog
icalSelector(topo) Hist1D(muonpT)


############# GENERAL CAFE CONFIGURATION #####################################

# attach specified packages (emid_cuts packages is used by ElectronSelector)
cafe.Packages: emid_cuts caf_util

# print debug messages
cafe.Debug: 0

# input root file or list of files
#cafe.Input:  /prj_root/1402/caf_write/CAF-EMMU-p18.01.00/CAF-V1-CSskim-EMMU-20050507-1
92359-825502.raw_p17.03.03.root
cafe.Input: listfile:filelist.dat

# number of events to proceed
cafe.Events: 5000

#output file with histograms
cafe.Output: test.root
```

Figure 1.18: Example of a simple configuration file for the analysis run in the CAFe framework. The first line "cafe.Run: ..." specifies the order of the event processors. Other lines are the processor configurations.

Bibliography

[1] S. Abachi et al., "The D0 Detector", Nucl.Instrum.Meth. **A338**, 185–253 (1994).

[2] S. Abachi et al., "Observation of the top quark", Phys. Rev. Lett. **74**, 2632–2637 (1995), arXiv:`hep-ex/9503003 [hep-ex]`.

[3] V. Abazov et al., "A precision measurement of the mass of the top quark", Nature **429**, 638–642 (2004), arXiv:`hep-ex/0406031 [hep-ex]`.

[4] V. Abazov et al., "The Upgraded D0 detector", Nucl. Instrum. Meth. **A565**, 463–537 (2006), arXiv:`physics/0507191 [physics.ins-det]`.

[5] D. Schamberger, "Design, construction, commissioning and long term operational experience with the D0 Uranium/Liquid Argon calorimeter", 59–68 (2014), arXiv:`1403.4391 [physics.ins-det]`.

[6] V. M. Abazov et al., "Measurement of the inclusive jet cross section in $p\bar{p}$ collisions at $\sqrt{s} = 1.96$ TeV", Phys. Rev. **D85**, 052006 (2012), arXiv:`1110.3771 [hep-ex]`.

[7] V. M. Abazov et al., "Measurement of the W boson mass with the D0 detector", Phys.Rev. **D89**, 012005 (2014), arXiv:`1310.8628 [hep-ex]`.

[8] V. Shary, "Data quality monitoring for the D0 calorimeter", Proceedings of 11th International Conference on Calorimetry in High-Energy Physics, Perugia, Italy, 205–209 (2004).

[9] S. Trincaz-Duvoid, "Calorimeter algorithms for D0", Proceedings of 11th International Conference on Calorimetry in High-Energy Physics, Perugia, Italy, 343–348 (2004).

[10] *The ROOT project web page: http://root.cern.ch*, `http://root.cern.ch`.

[11] V. Shary, "Computing tools and analysis architecture: The Tevatron experience", Nucl. Phys. Proc. Suppl. **177-178**, 18th Hadron Collider Physics Symposium 2007 (HCP 2007), 121–125 (2008).

[12] L. Lueking, L. Loebel-Carpenter, W. Merritt, C. Moore, R. Pordes, et al., "The D0 experiment data grid: SAM", Lect.Notes Comput.Sci. **2242**, 177–184 (2001).

[13] I. Terekhov, "Distributed processing and analysis of physics data in the D0 SAM system at Fermilab", (2001).

[14] I. Terekhov, "Meta-computing at D0", Nucl.Instrum.Meth. **A502**, 402–406 (2003).

Chapter 2

Top Quark Studies

2.1 Introduction

The Standard Model (SM) of particle physics postulates the existence of three particle generations. Each generation contains two quarks, a charge lepton and its corresponding neutrino, as well as their antiparticles. The third generation contains the heaviest particles: top and bottom quarks, tau lepton and tau neutrino. The top quark is a fermion with spin $\frac{1}{2}$ and electric charge of $+\frac{2}{3}$. Together with the bottom quark they form weak isospin doublet, in which the positive projection value $T_3 = +\frac{1}{2}$ is assigned to the top quark. Under the SU(3) gauge group of the strong interactions the top quark transforms as a color triplet [1].

The top quark is the heaviest known elementary particle, with a mass of 174.34 ± 0.64 GeV/c^2 [2]. Because of its large mass, the top quark has been discovered only in 1995 by the D0 and CDF experiments at the Tevatron $p\bar{p}$ collider at Fermilab [3, 4]. The history of the top quark could be started with the prediction of the third generation by M. Kobayashi and T. Maskawa, intended to explain the CP violation in K-meson decays [5]. The existence of the third generation has been confirmed with the discoveries of the τ lepton in 1975 at SLAC [6] and the Υ meson formed with a bottom quark and antiquark in 1977 at Fermilab [7]. After these discoveries, the existence of the weak isospin partner of the bottom quark was the natural hypothesis.

Several experiments were searching for the top quark in e^+e^- collisions. PETRA at DESY in the 1984 – 1985 established a limit on the bound $t\bar{t}$ state production of about 47 GeV [8, 9], so the top quark with a mass up to 23.5 GeV/c^2 has been excluded. TRISTAN at KEK in the 1990 has excluded the top quark with a mass up to 30 GeV/c^2 [10]. At the same time SLC at SLAC [11] and LEP experiments [12–14] pushed the limit on the top quark mass up to 46 GeV/c^2 by searching for the top quark production in the Z-boson decays. In the 1980s, the construction of hadron colliders, ISR and $Sp\bar{p}S$, at CERN allowed to search for the top quark in the W boson decay $W \to tb$ and demonstrated the absence of the top quark production for a mass up to 69 GeV/c^2 in 1990 [15, 16]. Finally the construction of the Tevatron $p\bar{p}$ collider in the late 80s with a center-of-mass energy of 1.8 TeV led to the top quark discovery in 1995 [3, 4] by both CDF and D0.

The top quark is a very special quark with several unique features. One of them is the value of the Yukawa coupling of the top quark. The Yukawa term of the SM Lagrangian describes the interaction of the fermions with the Higgs field and it is the origin of the fermion masses [17, 18]:

$$\mathscr{L}_M = -\frac{1}{\sqrt{2}}\lambda_t v \bar{t}_L t_R - \frac{1}{\sqrt{2}}\lambda_b v \bar{b}_L b_R + h.c. \ , \tag{2.1}$$

where λ_t is a Yukawa coupling of the top quark and v is a vacuum expectation value of the Higgs field, $v = 1/\sqrt{G_F\sqrt{2}} \simeq 246.2\ GeV$. In the SM mass of the top quark is given by $M_t = \frac{1}{\sqrt{2}}\lambda_t(M_t)v$. With the measured value of the top mass 174.3 GeV [2][1] the Yukawa coupling of the top quark is found to be extremely close to 1.0: $\lambda_t(M_t) \simeq 1.001$. This fact is the origin of different speculations about the special role of the top quark in the theory and about the possibility that the Higgs boson could be a bound state of the top quark (top quark condensate models) [19–22].

An important property of the top quark is its fast decay. In the SM the top quark decays predominantly to a W boson and a b quark. The width of the top quark is given by the following expression (the higher order electroweak correction of order m_b^2/m_t^2, α_s^2, $(\alpha_s/\pi)m_W^2/m_t^2$ are ignored) [23, 24]:

$$\Gamma_t = \frac{G_F m_t^3}{8\pi\sqrt{2}}\,|V_{tb}|^2\left(1-\frac{M_W^2}{m_t^2}\right)^2\left(1+2\frac{M_W^2}{m_t^2}\right)\left[1-\frac{2\alpha_s}{3\pi}\left(\frac{2\pi^2}{3}-\frac{5}{2}\right)\right] \tag{2.2}$$

Other $t \to Wq$ decays are also allowed in the SM, but the probability of such decays is proportional to the square of the Cabibbo-Kobayashi-Maskawa (CKM) matrix element V_{tq}. Assuming unitarity of the CKM matrix, the matrix element values V_{ts} and V_{td} are estimated to be 0.043 and 0.008, respectively [1]. Such small values imply that top quark decays other than Wb should have a rate of the order of $2 \cdot 10^{-3}$. For a top quark mass of 173.2 GeV and $\alpha_s(M_Z) = 0.118$ formula (2.2) gives a width of the top quark of 1.35 GeV and a corresponding life time of $\tau \approx 4.9 \cdot 10^{-25}$ sec. The fact that the top quark life time has such a small value is extremely important for the measurement of the top quark properties. In particular, this life time is smaller than the top quark hadronization time, estimated as, $\tau_{had} \sim (\Lambda_{QCD})^{-1} \approx (200\ MeV)^{-1} = 3.3 \cdot 10^{-24}$ sec, where Λ_{QCD} is a fundamental quantum chromodynamics (QCD) scale. It is also smaller than the spin decorrelation time, due to the spin-spin interaction with the light quark, $\tau_{spin} \sim (\Lambda_{QCD}^2/m_t)^{-1} \approx (0.2\ MeV)^{-1} = 3 \cdot 10^{-21}$ sec, see, for example, [17]. This means that the top quark decays before it has a chance to hadronize and its decay products, W boson and b quark, "remember" the spin of the initial quark. Such a situation gives a unique possibility to measure the properties of the top quark with high precision, including spin related properties.

In $p\bar{p}$ collisions the top quark can be produced in pairs by strong interactions and the single top quark can be produced by electroweak interactions. The leading Feynman diagrams for the top quark production in pairs are shown in Fig. 2.1, 2.2 and for the single top production in Fig. 2.3. In this manuscript we describe only the measurements of the top quarks produced in pairs. It should be noticed that to *leading order* (LO) of the QCD calculation, the pair of top quarks can be produced via the quark-antiquark annihilation, Fig. 2.1 or via gluon fusion, Fig. 2.2. At the Tevatron, in $p\bar{p}$ collisions with a center-of-mass energy of 1.96 TeV, the dominant production mechanism is the quark-antiquark annihilation, with a probability of about 85%, see, for example, [25, 26]. This is an important difference to top pair production in pp collisions at the LHC with the center-of-mass energy of 7–14 TeV, where the dominant production mechanism is gluon fusion. This difference in production is a main reason why many of the measurements for the top quark are complementary between the two colliders.

The finals states in the top quark pair production used for the measurements are

[1] In fact, the Lagrangian mass parameter doesn't correspond exactly to the mass measured experimentally. See the corresponding discussion in the section 2.5

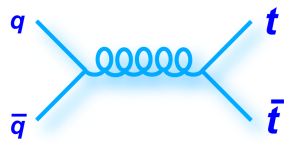

Figure 2.1: Feynman diagram for the top quark production via quark-antiquark annihilation.

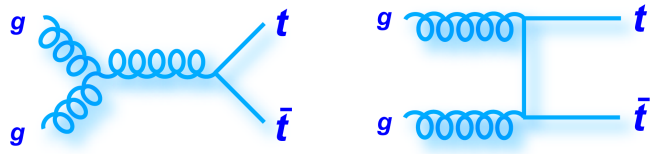

Figure 2.2: Feynman diagrams for the top quark production via gluon fusion.

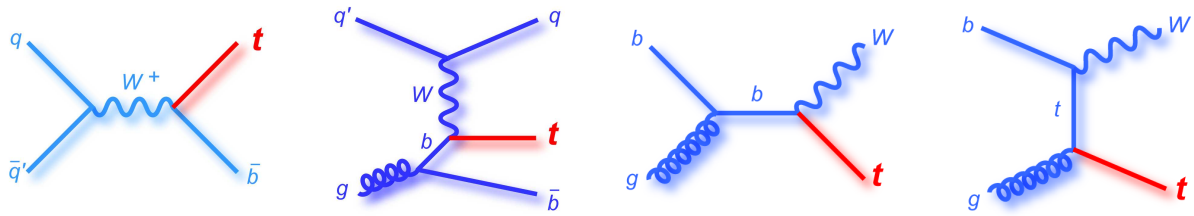

Figure 2.3: Feynman diagrams for the single top quark production.

classified according to the decay of the W boson.

$$
\begin{aligned}
\text{all jets}: &\quad t\bar{t} \to W^+b\, W^-\bar{b} \to \; b\bar{b}qq'q''q''',\\
\text{lepton} + \text{jets}\ (\ell + \text{jets}): &\quad t\bar{t} \to W^+b\, W^-\bar{b} \to \; \ell\nu_\ell b\bar{b}qq',\\
\text{dilepton}\ (\ell\ell): &\quad t\bar{t} \to W^+b\, W^-\bar{b} \to \; \ell\ell'\nu_\ell\nu_{\ell'}b\bar{b}.
\end{aligned}
$$

Assuming lepton universality in W decays, the decay probability for these three final states are the following: 45.5% for the all jets, 43.8% for the ℓ+jets and 10.5% for the $\ell\ell$ [1], where ℓ denotes electron (e), muon (μ), or tau lepton (τ). In this manuscript we consider mainly measurements in the $\ell\ell$ final state and the combination of $\ell\ell$ and ℓ+jets results, which leads to the improved precision of the measurements.

2.2 Selection of $t\bar{t}$ Events in the Dilepton Final State

This section describes a selection of $t\bar{t}$ events in the dilepton final state. This selection has evolved in time, starting from the cross section measurement with an integrated luminosity of 0.4 fb^{-1} and up to the measurement with the full D0 luminosity of 9.7 fb^{-1}. We keep the selection as similar as possible in the different dilepton measurements, but optimization of the final cuts are usually performed in each analysis. In this section, we describe the basics of the selection, efficiency estimation for the $t\bar{t}$ signal and estimation of the background contributions. The details for each measurement can be found in the referenced publications.

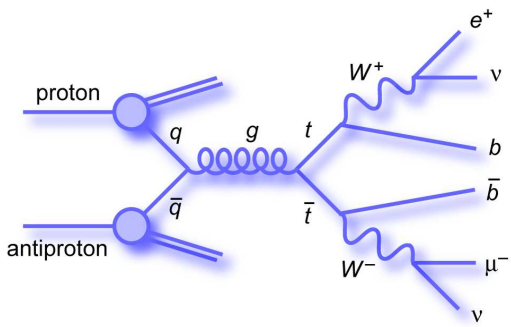

Figure 2.4: Feynman diagram for the $t\bar{t}$ event decay in the dilepton ($e\mu$) final state .

The $t\bar{t}$ decay to dilepton final states are characterized by the presence of two high p_T charged leptons, significant *missing transverse momentum* ($\not{p}_T$) from two escaping neutrinos, and two or more jets (from b quark fragmentation and initial and final state radiation). The corresponding Feynman diagram is shown in Fig. 2.4. We consider the leptonic decays of both W bosons from top quark decay into $e\nu_e$, $\mu\nu_\mu$, or $\tau\nu_\tau$ (throughout this manuscript, e, μ, τ refer to both charge conjugate states: $e^\pm$, $\mu^\pm$ or $\tau^\pm$), where only leptonic decays of the τ are considered.

2.2.1 Object Identification

Electrons are identified as energy clusters with radius $\mathcal{R} = \sqrt{(\Delta\eta)^2 + (\Delta\phi)^2} < 0.2$ in the calorimeter (ϕ is the azimuthal angle) which are consistent in their longitudinal and transverse profiles with those of an electromagnetic shower [27]. More than 90% of the energy of the electron candidate must be deposited in the electromagnetic part of the calorimeter, and less than 20% of its energy may be deposited in an annulus of $0.2 < \mathcal{R} < 0.4$ around its direction. This cluster has to be matched to an inner detector track. We consider electrons in the central calorimeter (CC) with $|\eta_{\rm det}| < 1.1$ and in the end-cap calorimeter (EC) with $1.5 < |\eta_{\rm det}| < 2.5$. Several versions of the electron discriminant to improve electron identification were developed at D0. In the earlier version, the likelihood discriminant, based on tracking and calorimeter information has been used. In the latest version, the boosted decision tree multivariate discriminant has replaced the likelihood [27].

A *muon* is identified as a segment in at least one layer of the muon system that is matched to a track in the central tracking system [28]. Reconstructed muons must satisfy two isolation criteria. First, the transverse energy deposited in an annulus around the muon $0.1 < \mathcal{R} < 0.4$ ($E_T^{\mu,\rm iso}$) has to be less than 15% of the *transverse momentum of the muon* (p_T^μ). Second, the sum of the transverse momenta of the tracks in a cone of radius $\mathcal{R} < 0.5$ around the muon track in the central tracking system ($p_T^{\mu,\rm iso}$) has to be less than 15% of p_T^μ.

Jets are identified with a cone algorithm with radius $\mathcal{R} < 0.5$ [29] in the range $|\eta_{\rm det}| < 2.5$. A *jet energy scale* correction (JES) is determined by calibrating the energy deposited in the jet cone using transverse momentum balance in γ+jet and dijet events. If a muon overlaps with the jet cone, the momentum of that muon is added to the jet p_T, assuming that the muon originates from a semileptonic decay of a hadron belonging to the jet [30].

Several versions of the *b-tagging* algorithm to identify jets which originate from b

quarks have been used in the D0 experiment [31, 32]. First versions of the selection uses the secondary vertex tagging algorithm or impact parameter algorithm that exploits the long life-time of b hadrons. Later, the b-quark identification has been improved by using the neural-network tagging algorithm [31]. This algorithm combines information from the impact parameters of the tracks and variables that characterize the presence and properties of secondary vertices within the jet in a single discriminant. The most recent version uses a boosted decision tree version of the discriminant [32], which improve the tagging efficiency by about 10% with the same rate of the mis-identification of the light jets, see Fig. 2.5.

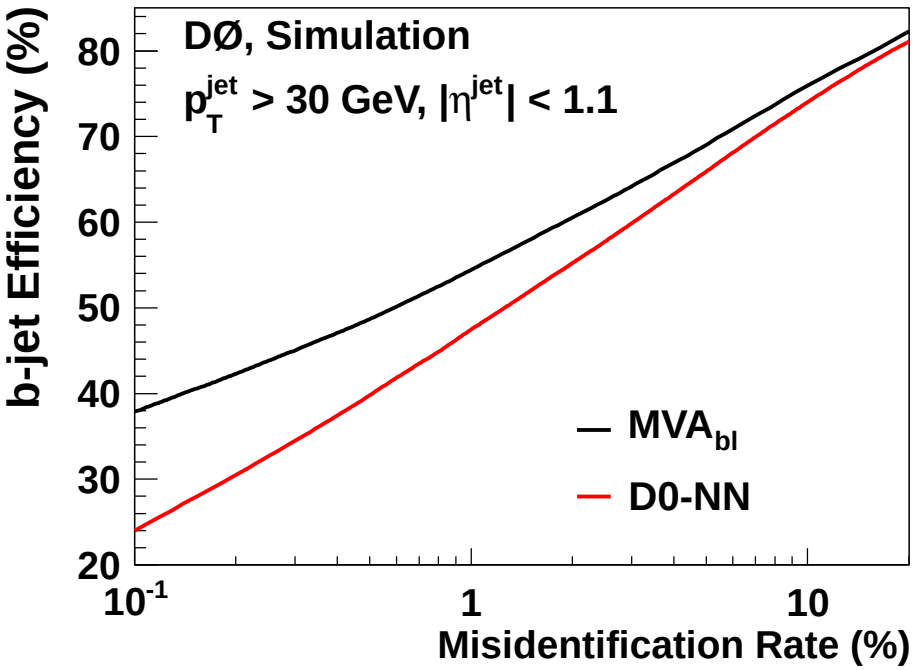

Figure 2.5: The performance of the most recent b-tagging algorithm, boosted decision tree ($\mathrm{MVA_{bl}}$) in comparison with former, neural networking algorithm (NN) for jets with $|\eta^{\mathrm{jet}}| < 1.1$ and $p_T^{\mathrm{jet}} > 30$ GeV, [32].

The $\not{p}_T$ is reconstructed from the energy deposited in the calorimeter cells (unclustered energy). Corrections for lepton and jet p_T are propagated into the $\not{p}_T$ [30]. The *missing transverse momentum significance* ($\sigma_{\not{p}_T}$) is defined in each event as a likelihood discriminant constructed using the ratio of $\not{p}_T$ to its uncertainty: $\sigma_{\not{p}_T} = \not{p}_T/\sigma$, where σ is the quadratic sum of the $\not{p}_T$ resolutions for the unclustered energy, jets, muons and electrons detected in the event.

2.2.2 Events Selection

Events selection is done separately for the three channels ee, $\mu\mu$ and $e\mu$. It is optimized in each channel and the results of the measurements are combined together. The main selections applied to events are the following.

1. For the ee and $\mu\mu$ channels, we select events that pass at least one single-lepton trigger, while for the $e\mu$ channel, we consider events selected through a mixture of single and multilepton triggers and lepton+jet triggers. Efficiencies for single electron and muon triggers are measured using $Z/\gamma^\star \to ee$ or $Z/\gamma^\star \to \mu\mu$ data, and found to be $\approx 99\%$ and $\approx 80\%$, respectively, for dilepton signal events. For the $e\mu$ channel, the trigger efficiency is almost 100%.

2. We require at least one $p\bar{p}$ interaction vertex in the interaction region with $|z| <$ 60 cm, where z is the coordinate along the beam axis, and $z = 0$ is the center of the detector. At least three tracks with $p_T > 0.5$ GeV must be associated with this vertex.

3. We require at least two isolated leptons with $p_t > 15$ GeV, both originating from the same interaction vertex. We consider only muons within $|\eta_{\rm det}| < 2.0$ and electrons within $|\eta_{\rm det}| < 1.1$ or $1.5 < |\eta_{\rm det}| < 2.5$. The two highest-$p_T$ leptons in an event must have opposite electric charges.

4. To reduce the background from bremsstrahlung in the $e\mu$ final state, we require the distance in (η, ϕ) space between the electron and the muon trajectories to be $\mathcal{R}(e, \mu) > 0.3$.

5. In the ee and $\mu\mu$ channels, we require at least two jets with $p_T > 20$ GeV. For the $e\mu$ channel, we consider two types of events: (i) events with at least two jets ($e\mu$ 2-jets) and (ii) events that contain just one detected jet ($e\mu$ 1-jet).

6. To improve the signal purity, additional selection criteria are implemented based on global event properties of the final state. In the $e\mu$ events we apply a selection on the H_T variable, where H_T is the scalar sum of the transverse momenta of the leading lepton and the two leading jet, with a typical cutoff value around 110 GeV. In the ee final state, we apply a selection on the $\sigma_{\not{p}_T}$variable, typically $\sigma_{\not{p}_T} > 5$. In the $\mu\mu$ channel, we typically require $\not{p}_T > 40$ GeV and $\sigma_{\not{p}_T} > 2.5$ or $\sigma_{\not{p}_T} > 5$.

7. The $t\bar{t}$ final state contains two b-quark jets, while most of the backgrounds contain light quark jets. In the first versions of selection only the topological cuts (6) have been used to improve separation between signal and background. In the more recent measurements we use the b-quark identification discriminant of the two jets of largest p_T. It is used in two different manners. For the cross section measurement we fit the discriminant distribution and determine the relative contributions of the $t\bar{t}$ signal and backgrounds. For other measurements, we apply a cut on the b-tagging discriminant and consider only events with a discriminant value higher than a selected cut.

2.2.3 Estimation of the $t\bar{t}$ Efficiency and Background Contribution

The main sources of background in the $\ell\ell$ channel are the Drell-Yan and Z boson production ($Z/\gamma^\star \to \ell\ell + jets$), diboson production ($WW$, WZ, $ZZ \to \ell\ell(\ell) + jets$), and instrumental background. The instrumental background mainly arises from multijet and $W \to \ell\nu + jets$ events in which one or two jets are misidentified as electrons and/or muons originating from the semileptonic decay of a heavy flavor hadron.

To estimate the signal efficiency and background contamination, we use a Monte Carlo (MC) simulation of $t\bar{t}$ signal and all background processes but for the instrumental background, the latter being derived from data. The $t\bar{t}$ and $Z/\gamma^\star$ events are generated with the tree level LO matrix element generator ALPGEN [33] interfaced with PYTHIA [34] generator for parton showering and hadronization (D0 modified tune A [35]). Diboson events are generated with PYTHIA. All simulated samples are generated using the CTEQ6L1 parton distribution functions (PDF) [36]. Generated events are processed through a GEANT3 [37] based simulation of the D0 detector and the reconstruction programs, identical to one used

for the data processing. To simulate the effects from additional $p\bar{p}$ interactions, zero bias events with no trigger requirements are selected randomly in collider data and overlayed on the fully simulated MC events. Residual differences between data and MC simulation in the identification efficiencies, electron and muon p_T resolutions are corrected by an additional scale factors and reweighting functions. These corrections are derived from a sample of $Z/\gamma^\star \to \ell\ell$ events in data and MC, applying tight requirements on one of the two leptons for selecting the events and using the other one to measure the efficiencies and resolutions[2].

The $Z/\gamma^\star$ samples are normalized to the NNLO cross section computed with the FEWZ program [38]. We simulate $Z/\gamma^\star$ with heavy flavor (HF) quarks, $Z/\gamma^\star + b\bar{b}$ (or $Z/\gamma^\star + c\bar{c}$), separately from the $Z/\gamma^\star +$ light quarks, using the ALPGEN generator. We enhance the $Z/\gamma^\star + b\bar{b}$ LO cross section by a factor of 1.5 (1.7 for $Z/\gamma^\star + c\bar{c}$), estimated with the MCFM program [39]. The diboson samples are normalized to the NLO cross section calculated with MCFM. In addition, we apply a correction to the $Z/\gamma^\star + jets$ simulation based on data to address the imperfect modeling of the Z boson p_T in the MC [40].

The instrumental background is estimated directly from data. Two versions of this estimation has been developed. At the earlier stage, the electron identification uses the likelihood discriminant. We make the estimation based on the sample without the electron likelihood discriminant requirement. We extract the number of events with jets misidentified as electrons, n_f, and the number of events with real electrons, n_e, by maximizing the following function

$$\mathcal{L} = \prod_{i=1}^{N} [n_e S(x_i) + n_f B(x_i)] \frac{e^{-(n_e+n_f)}}{N!} \ , \tag{2.3}$$

where N is the number of selected events, x_i is the electron likelihood discriminant value in the event i, and $S(x_i)$ and $B(x_i)$ are the signal and background probability density functions (pdf), see Fig. 2.6. The signal pdf is measured in $Z/\gamma^\star \to ee$ data events. The background pdf is measured in $e\mu$ events with the same selection as the analysis sample but inverting the opposite sign lepton requirement (i.e., requiring leptons of the same sign). The topological requirement is also not applied in this selection and muons are required to have the reversed isolation requirements (i.e. to be non-isolated). The total number of events with a jet misidentified as an electron is given by n_f scaled for the integral of $B(x)$ over the region satisfying the likelihood requirement.

We also determine the number of events with an isolated muon arising from jets in the $e\mu$ and $\mu\mu$ channels. This number is estimated as $n_f^\mu = N_{\text{loose}} f_\mu$, where N_{loose} is the number of events in the same sign sample with loose isolation criteria on the muon and f_μ is the misidentification rate for isolated muons. In the $\mu\mu$ final state, we apply these loose isolation criteria only to one randomly chosen muon. In the $e\mu$ channel, the number of events with jets misidentified as electrons in the same sign sample is subtracted from N_{loose}. The misidentification rate, f_μ, is determined in a dimuon sample with at least one jet. In this sample we require one muon to be close to the jet ($R(\mu, \text{jet}) < 0.5$) with reversed isolation criteria. The other muon, defined as the probe, should pass the loose isolation criteria. We compute f_μ as the ratio of the number of events in which the probe muon passes the tight isolation criteria to the total number of events in this same sign sample.

In the more recent analysis, the electron identification was improved and uses the boosted decision tree discriminant (MVA). This discriminant has a very different output distribution, so the fit procedure described above is not optimal. The modified version of estimation uses the "matrix method". The loose sample of events (n_{loose}) is defined

[2]This is the so-called "tag-and-probe" method.

following the same selection as used for the $t\bar{t}$ signal but ignoring the requirement on the electron MVA discriminant. We measure the efficiency ε_e that events with a true electron pass the requirement on the electron MVA discriminant using $Z/\gamma^\star \to ee$ data. We measure the efficiency f_e that events with a misidentified jet pass the electron MVA requirement using $e\mu$ events similarly to the $B(x)$ determination, described above. We extract the number of events with jets misidentified as electrons, n_f, and the number of events with true electrons, n_e, by solving the equations:

$$n_{\text{loose}} = n_e/\varepsilon_e + n_f/f_e, \tag{2.4}$$

$$n_{\text{tight}} = n_e + n_f, \tag{2.5}$$

where n_{tight} is the number of events remaining after applying the default selections. The factors f_e and ε_e are measured separately for each jet multiplicity (0, 1, and 2 jets), and separately for electron candidates in the CC and EC parts of the calorimeter. Typical values of ε_e are 0.7 – 0.8 in the CC and 0.65 – 0.75 in the EC. Values of f_e are 0.005 – 0.010 in the CC, and 0.005 – 0.020 in the EC.

The estimation of the instrumental background due to the isolated muon was also optimized in order to match the updated muon ID definitions in the recent analyses. In the $e\mu$ and $\mu\mu$ channels, we determine the number of muon background events relying on the main analysis selection, but requiring that both leptons have the same charge. In the $\mu\mu$ channel, this number of events is taken to be the number of same-sign events. In the $e\mu$ channel, it is the number of events in the same-sign sample after subtracting the contribution from events with jets misidentified as electrons.

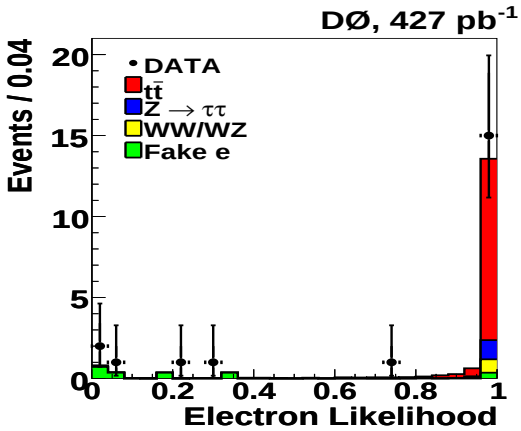

Figure 2.6: The electron likelihood distribution in $e\mu$ channel, used to determine contribution of events with a jet misidentified as electron ("fake" e) [41].

The selected number of events in the dileptons measurement for the 1 fb^{-1} analysis [42] and for the 9.7 fb^{-1} [43] are shown in tables 2.1, 2.2. The expected number of signal events has increased by a factor of ∼10 due to the 10 times larger integrated luminosity, and, in addition, the signal to background ratio has increased from ∼ 2.3 to ∼ 6.5 due to the improvements in the selection and object identifications.

Table 2.1: Numbers of expected and observed events, for the 1 fb^{-1} cross section analysis [42]. Uncertainties include both statistical and systematic contributions (excluding the luminosity uncertainty of 6.1%). Expected numbers of signal events are given for a cross section of 7.9 pb ($m_t = 170$ GeV).

	$Z \to \ell\ell$	Dibosons	Multijet W+jets	$t\bar{t} \to \ell\ell jj$	N_{expected}	N_{observed}	$\frac{N_{\text{observed}}}{N_{\text{expected}}}$
ee	$2.4^{+0.6}_{-0.5}$	$0.5^{+0.1}_{-0.1}$	$0.6^{+0.4}_{-0.4}$	$11.2^{+0.8}_{-0.8}$	$14.6^{+1.0}_{-1.0}$	17	1.16 ± 0.08
$e\mu$ 2 jets	$5.4^{+0.9}_{-1.0}$	$1.4^{+0.4}_{-0.4}$	$2.6^{+0.6}_{-0.5}$	$35.2^{+2.6}_{-2.7}$	$44.6^{+3.4}_{-3.6}$	39	0.87 ± 0.07
$e\mu$ 1 jet	$5.5^{+0.7}_{-0.8}$	$3.1^{+0.7}_{-0.7}$	$0.9^{+0.3}_{-0.2}$	$8.6^{+1.1}_{-1.1}$	$18.0^{+1.4}_{-1.6}$	21	1.17 ± 0.10
$\mu\mu$	$5.6^{+1.0}_{-1.2}$	$0.6^{+0.1}_{-0.1}$	$0.2^{+0.2}_{-0.2}$	$8.8^{+0.8}_{-0.8}$	$15.1^{+1.5}_{-1.6}$	12	0.79 ± 0.08

Table 2.2: Numbers of expected and observed events for the 9.7 fb^{-1} analysis [43]. Expected numbers of events are shown with their statistical uncertainties only. Expected numbers of signal events are given for a cross section of 7.45 pb ($m_t = 172.5$ GeV).

	$Z \to \ell\ell$	Dibosons	Multijet W+jets	$t\bar{t} \to \ell\ell jj$	N_{expected}	N_{observed}	$\frac{N_{\text{observed}}}{N_{\text{expected}}}$
ee	$17.2^{+0.6}_{-0.6}$	$2.4^{+0.1}_{-0.1}$	$4.7^{+0.4}_{-0.4}$	$127.8^{-1.4}_{-1.4}$	$152.1^{+1.6}_{-1.6}$	147	0.97 ± 0.08
$e\mu$ 2 jets	$13.7^{+0.5}_{-0.5}$	$3.9^{+0.2}_{-0.2}$	$16.3^{+4.0}_{-4.0}$	$314.7^{+1.1}_{-1.1}$	$348.6^{+4.2}_{-4.2}$	343	0.98 ± 0.05
$e\mu$ 1 jet	$8.7^{+0.6}_{-0.6}$	$3.4^{+0.2}_{-0.2}$	$2.9^{+1.7}_{-1.7}$	$61.7^{+0.5}_{-0.5}$	$76.7^{-1.9}_{-1.9}$	78	1.02 ± 0.12
$\mu\mu$	$17.5^{+0.6}_{-0.6}$	$1.9^{+0.1}_{-0.1}$	$0.0^{+0.0}_{-0.0}$	$97.7^{+0.6}_{-0.6}$	$117.1^{+0.8}_{-0.8}$	114	0.97 ± 0.09

Authors	Year	Calc. Order	Result	PDF
Czakon et al. [26, 45] ($m_t = 173.3$ GeV)	2013	NNLO+NNLL	7.16 pb $^{+2.8\%}_{-3.2\%}$	MSTW08
Ahrens et al. [46, 47]	2010	NLO+NNLL	5.93 pb $^{+5.9\%}_{-4.7\%}$	MSTW08
Moch and Uwer [48, 49]	2009	appr. NNLO	6.71 pb $^{+4.8\%}_{-5.8\%}$	MSTW08
Kidonakis [50]	2008	appr. NNLO	6.66 pb $^{+6.5\%}_{-5.3\%}$	MSTW08
Cacciari et al. [51]	2008	NLO+NLL	6.61 pb $^{+7.7\%}_{-8.6\%}$	CTEQ6.6
Nadolsky et al. [36]	2008	NLO	6.39 pb $^{+7.5\%}_{-12.0\%}$	CTEQ6.6
Cacciari et al. [52]	2004	NLO	6.47 pb $^{+10.6\%}_{-13.1\%}$	CTEQ6M
Kidonakis and Vogt [53]	2003	NLO+corr.	6.77 pb $\pm 6.2\%$	MRST2002

Table 2.3: Selected theoretical predictions for the $t\bar{t}$ production cross section in $p\bar{p}$ collision at 1.98 TeV. If top quark mass is not indicated, predictions are given for $m_t = 175$ GeV.

2.3 $t\bar{t}$ Production Cross Section and Related Measurements

The cross section measurement of $t\bar{t}$ production is one of the fundamental measurements of top quark physics. First of all, the measured cross section is compared with SM QCD calculation. Any deviation from the prediction may indicate the presence of a contribution beyond the standard model. Another important reason for this measurement is that it allows to validate the $t\bar{t}$ events selection and to use the same or similar selection in the top quark properties measurements. Additionally, the cross section measurement at D0 is used to measure the top quark mass with a non conventional method, and importance of such approach will be explained later in the section 2.5.

During the recent decade, the theoretical calculations of the $t\bar{t}$ cross section were making significant progress. Starting from the NLO calculation with precision of about 10%, it is known now at the NNLO order and reached a precision of about 3%, see Table 2.3. In the same time, D0 measurements were improving as well. First of all, more data have been accumulated and analyzed by the D0 experiment. Analysis techniques have been also improved. Table 2.4 summarizes the cross section measurement at D0 in the dilepton final state, combinations with ℓ+jets final state and combinations with the CDF measurements. In the first measurement, precision has been limited by the statistics, especially in the dilepton channel. In the latest measurements, precision is limited the systematic uncertainties. In this context, we decided to use a nuisance parameter fit, the experimental technique to improve the systematic uncertainty. This technique is similar to the likelihood profiling technique used in the Tevatron Higgs search [44] and explained below.

To measure the cross section in the dilepton channel, we use a discriminating variable to separate signal and background. For example, in [55], such a discriminating variable is a b-quark tagging NN discriminant, see Fig. 2.7. We measure the $t\bar{t}$ cross section $\sigma_{t\bar{t}}$ by simultaneous fit of the NN distributions in all channels and maximize the likelihood function

$$\mathcal{L} = \prod_i \prod_j P[n_{ij}, \mu_{ij}(\sigma_{t\bar{t}})] \ , \tag{2.6}$$

where i runs over the channels and j over the bins of the NN distribution. $P[n, \mu(\sigma_{t\bar{t}})]$ is the Poisson probability function to observe n events when $\mu(\sigma_{t\bar{t}})$ events are expected. The expected probabilities are calculated using the MC distributions. In order to reduce

Measurement	Year	Int. Luminosity	Result	Precision
$\ell\ell$ + ℓ+jets, D0 + CDF, [54]	2014	up to 8.8 fb^{-1}	7.60 ± 0.41 pb	$\pm 5.4\%$
$\ell\ell$ + ℓ+jets, [55]	2011	5.4 fb^{-1}	$7.56^{+0.63}_{-0.56}$ pb	$\pm 8\%$
$\ell\ell$, [55]	2011	5.4 fb^{-1}	$7.36^{+0.90}_{-0.79}$ pb	$^{+12\%}_{-11\%}$
$\ell\ell$ + ℓ+jets, [56]	2009	1 fb^{-1}	$8.18^{+0.98}_{-0.87}$ pb	$^{+12\%}_{-11\%}$
$\ell\ell$ [42]	2009	1 fb^{-1}	$7.5^{+1.4}_{-1.3}$ pb	$^{+18\%}_{-17\%}$
$\ell\ell$ [57]	2007	425 pb^{-1}	7.8 ± 1.8 pb	$\pm 23\%$

Table 2.4: Measured $t\bar{t}$ cross section in the $\ell\ell$ final state and in combination with ℓ+jets final state at D0.

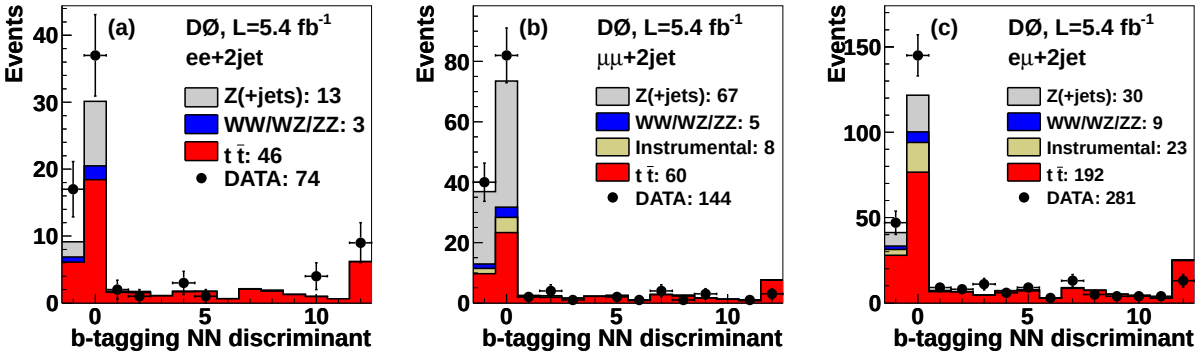

Figure 2.7: $t\bar{t}$ cross section measurement in the dilepton channel [55], for 5.4 fb^{-1}. Expected and observed distributions for the smallest b-tagging NN discriminant output of the two leading jets for the (a) ee + 2 jets, (b) $\mu\mu$ + 2 jets and (c) $e\mu$ + 2 jet channels. The $t\bar{t}$ signal is normalized to the SM cross section (7.45 pb). The x axis represents the NN output non-uniformly mapped to 14 bins. The bin with central value 0 represents the lowest probability for a jet to be produced by a b quark. The bin with value 12 represents the highest probability. The bin with value -1 represents the jets which do not satisfy the requirements to enter the NN computation (non-taggable jets).

the influence of systematic uncertainties on the measurement, the overall uncertainty can be constrained using the same discriminant distribution. For this, the likelihood (Eq. 2.6) is multiplied by the probability related to the systematic uncertainty:

$$\mathcal{L} = \prod_i \prod_j P[n_{ij}, \mu_{ij}(\sigma_{t\bar{t}}, \nu_k)] \prod_k \mathcal{G}(\nu_k; 0, SD), \tag{2.7}$$

where $\mathcal{G}(\nu_k; 0, \mathrm{SD})$ denotes the Gaussian probability density with mean at zero and width corresponding to one standard deviation (SD) of the considered systematic uncertainty k. The free parameters of the fit are ν_k and $\sigma_{t\bar{t}}$. Correlations of systematic uncertainties between channels are naturally taken into account by assigning the same nuisance parameter to the correlated uncertainties. Such an approach usually allows to improve the systematic uncertainty by about 20%.

The cross section measurement described above, in fact, doesn't measure the cross section itself, but the product of $\sigma_{t\bar{t}} \times \mathcal{B}(t \to Wb)$, in which we assume the branching ratio of top quark to W boson and b-quark, $\mathcal{B}(t \to Wb)$, is equal to one. The decay rate of the top quark into a W boson and a down-type quark q ($q = d, s, b$) is proportional to $|V_{tq}|^2$, the squared element of the Cabibbo Kobayashi Maskawa (CKM) matrix [5, 58]. Under the assumption of a unitary 3×3 CKM matrix, $|V_{tb}|$ is highly constrained to $|V_{tb}| = 0.999152^{+0.000030}_{-0.000045}$ [59], and the top quark decays almost exclusively to Wb. The

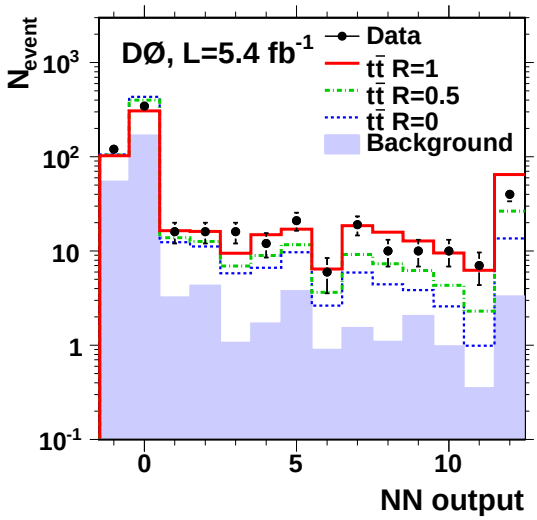

Figure 2.8: R measurement in the $\ell\ell$ and ℓ+jets channel [61], 5.4 fb^{-1}. Distribution in the minimum b-tag NN output of the two jets for dilepton final states.

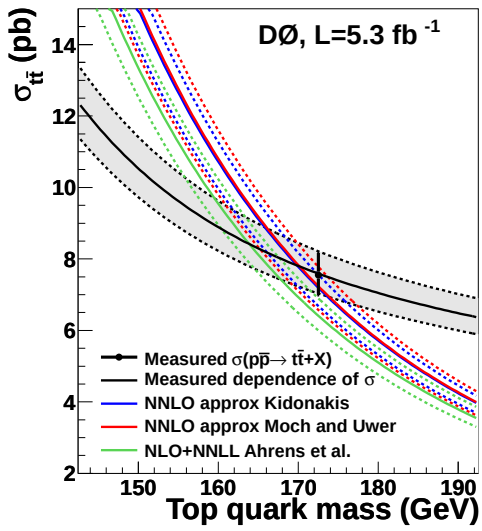

Figure 2.9: Dependence of the experimental [55] and theoretical [46–50] $t\bar{t}$ cross sections on m_t. The colored dashed lines represent the uncertainties on the theoretical calculations. The data point shows the combined $\ell\ell$ and ℓ+jets cross section measurement for $m_t = 172.5$ GeV, the black curve is the experimental $t\bar{t}$ cross section as a function of m_t, and the gray band corresponds to the total experimental uncertainty.

existence of a fourth generation of quarks would remove this constraint and accommodate significantly smaller values of $|V_{tb}|$. A smaller value of $|V_{tb}|$ could be observed directly through the electroweak production of single top quarks, for which the cross section is proportional to $|V_{tb}|^2$, and could also affect the decay rates in the $t\bar{t}$ production channel. The latter can be used to extract the ratio of branching fractions R:

$$R = \frac{\mathcal{B}(t \to Wb)}{\mathcal{B}(t \to Wq)} = \frac{|\ V_{tb}\ |^2}{|\ V_{tb}\ |^2 + |\ V_{ts}\ |^2 + |\ V_{td}\ |^2}\ . \tag{2.8}$$

Given the constraints on the unitary 3×3 CKM matrix elements, R is expected to be $0.99830^{+0.00006}_{-0.00009}$. Along with a measurement of $|V_{tb}|$ using single top quark production, the measurement of R provides the possibility of a study of $|V_{tq}|$ [60].

In [61] we measured R both in $\ell\ell$ and ℓ+jets final states using the same selection, data set and output discriminant distribution as in the cross section measurement [55]. The estimation of the probability of decays with light quarks ($q_l = d, s$) $t\bar{t} \to W^+bW^-\bar{q}_l$ and $t\bar{t} \to W^+q_lW^-\bar{q}_l$ (q_lq_l) are done by fitting the output discriminant distribution with the corresponding MC templates, Fig. 2.8. The result of the measurement is

$$R = 0.90 \pm 0.04\ \text{(stat+syst)}.$$

If we assume unitarity of the CKM matrix, this result can be reinterpreted as the measurement of $|V_{tb}| = 0.95 \pm 0.02$. Using the Feldman-Cousins approach [62] we obtain the intervals in R as 0.82–0.98 and V_{tb} as 0.90–0.99 at 95% CL. This result shows slight tension with the SM expectation, but is compatible with the SM at the 1.6% level.

Theoretical prediction	m_t^{pole}	$m_t^{\overline{\text{MS}}}$
NLO, Nadolsky et al. [36]	$164.8^{+5.7}_{-5.4}$	
NLO+NLL, Cacciari et al. [51]	$166.5^{+5.5}_{-4.8}$	
NLO+NNLL, Ahrens et al. [46, 47]	$163.0^{+5.1}_{-4.6}$	$154.5^{+5.0}_{-4.3}$
appr. NNLO, Moch and Uwer [48, 49]	$167.5^{+5.2}_{-4.7}$	$160.0^{+4.8}_{-4.3}$
NNLO, Kidonakis [50]	$166.7^{+5.2}_{-4.5}$	

Table 2.5: Measured pole (m_t^{pole}) and $\overline{\text{MS}}$ ($m_t^{\overline{\text{MS}}}$) top quark mass from the $t\bar{t}$ cross section [63]. The combined experimental and theoretical uncertainties are shown.

One of the applications of the cross section measurement is the determination of the top quark mass. The measured cross section has a very mild dependence on the mass due to acceptance effects, see Fig. 2.9. Theoretical predictions for the cross section have a much more stronger dependence. Comparing the experimental dependence to the theoretical one, it is possible to determine the most probable top mass from the cross section. Table 2.5 shows the results of such a determination from [63]. This determination allows to extract the top quark mass in a well defined renormalization scheme and could be done both in pole and $\overline{\text{MS}}$ schemes. This determination suffers from larger uncertainties compared to the direct measurements, but as will be explained latter, in section 2.5, has an advantage to be better defined from the theoretical point of view.

2.4 Matrix Element Method

In this section we discuss the matrix element (ME) method. This important experimental technique has been introduced for the first time in the top quark analysis by D0 in 2004 [64]. In this publication D0 reanalysed the data collected during D0 Run I data taking period (1992 – 1996 with an integrated luminosity of 125 pb^{-1}) and remeasured the top quark mass. Use of this technique allows to improve the statistical precision of the mass measurement by about 20%, from 5.2 GeV [65] to 4.3 GeV. The similar level of improvement is reached when D0 measures the top quark mass in the dilepton final state. For example, in [66] D0 measured the mass using the template based method, neutrino weighting technique, using the integrated luminosity of 5.4 fb^{-1}and obtained the statistical uncertainty of 2.4 GeV. With the same data set, the use of the matrix element technique allowed to improve the statistical uncertainty by about 30% and reached the precision of 1.8 GeV [67]. This technique can be also used to distinguish between the signal and background events, like in the single top searches at the Tevatron [68], or to separate two different hypotheses for the signal events as in the measurement of the spin correlation strength by D0 [69, 70].

For the top quark mass measurement the ME technique associates to each event a probability calculated as

$$P(x, m_t) = f_{t\bar{t}} \cdot P_{t\bar{t}}(x, m_t) + (1 - f_{t\bar{t}}) \cdot P_{bckg}(x), \tag{2.9}$$

where $f_{t\bar{t}}$ is the fraction of the $t\bar{t}$ events in the selected data set, $P_{t\bar{t}}(m_t)$ and P_{bckg} are the per-event probabilities calculated for the hypothesis that the selected event is a $t\bar{t}$ event with the top quark mass m_t or it is a background event. x represents the measured parameters, i.e. p_T, η and ϕ for jets and leptons. The probability $P_{t\bar{t}}(x, m_t)$ is calculated as an integral

$$P_{t\bar{t}}(x, m_t) = \frac{1}{\sigma_{obs}(m_t)} \int f_{PDF}(q_1) f_{PDF}(q_2) dq_1 dq_2 \times \frac{(2\pi)^4 |\mathscr{M}(y, m_t)|^2}{q_1 q_2 s} W(x, y) d\Phi^6. \tag{2.10}$$

Here q_1 and q_2 represent the fraction of proton and antiproton momentum carried by the initial state partons, f_{PDF} represents the parton distribution functions, s is the square of the $p\bar{p}$ center-of-mass energy, y refers to the vector of the partonic final state particles four-momenta, $W(x, y)$ are the detector transfer functions, corresponding to the probability to reconstruct vector y as x. For the ME calculation, the LO matrix elements $\mathscr{M}(y, m_t)$ of the processes $q\bar{q} \to t\bar{t} \to W^+W^-b\bar{b} \to \ell^\pm\nu_\ell q q' b\bar{b}$ (for ℓ+jets final state) or $q\bar{q} \to t\bar{t} \to W^+W^-b\bar{b} \to \ell^+\ell^-\nu_\ell\bar{\nu}_\ell b\bar{b}$ (for $\ell\ell$ final state) are used. The gg matrix element is usually ignored, because it contributes only at the level of 15% at the Tevatron and an attempt of adding such ME doesn't improve the precision of the method. $d\Phi^6$ is the six-body phase space

$$d\Phi^6(q_1 + q_2; p_1, \ldots, p_6) = \delta^4((q_1 + q_2)s - \sum_{i=1}^{6} p_i) \prod_{i=1}^{6} \frac{d^3 p_i}{(2\pi)^3 2E_i} \ . \tag{2.11}$$

$\sigma_{obs}(m_t)$ is the $t\bar{t}$ observed cross section, which accounts for the efficiency of the selection and calculated with matrix element $\mathscr{M}(y, m_t)$. The probabilities is summed over two possible jet-parton assignments and over up to two real solutions for each neutrino energy.

In the calculation, we assume a perfect measurement of the leptons and jets directions and a perfect measurement of the electron energy. These assumptions replace the corresponding transfer functions $W(x, y)$ with delta distributions $\delta(x - y)$ and reduce the number of integration dimensions. In the $\ell\ell$ final state we integrate over 8 directions

as shown in the table 2.6 plus one additional integration per muon in the final state[3]. The main drawback of the ME method is the integration time, in spite of using the MC

6 final state partons (2 b-quark, 2 leptons, 2 neutrinos):	24
6 known masses for the final state partons;	-6
2×2 jet directions:	-4
2×2 lepton directions:	-4
remaining dimensions:	10
perfectly measured electron energy:	$n_{\text{electrons}}$
remaining dimensions:	$10 - n_{\text{electrons}}$

Table 2.6: The number of dimensions in the $t\bar{t}$ probability integration for $\ell\ell$ events.

method for the integration[4]. In the first D0 ME top mass measurement in the $\ell\ell$ final state [67], we chose the following integration variables: b-quarks momenta, W-bosons masses, differences between neutrino transverse momenta (x and y components), radii of curvature ($1/p_t$) of muons, and x and y components of the transverse momentum of the $t\bar{t}$ system. Such choice of variables simplifies the resolution of the $t\bar{t}$ kinematic equations and calculation of other kinematic parameters. With this choice of variables the typical integration time is at the order of several minutes per event (on a modern "PC" computer). Choice of the masses of two top quarks as integration variables complicates significantly the resolution of kinematic equations and Jacobian calculation, but samples the integration space in a more optimal manner and reduces the number of integration calls. It was a generally accepted opinion that complication in the calculations will absorb the potential gain due to the more optimal integration sampling. Since the main limiting factor in the first dilepton ME mass measurement was the integration time, we decided to verify this statement and try to speed-up the integration. In fact, this opinion was found to be wrong. After different studies, we chose as the integration variables the two top quark masses, two W-boson masses, p_T of two b-quarks, muon $1/p_t$, and the absolute value and azimuthal angle ϕ of the $t\bar{t}$ transverse momentum. We found that a gain due to the reduction of the numbers of integration calls largely surpasses the losses in time due to the resolution of the kinematic equations. We obtained a reduction of the integration time by a factor of 100. This is an important advance in use of the ME method at D0 in the $\ell\ell$ channel. This integration speed-up allows to integrate the much larger set of MC events, which is the necessary condition for the analysis of the full D0 data set.

To measure the top quark mass, the probability $P(x, m_t)$ is calculated over a range of top quark masses for each event, and the log-likelihood function is calculated for the set of events $i = 1 \,..\, n$:

$$\mathscr{L} = -\sum_{i=1}^{n} \ln(P(x_i, m_t)) \ . \tag{2.12}$$

The minimum of this function, determined by the fit, is used as the measured mass. Statistical uncertainty on the measurement is given by the 68% confidence region around the measured value, i.e. by the mass difference at $\mathscr{L}_{min}$ and $\mathscr{L}_{min} + 0.5$. The measured value is calibrated with the ensemble testing technique using the simulated events as pseudo-data. Additional details about the use of ME method can be found in [74, 75].

[3]In the D0 detector, the muon p_T resolution is approximately three times worse than the electron energy resolution. That is why we replace the electron energy transfer function with a delta-distribution, but integrate over muon p_T.

[4]In the D0 dileptons analyses we use the VEGAS [71, 72] algorithm for the MC integration, as implemented in the GNU Scientific Library (GSL) [73].

Another variant of the matrix element technique is used in the $t\bar{t}$ spin correlation analysis at D0, [69, 70]. We calculate the spin correlation discriminant [76]:

$$R = \frac{P_{t\bar{t}}(corr)}{P_{t\bar{t}}(corr) + P_{t\bar{t}}(uncorr)} ,$$

where $P_{t\bar{t}}$ is a per-event probability calculated similar to the equation (2.10) for the hypotheses: $\mathscr{H} = corr$, when spins of the top quark and antiquark are assumed to have the SM correlation, $\mathscr{H} = uncorr$, when spins are assumed to be not correlated. These probabilities are calculated as

$$P_{t\bar{t}}(x, \mathscr{H}) = \frac{1}{\sigma_{obs}} \int f_{PDF}(q_1) f_{PDF}(q_2) dq_1 dq_2 \times \frac{(2\pi)^4 |\mathscr{M}(y, \mathscr{H})|^2}{q_1 q_2 s} W(x, y) d\Phi^6. \quad (2.13)$$

Here the LO matrix element $\mathscr{M}(y, \mathscr{H})$ is calculated according to the spin correlation hypothesis $\mathscr{H}$. For the $\mathscr{H} = corr$, the matrix element is averaged over the color and spins of the initial partons, and summed over the final-state color and spins. For the $\mathscr{H} = uncorr$ we use the same matrix element, but neglect the $t\bar{t}$ spin correlation part [77, 78]. A template fit of the R-distribution is used to extract the fraction of events with SM spin correlation and translate it to the spin correlation strength. The use of the ME technique at D0, allowed to improve the sensitivity of the measurement with respect to the one-dimensional distribution fit [79] by almost 30% [69] and to produce the first evidence for the correlation of spins of top quark and antiquark in $t\bar{t}$ production at the Tevatron [70].

We developed a different way of using the ME approach for the $t\bar{t}$ asymmetry measurement in the dilepton final state [80]. In this approach the formula (2.10) is replaced with the following:

$$\frac{dP_{t\bar{t}}(x)}{dv} = \frac{1}{\sigma_{obs}(m_t)} \frac{d}{dv} \int f_{PDF}(q_1) f_{PDF}(q_2) dq_1 dq_2 \frac{(2\pi)^4 |\mathscr{M}(y, m_t)|^2}{q_1 q_2 s} W(x, y) d\Phi^6, \quad (2.14)$$

where v is any chosen variable and $\frac{dP_{t\bar{t}}(x)}{dv}$ is a probability density as a function of the variable v, calculated for a given set of measured parameters x. Technically, this distribution is calculated using original sampling, provided by the MC integration algorithm, which randomly generates the set of parameters (y') for the integration variables. For each set of parameters, the probability $P_{t\bar{t}}(x, y')$ is calculated and stored in the 1D histogram for the parameter v, weighted by the appropriate normalization factors. In such a way, a probability density histogram corresponds to a generated parameter for an individual event. The obtained histograms for each events are normalized to one and are summed together. Correlations between reconstructed and MC generated histograms for several $t\bar{t}$ parameters are shown in Fig. 2.10. The developed approach has an advantage for the under-constrained kinematics (like in the dilepton final state), that it takes into account all possible solutions by using the probability density histograms and maximizes the statistical precision of the results. It is possible to use a value with the highest probability to estimate the true parameter, but inevitably the precision of such an estimator will be worse due to the information loss. In the framework of the asymmetry analysis, [80], we showed that use of the probability density histograms reduces the statistical uncertainty by about 20% in the measurement of $t\bar{t}$ asymmetry.

As was mentioned several times, the ME technique allows to improve significantly the precision of the measurement. What is the reason for it? The usual answer that this technique uses the full available information in the event, i.e. all measured particle

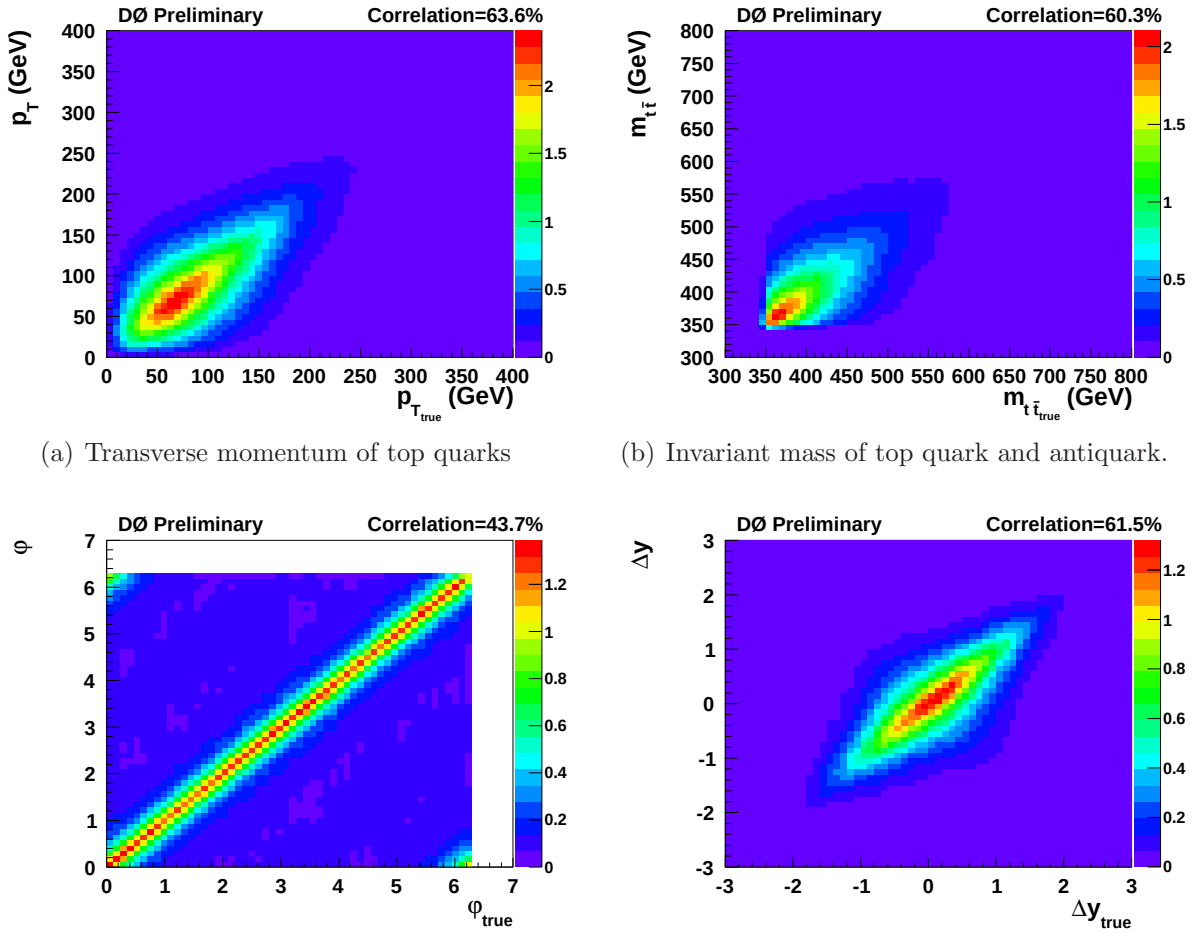

(a) Transverse momentum of top quarks

(b) Invariant mass of top quark and antiquark.

(c) Azimuthal angle ϕ of top quark or antiquark.

(d) Difference in rapidity dy between top quark and antiquark.

Figure 2.10: $t\bar{t}$ asymmetry measurement in the dilepton channel [80], 9.7 fb^{-1}. Reconstructed parameters of $t\bar{t}$ system versus generated ones.

energies and angles. This is only a partially correct answer. From our point of view, the most important reason is of statistical nature. As shown by equation (2.12), each event contributes to the likelihood with a different weight. This weight is proportional to the difference between the minimal likelihood value and values with different m_t. For example, event with a flat likelihood function in m_t has no minimum and adds no information about the top quark mass, so it will not improve the overall precision.At the same time, events with a good separation will contribute more to the overall likelihood. How sensitive an individual event is determined by several factors. One of them is the detector resolution, which is encoded in the transfer functions. For example, better detector resolution leads to narrow transfer functions and, in consequence, to a more pronounced difference in the likelihood values for the different top quark masses. The matrix element improves the sensitivity, because it enhances the probabilities and corresponding weight for the events which "look like" the $t\bar{t}$. For example, configurations with the invariant mass of lepton and neutrino close to the W-boson mass, will have enhanced probabilities due to the Breit-Wigner resonance behaviour of the matrix element. To conclude, the ME method associates to each event a weight, and this weight is larger for events being in agreement with a $t\bar{t}$ configuration and well reconstructed in the detector. This is not the case for the template based method. In this method, each event is contributing equally to the fit and hence the information from the signal-like, more precisely measured events

is diluted by events measured with worse precision. Similar reasons are also valid for the use of the ME method for the separation of two hypotheses, like in the spin correlation measurement, or separation of signal events from background, but in this case, there is an alternative, the use of multivariate approaches, for example, decision trees, neural networks etc., [81]. We believe that even in comparison with the multivariate approaches, there are some advantages in use of ME technique. First of all, the recipe, how to construct the discriminant, is known. There is no need to test many different variables and many different MVA configurations, as it is the case for the multivariate techniques. The second reason is that the discriminant behaviour can be analyzed from the physics point of view and is more predictable and understandable, as opposite to the MVA, which is often considered as a "black-box".

We would like to conclude the description of the ME method by discussing the possibility to use it in the LHC experiments. As was mentioned before, the weakest point of the ME technique is its strong demand for computer CPU resources. the LHC $t\bar{t}$ analyses the number of events is a factor of thousand larger than in the Tevatron measurements, so at first look, the use of ME seems to be difficult at the LHC. At the same time, for most of the analyses at LHC, the statistical precision is not a limiting factor, so there is no need to improve it. On the other side, LHC experiments have a possibility to study the rare processes, like $t\bar{t}H$, $t\bar{t}t\bar{t}$. For these analyses, the statistical precision does matter and the number of events after the preselection is not too large. For sure, those measurements potentially could profit from the use of the ME method, and there is an example for its successful application at the LHC, [82]. It is also important to mention that there are many possibilities to accelerate the ME technique, as shown by the D0 experiment. For example, in both $\ell\ell$ and ℓ+jets final configurations the speed of the ME technique at D0 was improved by a factor of one hundred. The important points to consider for the acceleration of the technique are the following.

- The optimal choice of the integration variables.
- The possible factorization of the probabilities calculations, e.g. see [83, 84] for the JES correction parameter factorization.
- The use of the quasi-random number generation instead of pseudo-random numbers, see [83–85].

Quite recently the development of new approaches were started for automatizing the ME technique and use of the NLO matrix elements [86, 87]. All these improvements give the possibility to use the ME approach to analyze larger data sets at the LHC and at future experiments at e^+e^- colliders.

2.5 Top Quark Mass Measurement

The top quark mass (m_t) is a free parameter of the SM Lagrangian and can't be predicted from first principles. On the other hand, the top quark influences the electroweak observables via self-energy and vertex corrections, e.g. the forward-backward asymmetry in Z-boson decays $Z \to b\bar{b}$ or the ratio $R_b = \Gamma_Z^{b\bar{b}}/\Gamma_Z^{\text{hadrons}}$. The precise experimental measurements in the electroweak sector allow to indirectly constrain the top quark mass. For the first time such determinations of the top quark mass were done before its discovery, as demonstrated in the Fig. 2.11 from [88]. The top quark discovery in 1995 confirmed these determinations.

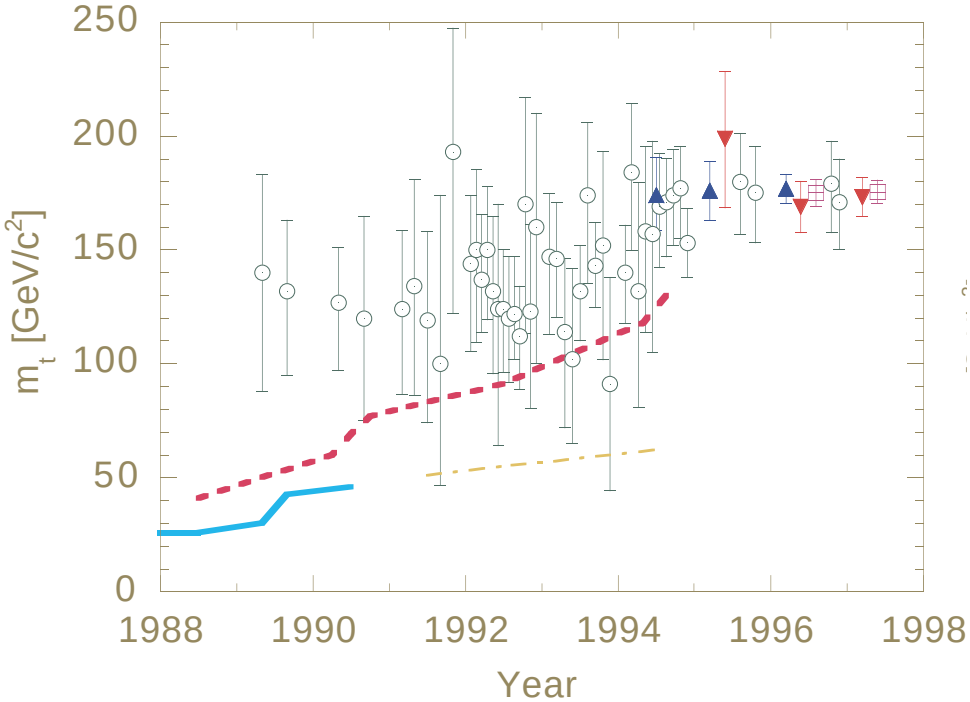

Figure 2.11: From Ref. [88]. Indirect determinations of the top-quark mass (open circles) and 95% confidence-level lower bounds on the top-quark mass from direct searches in e^+e^- (solid line) and $p\bar{p}$ collisions (broken line). An indirect lower bound, derived from the W-boson width is shown as the dot-dashed line. Direct measurements of m_t are shown as triangles for CDF and inverted triangles for D0. The world average in 1997 from direct observations is shown as the crossed box.

The current global electroweak fit constrains the top quark mass to the interval $[172, 190]$ GeV (1σ) if the Higgs boson mass measurement is ignored, see Fig. 2.12(a), [89, 90] and is in good agreement with the direct measurements. The more stringent test of the SM could be done by including the measured Higgs boson mass. The W-boson mass, M_W, is related to the top quark mass, m_t, and Higgs boson mass, M_H, via the radiative correction function Δr, [91]:

$$M_W^2 = M_Z^2 \left\{ \frac{1}{2} + \sqrt{\frac{1}{4} - \frac{\pi\alpha}{\sqrt{2}G_\mu M_Z^2}\left[1 + \Delta r(M_W, M_Z, M_H, m_t, \ldots)\right]} \right\}, \tag{2.15}$$

where α and G_μ are the fine structure and Fermi constants, m_Z is the Z-boson mass. The correction function is quadratically dependent on the top quark mass , $\Delta r \sim m_t^2$, and logarithmically on the Higgs boson mass, $\Delta r \sim \ln M_H^2/M_Z^2$. The precision of the indirect determination of the top quark mass is improved by a factor of five, when one accounts

Measurement	Year	Int. Lumi	Result in GeV	Precision
D0, CDF [2]	2014	≤ 9.7 fb^{-1}	$174.34 \pm 0.37 \pm 0.52$	$\pm 0.37\%$
D0, CDF, ATLAS, CMS, [92]	2014	≤ 8.7 fb^{-1}	$173.34 \pm 0.27 \pm 0.71$	$\pm 0.44\%$
ℓ+jets, D0, ME [83]	2014	9.7 fb^{-1}	$174.98 \pm 0.60 \pm 0.49$	$\pm 0.43\%$
$\ell\ell$, D0 , ME + NW, [66]	2012	5.4 fb^{-1}	$173.9 \pm 1.9 \pm 1.6$	$\pm 1.4\%$
$\ell\ell$, D0 , ME, [67]	2011	5.4 fb^{-1}	$174.0 \pm 1.8 \pm 2.4$	$\pm 1.8\%$
ℓ+jets, D0, ME [95]	2011	3.6 fb^{-1}	$174.94 \pm 1.14 \pm 0.96$	$\pm 0.85\%$
$\ell\ell$, D0 , NW+MW, [96]	2009	1.0 fb^{-1}	$174.7 \pm 4.4 \pm 2.0$	$\pm 2.8\%$
ℓ+jets, D0, ME [97]	2008	1.0 fb^{-1}	$171.5 \pm 1.8 \pm 1.1$	$\pm 1.2\%$

Table 2.7: The selected kinematic top quark mass measurement at D0. The first uncertainty in the result column is the statistical uncertainty, the second one is the systematic uncertainty. ME means matrix element technique, NW is a neutrino weighting and MW is a matrix weighting template techniques.

for the measurement of the Higgs boson mass in the fit. The best fitted value of m_t is found to be $m_t = 177.0^{+2.3}_{-2.4}$ [89], Fig. 2.12(a). It has a 1.5σ difference with the Tevatron and LHC combination of $m_t = 173.34 \pm 0.76$ GeV/c^2 [92], but the interpretation of this difference is a subtle point for reasons related to the nature of the measured top quark mass and will be discussed later in this section. The relation (2.15) can be inverted and used as a prediction of the Higgs boson mass, which gives the famous plot, Fig. 2.12(b) and shows the self-consistency of the SM.

Another interesting point related to the top quark mass is the stability of the electroweak vacuum in the SM. The relation between Higgs quartic coupling, λ, and the Higgs boson mass, M_H can be written as [93]:

$$\lambda(\mu) = \frac{G_\mu M_H^2}{\sqrt{2}} + \Delta\lambda(\mu), \tag{2.16}$$

where μ is the renormalization scale. The threshold correction term $\Delta\lambda(\mu)$ depends mainly on the value of the top quark mass. A too heavy top quark will lead to a negative λ at high scales and the possibility for the vacuum to "tunnel" to a new minimum, leading to the instability of the SM vacuum. Of course, such interpretation requires the validity of the SM up to the Plank scale. The NNLO calculation of the $\Delta\lambda(\mu)$ term [93] shows that the Higgs quartic potential is vanishing at the Planck scale and our Universe happens to be exactly on the border between the stable and unstable region of the SM vacuum, Fig. 2.13. Such a remarkable feature stimulated many theoretical speculations about the reason hidden behind such criticality of the SM parameters, see, e.g. [94]. It should be noticed that any statement about the stability or instability of the SM requires the careful investigation of the theoretical and experimental uncertainties, especially, those related to the measurement of the most critical parameter, the top quark mass. As will be pointed out at the end of this section, the top quark mass is measured extremely precisely at the Tevatron and LHC, but the uncertainties related to this measurement are not always well defined.

At D0, the top quark mass is measured in the ℓ+jets and $\ell\ell$ final state. Table 2.7 summarizes the most recent measurements by the D0 collaboration and combinations with other experiments. The most precise measurements are obtained in the ℓ+jets channel, but analyses in the $\ell\ell$ channel are also important because they allow to cross-check the systematic uncertainties on the top quark mass measurement in an environment with

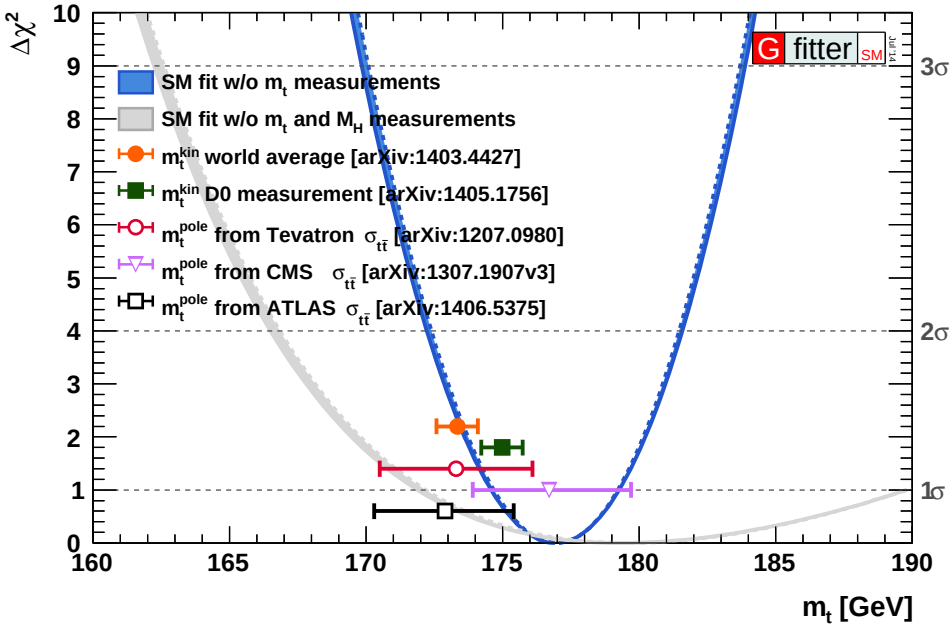

(a) $\Delta\chi^2$ as function of the top quark mass m_t, shown as blue band (the direct m_t measurements are excluded). The grey bands represents the result of the fit without the Higgs boson mass measurements.

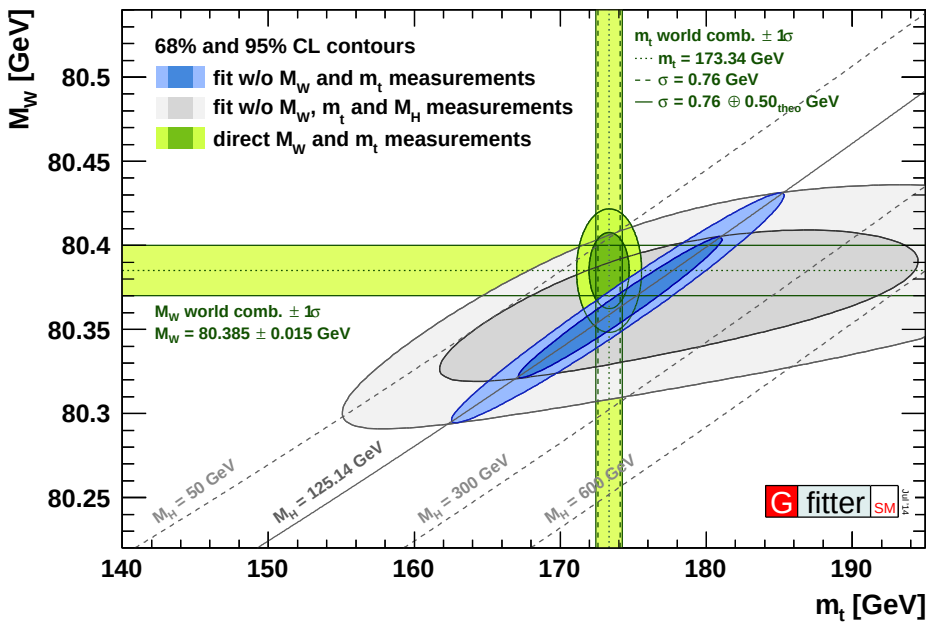

(b) Contours of 68% and 95% confidence level obtained from scans of fits with fixed variable pairs W-boson mass versus top quark mass. The narrower blue and larger grey allowed regions are the results of the fit including and excluding the Higgs boson mass measurements, respectively.

Figure 2.12: Results of the global electroweak fit. Gfitter collaboration [89, 90].

a smaller number of jets. Additionally, methods and techniques, developed for the $\ell\ell$ channels, could be applied to the LHC dilepton measurements, which are not limited by the statistics of the data set and could compete with the ℓ+jets measurements.

In Ref. [67] for the first time at D0, we used the ME technique for the mass measurement in the dilepton final state. As described in section 2.4, we measure m_t by finding

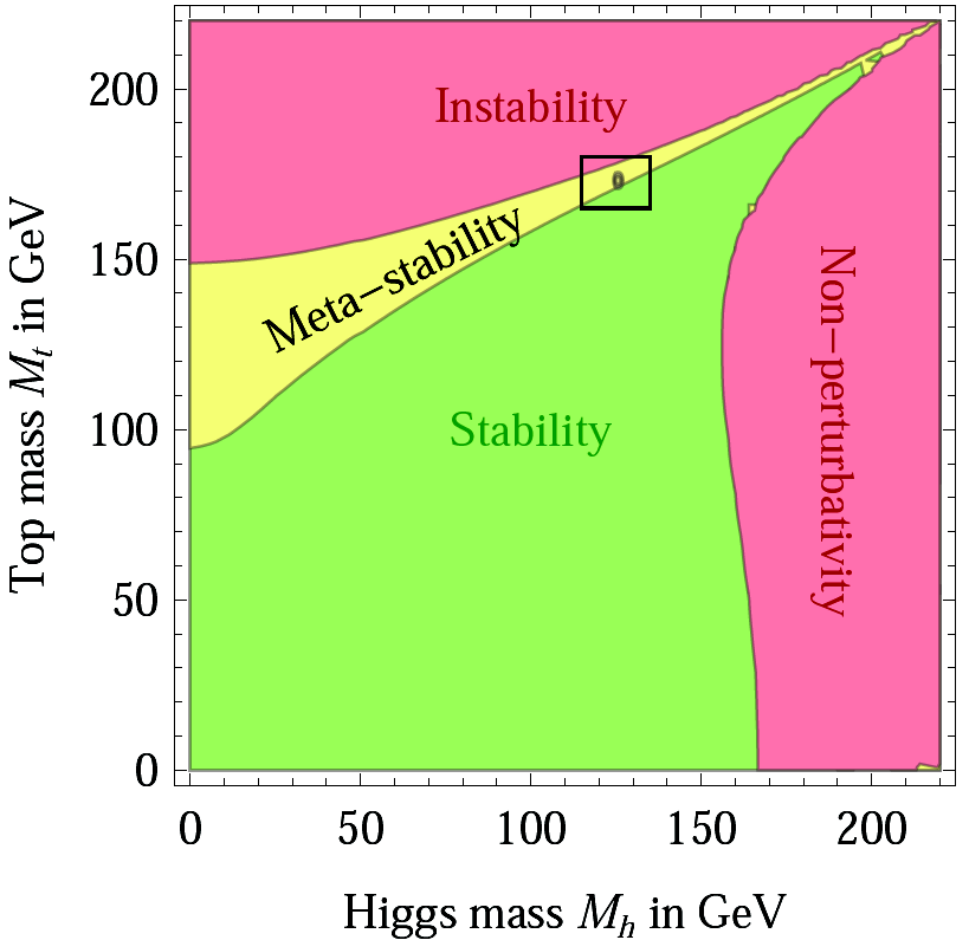

Figure 2.13: Regions of absolute stability, meta-stability and instability of the SM vacuum in the m_t vs M_H plane from [93].

a minimum of the likelihood function (2.12). We calibrate the method, in order to check for any bias caused by approximations, such as the use of the LO matrix element for the $t\bar{t}$ probability (2.10) or simplified description of the detector response in the transfer functions. The measurement is calibrated using MC events generated with ALPGEN [33] + PYTHIA [34]. Five $t\bar{t}$ MC samples are generated with input top quark masses of $m_t = 165$, 170, 172.5, 175, and 180 GeV. Probabilities for the $t\bar{t}$ signal and for $Z/\gamma^\star$, diboson and instrumental backgrounds are used to form randomly a set of events (pseudoexperiments) with a sample composition, similar to the one in data. The total number of events in each pseudoexperiment is fixed to the number of events in data for the combined dilepton channels. The signal and background fractions are fluctuated according to multinomial statistics around the fractions determined from the measured $t\bar{t}$ cross section in the separate channels. The mean values of m_t measured in 1000 pseudoexperiments as a function of the input m_t are shown in Fig. 2.14(a) For the case of background-free pseudoexperiments, no difference is observed. The pull variable, p_i, is defined for the pseudoexperiment i as

$$p_i = \frac{m_i - \langle m \rangle}{\sigma_i}, \tag{2.17}$$

where m_i is a measured top quark mass in the pseudoexperiment i and $\langle m \rangle$ is an average top quark mass for all pseudoexperiments. The width of the pull distribution characterizes the correction to the statistical uncertainty and is shown in Fig. 2.14(b) for this measurement. The statistical uncertainty measured in data is multiplied by the pull width. The calibration procedure described above is extremely important for the understanding of

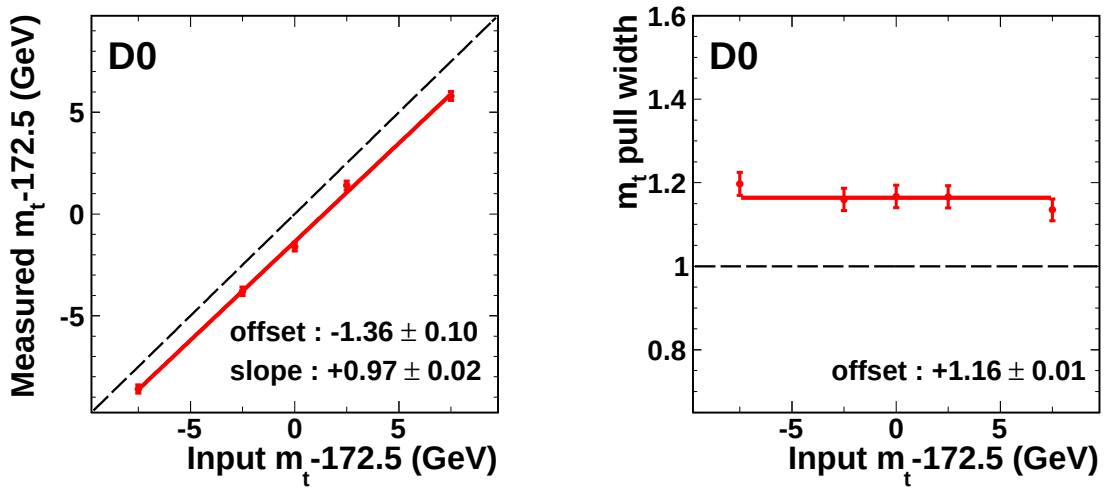

(a) Mean values of the measured top quark mass versus the generated one.

(b) Pull width as a function of generated top quark mass

Figure 2.14: Calibration results for the top quark mass measurement in the dilepton final state, 5.4 fb^{-1}, [67]. The dashed lines represent the ideal response.

the nature of the measured top quark mass. In fact, the measured mass is calibrated with MC in most of the direct measurements, so the measured mass corresponds to the mass as defined in the MC. In case of the D0 experiment, we use the LL MC ALPGEN+ PYTHIA, so the measured mass corresponds to the top quark mass as it is defined in ALPGEN with a low-energy correction from PYTHIA.

The important part of the top quark mass measurements is the estimation of systematic uncertainties. We divide all sources of uncertainties into three categories. The first involves uncertainties from modeling of the detector, such as the uncertainty on the energy scale of light-quark jets and the uncertainty in the relative calorimeter response to b and light-quark jets, as well as in the energy resolution for jets, muons, and electrons. The second category is related to the modeling of $t\bar{t}$ production. This includes possible differences in the amount of initial and final state radiation, effects from next-to-leading-order contributions and different hadronization models, color reconnection, modeling of b-quark fragmentation and uncertainties from the choice of PDF. The third category comprises effects from calibration, such as the uncertainties in the calibration function shown in Fig. 2.14(a), and from variations in signal and background contributions in the pseudoexperiments. Contributions to the total systematic uncertainty in the measurement of m_t are summarized in Table 2.8.

The dominant systematic uncertainty in the measurement [67] arises from the different detector response of light and b-quark jets. It accounts for the different calorimeter response of single particles (pions, kaons etc.) in data and MC simulation and the different fractions of single pions in light and b-quark jets. The relative uncertainty of the response has been evaluated to be 1.8% leading to a shift of 1.6 GeV in m_t. In more recent analyses, the estimation of this difference is improved, by measuring the difference in the single particle response between data and MC using γ+jets and dijets events [30]. The measured difference is applied as a correction to the MC jets, taking into account the individual particle composition of each jet, Fig. 2.15. Uncertainty on this correction is accounted in the systematic uncertainties of the measurement. This procedure allowed to reduce this uncertainty in the ℓ+jets top quark mass measurement to 160 MeV, Table 2.9.

The next important uncertainty comes from uncertainties in the jet energy scale (JES)

Table 2.8: Summary of systematic uncertainties on the measurement of m_t in $\ell\ell$ final state, 5.4 fb^{-1}, [67].

Source	σ, GeV
Signal modeling:	
Higher order and hadronization	±0.7
Color reconnection	±0.1
ISR/FSR	±0.2
b-jet modeling	±0.4
PDF uncertainty	±0.1
Detector modeling:	
b/light jet response	±1.6
JES	±1.5
Jet resolution	±0.3
Lepton p_t scale	±0.4
Muon resolution	±0.2
Method:	
MC calibration	±0.1
Signal fraction	±0.5
Total	±2.4

Table 2.9: Summary of systematic uncertainties on the measurement of m_t in ℓ+jets final state, 9.7 fb^{-1}, [83].

Source	σ, GeV
Signal and Bckg. Modeling:	
Higher order corrections	$+0.15$
Hadronization	$+0.26$
Color reconnection	$+0.10$
ISR/FSR	±0.09
b-jet modeling	$+0.09$
PDF uncertainty	±0.11
Multiple $p\bar{p}$ interactions	-0.06
Heavy flavor scale factor	±0.06
Detector modeling:	
b/light jet response	±0.16
Residual JES	±0.21
Jet resolution	±0.07
Lepton p_t scale	±0.01
b-tagging	±0.01
Method:	
MC calibration	±0.07
Signal fraction	±0.08
Modeling of multijet events	$+0.04$
Total	±0.49

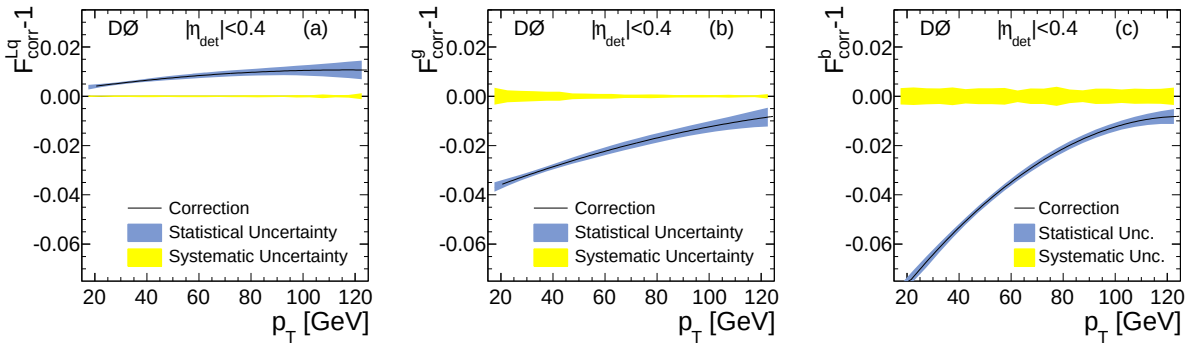

(a) Light quarks (u, d, s, c) (b) Gluons (c) b quarks

Figure 2.15: Correction factor F_{corr} derived using tuned MC single-particle responses for central jets ($|\eta_{det}| < 0.4$) and different jet flavors, [30]. The bands represent the statistical and systematic uncertainties.

of light quarks. This JES is calibrated using γ+jets and dijets events [30] and applied to jets of any flavor. The total uncertainty typically is about 1.5% per jet, Fig. 2.16, which translates into an uncertainty on m_t of 1.5 GeV. In ℓ+jets final states this uncertainty could be significantly reduced by the fact that one of the W-boson decays to two jets and the invariant mass of these two jets is constrained to the W-boson mass. The two-dimensional fit of the top quark mass and the JES correction factor allow to reduce the JES uncertainty. For example, in the most precise D0 measurement, the JES correction factor is found to be $k_{JES} = 1.025 \pm 0.005$ and the residual JES uncertainty is estimated to be 210 MeV, Table 2.9. This JES correction factor is relevant also to the measurements in the dilepton final state. In the more recent D0 measurement in $\ell\ell$ channel (5.4 fb^{-1}, neutrino weighting template technique) the ℓ+jets JES correction factor is applied to jets in the dilepton final state and due to this procedure, the JES uncertainty has been reduced to 950 MeV, [66]. We expect that in the 9.7 fb^{-1} $\ell\ell$ ME measurement, the JES uncertainty will be reduced to 500 MeV or less.

Another important set of uncertainties is related to the modeling of the $t\bar{t}$ events. The following source of uncertainties are considered. Uncertainty related to the higher-order effects, hadronization and underlying events is evaluated by comparing the measured mass using $t\bar{t}$ events generated with MC@NLO [98] + HERWIG [99] with the default ALPGEN+ PYTHIA. This uncertainty is estimated to be around 0.7 GeV. With the reduction of the detector related systematic uncertainties, hadronization and higher-order effects become the most important uncertainty. In addition, this uncertainty considered as 100% correlated between measurements in different experiments, and hence couldn't be reduced in the combination. This leads to a more refined estimation of this uncertainty. In particular, in [83], we estimated separately higher-order effects uncertainty and uncertainty due to the hadronization and underlying events simulation. The higher-order effects uncertainty is estimated by comparing the MC@NLO+HERWIG with ALPGEN+HERWIG. Hadronization uncertainty is estimated by comparing the ALPGEN+HERWIG with ALPGEN +PYTHIA. In order to avoid the double counting with the JES related uncertainties, the hadronization and underlying events uncertainty is evaluated by using the particle jet transverse momenta, i.e. the momenta of jets before any detector interaction and reconstruction. As a result, these uncertainties are estimated to be 150 MeV and 260 MeV respectively, see Table 2.9. The same approach is applied to the 9.7 fb^{-1}dilepton mass measurements.

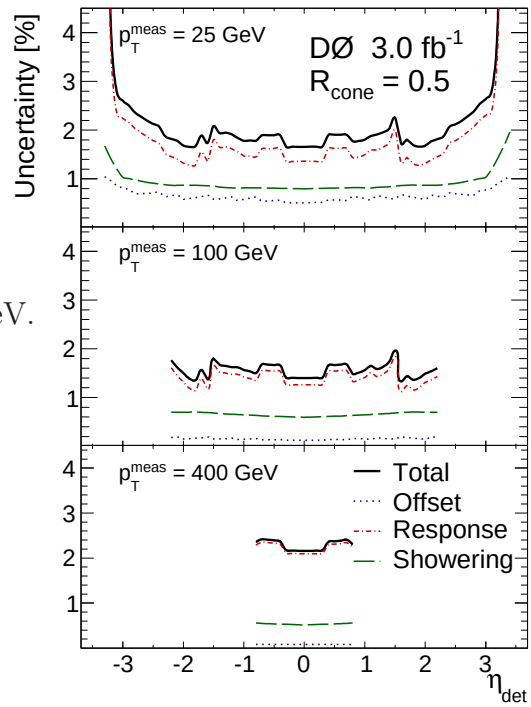

Figure 2.16: D0 JES uncertainty for jets in data as a function of the detector pseudorapidity η_{det} for different uncorrected p_T, [30].

The uncertainty due to the initial and final state radiation is estimated by comparing the Drell-Yan process in data and MC. In the most recent version of this estimation, we change the amount of radiation via the renormalization and factorization scale parameter for the matching scale in ALPGEN interfaced to PYTHIA [100] up and down by a factor

of 1.5. As a reference measurement in data, we use the D0 measurement of the $\phi^{\star}$[5] distribution [102]. A potential effect of color reconnection is evaluated by comparing different MC tunes. For example, for the latest ℓ+jets analysis, [83], we compare events simulated with ALPGEN interfaced with PYTHIA tunes Perugia2011NOCR or Perugia2011, where the latter includes an explicit color reconnection model [103]. Uncertainty due to the description of b-quark fragmentation is estimated by reweighting of the default MC samples to a Bowler scheme tuned to LEP or SLD data [104].

The most precise value of the measured top mass can be achieved by the combination of the results from the different channels and experiments. Such combination is done using the best linear unbiased estimator (BLUE) technique [105, 106]. The validity of the combination depends on the assignment about correlations between the different sources of systematic uncertainties in different measurements. For example, the detector related uncertainties, like JES or measurement method, are usually treated as uncorrelated and are significantly reduced by the combination. The signal modeling uncertainties are usually treated as correlated and can't be reduced by the combination, [107]. The most precise combinations are listed in the Table 2.7. One could remark than the LHC-Tevatron combination [92] is less precise that the Tevatron-only combination [2]. This is related to the fact that the LHC-Tevatron combination doesn't include the recent, most precise D0 measurement [83].

Till early 2014, all top quark mass measurements in different experiments were in surprisingly good agreement and this agreement was often considered to be too good to be true. In 2014 this situation has changed. The D0 collaboration published the measurement of the top quark mass $m_t = 174.98 \pm 0.76$ GeV in ℓ+jets channel with 9.7 fb^{-1} [83] and the CMS collaboration made public a preliminary measurement of $m_t = 172.22 \pm 0.73$ GeV [108]. Those two measurements differ by 2.8 GeV. It is difficult to estimate a significance of this difference without a full combination and proper account of the correlations between uncertainties, but a rough estimation gives a significance of about $(2.5 \div 3.5)\sigma$[6]. Without additional investigation it is difficult to explain such a large difference. It could be of statistical origin, because those measurements are the two measurements with a largest difference, selected from a set of more than twenty measurements. Another possibility is that one or several systematic uncertainties related to the detector effects or to the $t\bar{t}$ signal simulations are underestimated or not accounted for. One can even speculate about the difference being due to different production mechanisms, not fully accounted in the measurement calibration. In any case, this significant difference between measurements stimulated the more careful consideration of the different sources of the systematic uncertainties and special efforts are on-going in the collaborations to understand better the measurement uncertainties.

Up to this point we didn't discuss the definition of the top quark mass. Indeed in the SM, the mass of the particle is a parameter of the Lagrangian, and can be related to the observed or physical mass in different ways. Usually, the mass of a free, stable particle is understood as a physical mass. This mass corresponds to the pole mass, defined as a real part of the particle propagator. The pole mass of a stable particle is a well defined concept in the finite order perturbation theory. This definition is not working well for the top quark, because of the color confinement of the quarks. In other words, the definition

[5] $\phi^{\star}$ is a variable related to the angle between two leptons from $Z/\gamma^{\star}$ decay which is correlated strongly with the $Z/\gamma^{\star}$ p_T. For the definition, see [101, 102].

[6] For this estimation we consider two hypothesis: (1) totally uncorrelated uncertainties; (2) fully correlated systematic uncertainties, but statistical uncertainties and uncertainties related to the JES scale factor are uncorrelated.

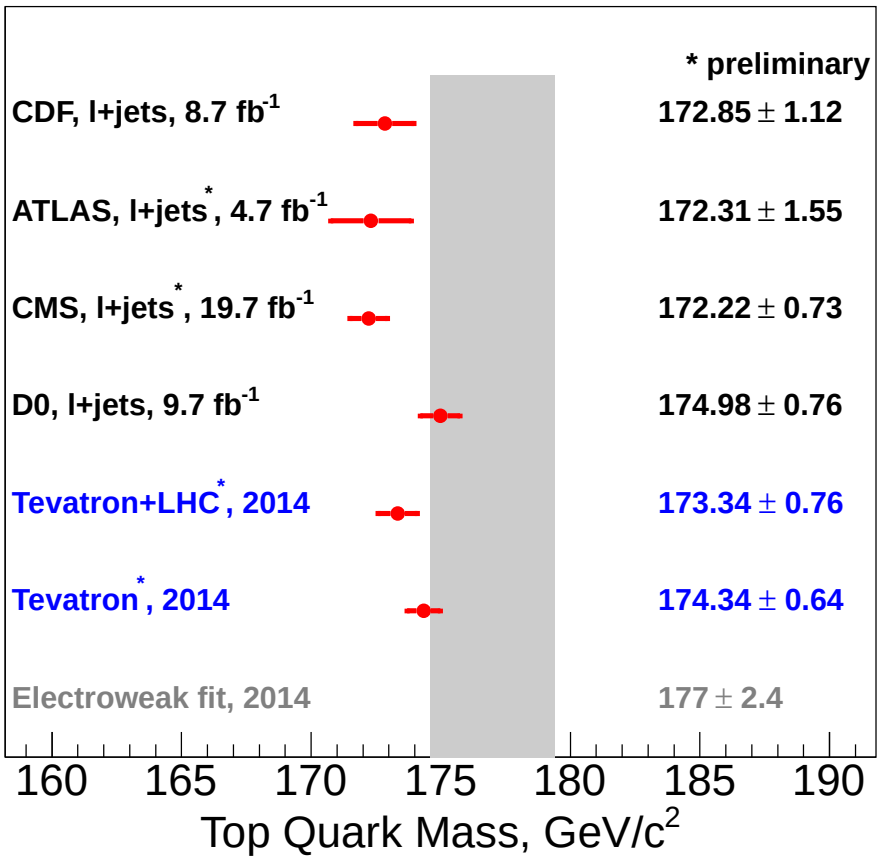

Figure 2.17: The most precise measurement of each of the four experiments, [83, 108–110] and the most recent combinations, [2, 92]. The results of the global electroweak fit [89, 90] is shown as a gray band.

of the top quark mass is ambiguous due to the non-perturbative effects and the scale of the ambiguity is of the order of Λ_{QCD}, see, for example, [111]. Alternatively, a short-distance mass definition could be used, the most often used short-distance mass definition is the one in the minimal subtraction scheme, $\overline{\text{MS}}$. This scheme realizes the concept of a running mass, i.e. the mass parameter is dependent on the renormalization scale μ, $m_t(\mu)$. It can be defined without any additional theoretical uncertainty.

So the natural question arises, what kind of mass is measured in the experiment? As was mentioned before, an unavoidable part of almost all methods based on the final state kinematics is a calibration of the method using the MC generator. This calibration fixes the experimental mass definition with the MC mass definition. The MC generators in use are the tree-level matrix element generators (e.g. ALPGEN, MADGRAPH) or NLO generator (MC@NLO, POWHEG)[7] with non-perturbative hadronization and showering realized by PYTHIA or HERWIG generators. The MC mass is very close to the pole mass definition, but it is not known how close. There are at least two effects which are not accounted for in the MC. Not all NLO diagrams are taken into account. Even in existing NLO generators, the top quark is usually simulated as a stable particle with the following decay to the final state particles, so the NLO diagrams related to the interaction between initial and final particles are not simulated. The second effect is the use of ad-hoc models for the showering

[7]Even if the NLO generators are not used for the mass measurement, they are always used to assign a systematic uncertainty related to the higher order effect. This uncertainty estimate how "far" the reconstructed mass from the MC NLO mass.

and hadronization realized in PYTHIA and HERWIG generators. This non-perturbative part is at least of the order of Λ_{QCD}. In [112, 113] authors stated that: "The uncertainty on the translation from the MC mass definition to a theoretically well defined short-distance mass definition at a low scale is currently estimated to be of the order of 1 GeV". In SM calculations using the pole-mass definition for m_t, the uncertainty is chosen to be $0.3 \div 0.5$ GeV, [89, 94]. From the experimental point of view, the uncertainty on the top quark mass definition is not considered as a systematic uncertainty. It is believed that future theoretical work will allow to clarify and reduce the uncertainty in the definition of the top quark mass in MC and all experimental results could be translated to any new generator with a clear definition of the mass.

Another approach to this problem was pioneered by D0 [56, 114] and consists in measuring the top quark mass using the dependence of the inclusive $t\bar{t}$ cross-section on the mass. This dependence can be calculated using pole or $\overline{\text{MS}}$ definitions of the top quark mass [26, 45, 48, 49]. As was mentioned in section 2.3, this dependence allows to measure the top quark mass with a reduced influence of the MC mass and, hence, to have a measurement with a theoretically clearer m_t definition. Unfortunately, these results have a rather large uncertainty, about 5 GeV in D0 measurement [63], but the precision has been improved in the LHC experiments up to 2 GeV, [115–117].

A revolution in the measurement of the top quark mass could happen at the future e^+e^- colliders. The measurement of the threshold behaviour of the $t\bar{t}$ cross section allows to measure m_t in the threshold short-distance mass scheme. The cross section dependence has been calculated up to the NNLO+NNLL order and the theoretical uncertainty in the determination of the top quark mass is estimated to be about 20 MeV, [118], while the experimental uncertainty could be as good as 100 MeV [119–121].

2.6 Angular Asymmetry in $t\bar{t}$ Production

2.6.1 Introduction

The measurement of the asymmetry in the angular distributions of $t\bar{t}$ events is a powerful test of the standard model (SM) predictions and allows to search for new effects beyond the SM. Perturbative quantum chromodynamics (pQCD) at leading order predicts that angular distributions of the t and $\bar{t}$ quarks produced in $q\bar{q}$ annihilation is forward-backward (FB) symmetric in the center of mass frame. However, a FB asymmetry appears at order α_S^3, as a result of interference of production diagrams. At this order, interference of the Born and box diagrams results in a positive asymmetry in two-body production, while a negative contribution to the asymmetry arises from the interference of the diagrams with initial and final state radiation (ISR/FSR) [122–128]. As a result, a positive FB asymmetry is expected, such that the top (antitop) quark is preferentially emitted in the direction of the incoming quark (antiquark). Interactions beyond the SM can modify the $t\bar{t}$ production asymmetry, for example through contributions from axigluons or diquarks [129–141], Z'/W' bosons [142–150], supersymmetry [151–153], or new scalar particles [154, 155].

At the Tevatron, the $t\bar{t}$ pairs are produced in $p\bar{p}$ collisions, so we can define the forward-backward asymmetry as

$$A_{t\bar{t}} = \frac{N(\Delta y > 0) - N(\Delta y < 0)}{N(\Delta y > 0) + N(\Delta y < 0)}, \tag{2.18}$$

where $\Delta y = y_t - y_{\bar{t}}$ is the difference in rapidity of top and antitop quarks, $N(...)$ is the corresponding number of $t\bar{t}$ events.

The results of the first measurements of the $t\bar{t}$ asymmetry at the Tevatron were rather high, compared to the theoretical NLO prediction and values predicted by the MC generator MC@NLO. For example, in [156] the D0 collaboration measured the $t\bar{t}$ asymmetry to be $19.6 \pm 6.5\%$ and CDF experiment measured it to be $15.0 \pm 5.5\%$ [157], while MC@NLO generator predicts a value of about $5.0 \pm 0.1\%$ [156]. The pQCD calculations which account for the electroweak corrections predict this asymmetry to be $8.7^{+0.6}_{-0.5}\%$ at the Tevatron [122]. The observed tension between measurements and theoretical expectations generated a lot of interest in the community and stayed, for many years, the most intriguing measurement in top quark physics.

The analysis of experimental data includes several steps. After event selection the top and antitop quark kinematic parameters need to be reconstructed using measured parameters of leptons, jets and missing transverse energy. Two final states are usually considered for the asymmetry measurement: ℓ+jets and $\ell\ell$. Usually, more or less sophisticated kinematic reconstruction methods are used to account for the ambiguity in attributing jets to partons. In the dilepton final state, the $t\bar{t}$ pair decays to a final state with two non-detected neutrinos, $t\bar{t} \to W^+W^-\ b\bar{b} \to \ell^+\ell^-\ \nu\bar{\nu}\ b\bar{b}$ and the reconstruction in this final state requires a "scan" of the phase space constrained by the experimental measured parameters of leptons and jets. The last step in the asymmetry measurements is a unfolding of the reconstructed distributions to the parton level. Strictly speaking, such unfolding is not required if we restrict the measurement to the inclusive asymmetry only. In the case of the ℓ+jets final state, we are interested in measuring the asymmetry dependence from the invariant mass of $t\bar{t}$ pair ($m_{t\bar{t}}$), Δy. Such a differential measurement is more sensitive to possible new physics contributions, because of the phase space enhancement of such a contribution, e.g. at high $m_{t\bar{t}}$.

The procedure of reconstruction and unfolding complicates a lot the asymmetry analyses and requires a careful calibration. An alternative approach has been developed for the

asymmetry measurements. Instead of measuring the quark asymmetry, we can measure an asymmetry in the distributions of leptons. Since the direction of leptons is measured with a good precision, no unfolding is needed. The drawback of this approach is that the leptonic asymmetry isn't as powerful as the top quark asymmetry, because the direction of leptons is not fully correlated with the direction of top quark. For example, at the Tevatron, the single-lepton asymmetry is defined as

$$A_\ell = \frac{N(q \times \eta > 0) - N(q \times \eta < 0)}{N(q \times \eta > 0) + N(q \times \eta < 0)} \tag{2.19}$$

where η and q are the lepton rapidity and charge. The dilepton asymmetry in the $\ell\ell$ final state is defined as

$$A_{\ell\ell} = \frac{N(\Delta\eta > 0) - N(\Delta\eta < 0)}{N(\Delta\eta > 0) + N(\Delta\eta < 0)} \tag{2.20}$$

where $\Delta\eta$ is the difference in leptons rapidities $\Delta\eta = \eta_{\ell^+} - \eta_{\ell^-}$. The NLO prediction for those asymmetries are $A_\ell = 3.8 \pm 0.6\%$ and $A_{\ell\ell} = 4.8 \pm 0.4\%$ [122]. In fact, the measurement of the leptonic asymmetry is complementary to the $t\bar{t}$ asymmetry measurement, because the angular distribution of leptons is influenced not only by the angular distribution but also by polarization of the top quark. In the SM the top quark polarization in $t\bar{t}$ production is close to zero, but could be significantly different for parity violating non-SM contributions, e.g. in the $t\bar{t}$ production via axigluon mechanism [158].

2.6.2 Asymmetry Measurement in Distributions of Leptons in the Dilepton Final State

For the asymmetry measurements in the dilepton final state [43], we used the selection described in section 2.2 with the additional acceptance cuts $|\eta| < 2$, $|\Delta\eta| < 2.4$ to optimize the statistical uncertainty of the asymmetry measurement. The $q \times \eta$ and $\Delta\eta$ distributions for dilepton events after selection are shown in Fig. 2.18. We compute A_ℓ and $A_{\ell\ell}$ in two steps. First, we perform a bin-by-bin subtraction of the estimated background contributions to the data and apply a bin-by-bin correction, to account for the efficiency of reconstruction and selection. The correction function is determined using $t\bar{t}$ MC@NLO events at the parton level within the fiducial region $|\eta| < 2$, $|\Delta\eta| < 2.4$[8]. and events after reconstruction and selection. The $q \times \eta$ and $\Delta\eta$ distributions after correction for selection efficiency are shown in Fig. 2.19. The cross section in each bin is calculated as a weighted sum of the measurements in all channels, where only the statistical uncertainty is taken into account. At the second step, we extrapolate the corrected asymmetries to the full range of η by multiplying the corrected asymmetries with the calculated extrapolation factor, which is given by the ratio of the generator level SM $t\bar{t}$ asymmetries from MC@NLO without selections to asymmetries within the fiducial region ($|\eta| < 2$ and $|\Delta\eta| < 2.4$). We refer to these asymmetries as "extrapolated" asymmetries.

Systematic effects can affect the measurements in different ways: affect the efficiency corrections and thereby modify the corrected and extrapolated asymmetries, affect the normalization or the differential dependence, i.e., shape of the background distributions, finally, differences in MC generations or model assumptions could impact the extrapolation correction to the full phase space. For the last item, we verified that the axigluon MC samples do not affect the extrapolated correction significantly. For the first two items, we consider the following sources of systematic uncertainties: uncertainties on the efficiencies

[8] Here η refers to the generated lepton pseudorapidity

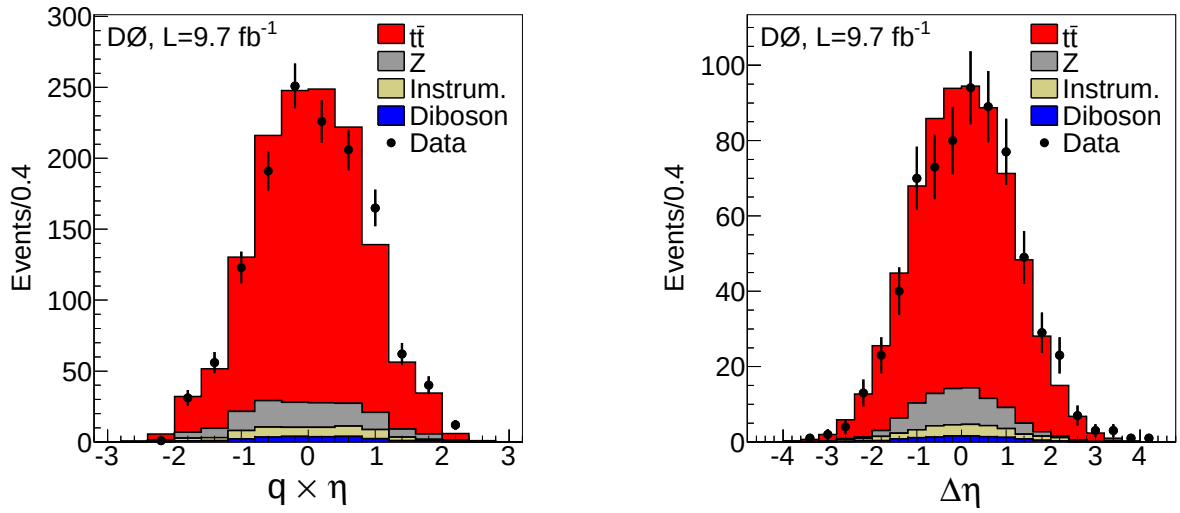

Figure 2.18: Distributions in $q \times \eta$ and $\Delta\eta = \eta_{\ell^+} - \eta_{\ell^-}$ for the sum of ee, $e\mu$ and $\mu\mu$ events, 9.7 fb^{-1}, [43].

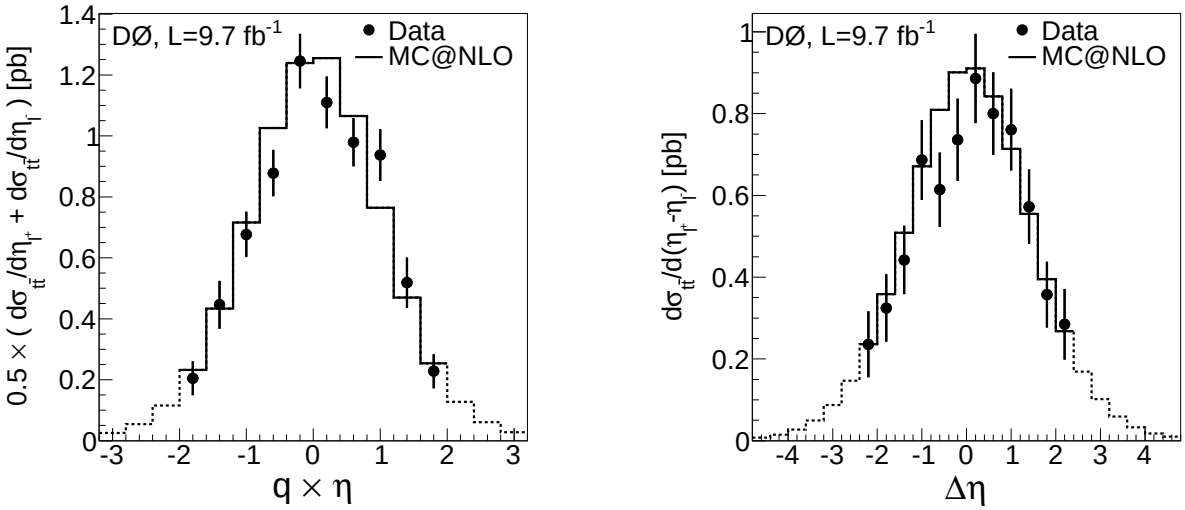

Figure 2.19: Distributions in $q \times \eta$ and $\Delta\eta$ in the dilepton final state, after subtraction of background and correction for selection efficiency within the acceptance. The dashed lines show the predictions from MC@NLO outside the analysis acceptance, 9.7 fb^{-1}, [43].

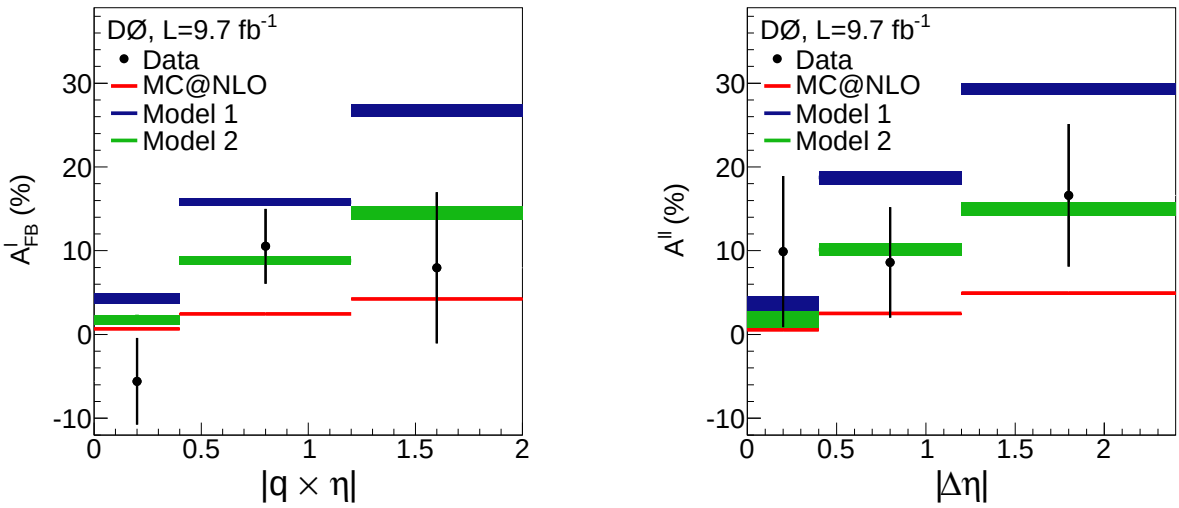

Figure 2.20: Asymmetry distributions in $|q \times \eta|$ and $|\Delta\eta|$, in the dilepton final state, after background subtraction and after corrections for selection efficiency. Data is compared with expectations from MC@NLO and axigluon models, 9.7 fb^{-1}, [43]

	A_ℓ, %	$A_{\ell\ell}$, %
Measured, $\|\eta\| < 2$ and $\|\Delta\eta\| < 2.4$	$4.1 \pm 3.5 \pm 1.0$	$10.5 \pm 4.7 \pm 1.1$
Extrapolated to the full phase space	$4.4 \pm 3.7 \pm 1.1$	$12.3 \pm 5.4 \pm 1.5$
SM, NLO	3.8 ± 0.3	4.8 ± 0.4

Table 2.10: The measured corrected and extrapolated asymmetries in lepton distribution. compared to the predicted SM NLO asymmetries [122] for inclusive $t\bar{t}$ production, 9.7 fb^{-1}, [43].

	$g_{R,i}$	$g_{L,i}$	$g_{R,q}$	$g_{L,q}$	$g_{R,t}$	$g_{L,t}$	m_G(GeV)	Γ_G(GeV)	$A_{t\bar{t}}$, %	$A_{\ell\ell}$, %	A_ℓ, %
Model 1	$0.8\,g_s$	0					200	50	11.2 ± 0.6	21.3 ± 0.6	14.9 ± 1.0
Model 2			$-1.5\,g_s$	0	$6\,g_s$	0	2000	670	7.4 ± 0.5	11.3 ± 0.5	8.9 ± 0.8

Table 2.11: Description of two axigluon models, where g_s is the QCD coupling, $g_{R,i}$ and $g_{L,i}$ represent flavor universal couplings to the SM quarks with right-handed (R), left-handed (L) couplings respectively. $g_{R,q}$, $g_{L,q}$, $g_{R,t}$ and $g_{L,t}$ represent couplings to light (q) and top (t) quarks respectively. m_G, Γ_G are the axigluon mass and width.

of lepton identification, uncertainties on trigger efficiencies, uncertainties on jet-related quantities (JES, efficiencies, b-quark tagging, etc). Uncertainties specific to the background model include uncertainties on the asymmetries generated for Z boson events and on background normalization. Another important uncertainty is related to the choice of parton showering and hadronization in $t\bar{t}$ events. This is evaluated by taking the difference between the asymmetries obtained with efficiency corrections and extrapolation factors using MC@NLO+HERWIG and ALPGEN+PYTHIA. This estimation also includes the difference in the simulation of NLO effects between MC@NLO and ALPGEN generators. Finally, we consider the limited statistics of the MC samples used to measure the efficiency correction. We estimate the total systematic uncertainty to be 1.0% (1.1%) on the corrected $A_\ell(A_{\ell\ell})$ asymmetries and 1.1% (1.5%) on the extrapolated ones.

The measured asymmetry is a combination of the asymmetries in the ee, $e\mu$ 2 jets, $e\mu$ 1 jet, and $\mu\mu$ final states. We combine these measurements using the BLUE method [105, 106], assuming 100% correlation among their systematic uncertainties. Table 2.10 summarizes the corrected and extrapolated asymmetries, as well as the prediction from a SM NLO calculation including QCD and electroweak (EW) corrections [122]. In addition, we studied the dependence of the corrected asymmetries as a function of $q \times \eta$ and $\Delta\eta$ in Fig. 2.20, where we observe no significant dependence on these variables in data and consistently with the MC@NLO [98, 159] predictions. For illustration, we compare the measured dependence with two selected axigluon models. The details of these models are given in Table 2.11 and in [158].

We also studied the statistical correlation between A_ℓ and $A_{\ell\ell}$, using ensembles of generated pseudo-data and found the correlation between the two asymmetries to be 0.82. Using this correlation coefficient, we can compute the ratio of the two extrapolated asymmetries in data to be $R = A_\ell/A_{\ell\ell} = 0.36 \pm 0.20$, consistent at the level of 2 standard deviations (SD) with the SM prediction of 0.79 ± 0.10. The uncertainty on the theoretical ratio is estimated by adding in quadrature the uncertainty on the theoretical expectations for A_ℓ and $A_{\ell\ell}$ and without taking into account the possible correlation between these two values. Fig. 2.21 shows the A_ℓ versus $A_{\ell\ell}$ 2D asymmetry measurement.

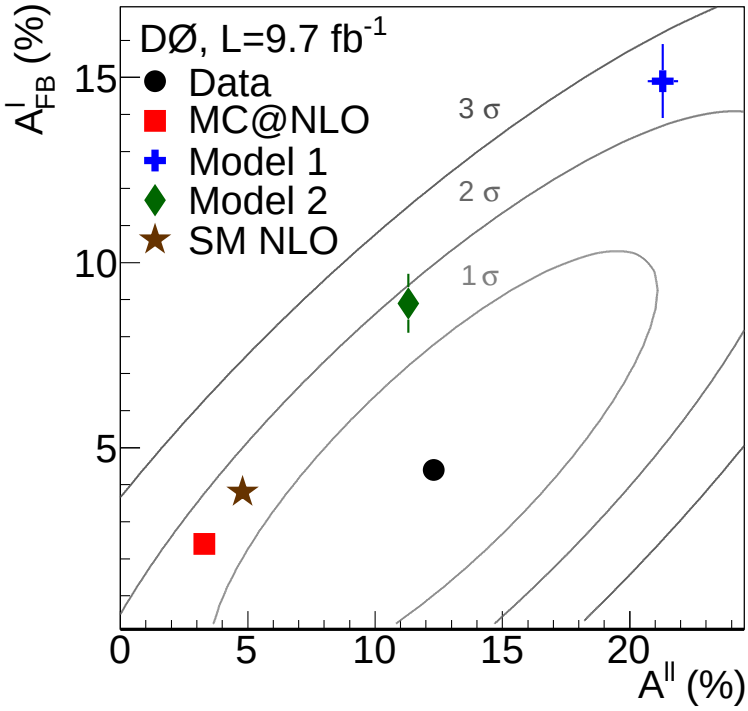

Figure 2.21: A_ℓ vs $A_{\ell\ell}$ asymmetry as measured in the dilepton final state [43]. The ellipses represent 1, 2, and 3 SD contours where both, statistical and systematical uncertainties are taken into account.

2.6.3 $t\bar{t}$ Asymmetry Measurement in Dilepton Final State

To measure the $A_{t\bar{t}}$ asymmetry in the dilepton final state [80], we use the selection described in section 2.2 and all events are required to have at least two jets. To reconstruct the top quark and antiquark rapidities, y_t, $y_{\bar{t}}$, we are using the ME technique, as it is discussed in section 2.4. Using this technique, we reconstruct the probability density function $f_i(\Delta y)$ for the variable $\Delta y = y_t - y_{\bar{t}}$ for each event i and not the single value for the rapidity difference. Function $f_i(\Delta y)$ is normalized to unity: $\int_{-\infty}^{+\infty} f_i(\Delta y) d(\Delta y) = 1$. The sum of these functions for all events, $f(\Delta y) = \sum_i^N f_i(\Delta y)$, forms the reconstructed distribution, see Fig. 2.22. The reconstructed asymmetry is calculated as:

$$A_{raw}^{t\bar{t}} = \frac{1}{N}\left(\int_0^{+\infty} f(\Delta y) d(\Delta y) - \int_{-\infty}^{0} f(\Delta y) d(\Delta y)\right), \tag{2.21}$$

where N is the number of selected events. For convenience, for each event i we introduce the variable A_i, defined as

$$A_i = \int_0^{+\infty} f_i(\Delta y) d(\Delta y) - \int_{-\infty}^{0} f_i(\Delta y) d(\Delta y), \text{ and} \tag{2.22}$$

$$A_{raw}^{t\bar{t}} = \frac{1}{N}\sum_i^N A_i \tag{2.23}$$

Fig. 2.23 shows the reconstructed Δy distribution after subtraction of the background and the corresponding distribution of the A_i variable. By definition the variable A_i is limited to the range [-1,+1].

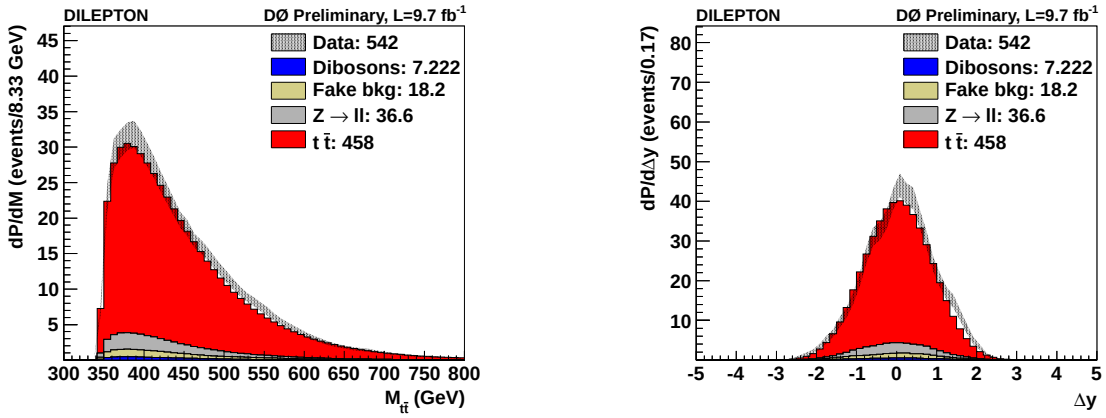

(a) $t\bar{t}$ invariant mass.

(b) Rapidity difference between the top quark and antiquark.

Figure 2.22: Comparison of reconstructed distributions between data (band) and expectations (filled areas), 9.7 fb^{-1}, [80]. The statistical uncertainty on data is represented by an uncertainty band, because data in adjacent bins are correlated due to the reconstruction procedure.

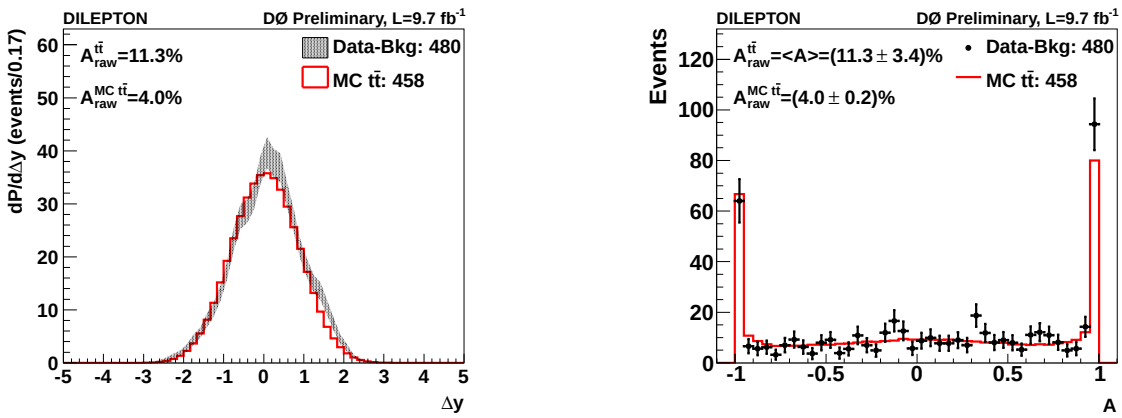

Figure 2.23: Distributions of the Δy and A_i variables after background subtraction, 9.7 fb^{-1}, [80].

The statistical precision of this measurement is limited by the number of events in the $\ell\ell$ final state. That is why we decided to focus our efforts on the measurement of the inclusive asymmetry only. In this case, we can correct the reconstructed asymmetry $A^{t\bar{t}}_{raw}$ with a simple calibration and no unfolding is needed. We produced samples with different asymmetries by reweighting the MC@NLO MC sample. The measured dependence of the reconstructed asymmetry, $A^{t\bar{t}}_{raw}$, versus the generated asymmetry, A^{MCtrue}_{FB}, is parametrized with a linear function, Fig. 2.24. Using this parametrization we correct the raw asymmetry for reconstruction effects:

$$A_{t\bar{t}} = \left(A^{t\bar{t}}_{raw} - 0.011\right)/0.565 \ . \tag{2.24}$$

To estimate the systematic uncertainty, we consider the sources of uncertainties similar to the ones described in section 2.6.2. The main contribution is coming from the signal modeling and uncertainty in calibration due to the MC reweighting procedure. It was found that the measurement result is sensitive to the polarization of the top quark. If we assume zero polarization, as in the SM, we obtain an asymmetry of [80].:

$$A_{t\bar{t}} = 0.180 \pm 0.061 \ (\mathrm{stat}) \ \pm 0.032 \ (\mathrm{syst}) \ \ . \tag{2.25}$$

If we allow for non-zero polarization, we estimate an additional model depent uncertainty of about 5 % using the axigluon MC samples with different asymmetries and polarizations [158].

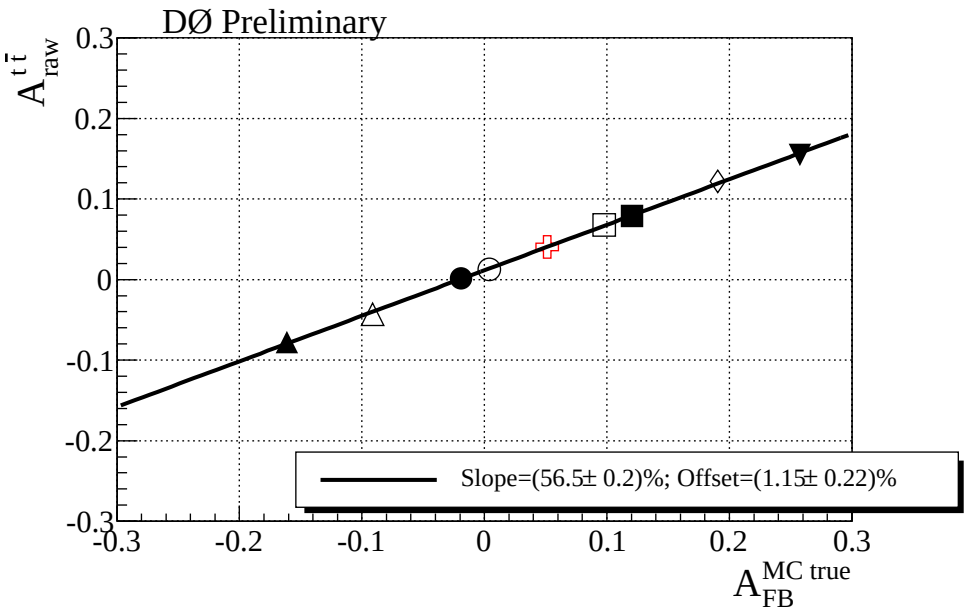

Figure 2.24: Reconstructed asymmetry as a function of the generated asymmetry, 9.7 fb^{-1}, [80]. The different markers correspond to the different pseudo-samples (the red marker corresponds to the non-reweighted MC@NLO sample). The black line shows the parametrization used for the measurement calibration.

2.6.4 Overview and discussion

For quite some time, measurements at the Tevatron were puzzling because of the observed deviation (2–3 SD) between the measured and expected $A_{t\bar{t}}$ inclusive asymmetries. In the most recent and the most precise measurements of the CDF and D0 experiments (Table 2.12, Fig. 2.25) this difference is reduced below 2 SD. Additional interest in these measurements is caused by the observed deviation in the dependence of the $A_{t\bar{t}}$ on the invariant mass of the $t\bar{t}$ pair. In particular, CDF measured a slope of the asymmetry to be different by a 2.4 SD deviation from the expectation [160]. A similar effect is observed for the dependence of the $A_{t\bar{t}}$ on the $|\Delta y|$ distribution, where a deviation of about 2.8 SD is observed. Unfortunately, the recent D0 measurement, [161], doesn't confirm these tensions, Fig. 2.26. In addition, a very recent NNLO differential cross-section calculation, increases the SM expectation by 0.7% [162], and makes the agreement between experimental and theoretical numbers even better. The combination of measurements between the two Tevatron experiments is ongoing and will allow to make a quantitative statement about the level of agreement between experimental and theoretical results.

The leptonic asymmetries A_ℓ, $A_{\ell\ell}$ are measured by both Tevatron experiments with full available statistics and show rather good agreement with the expectation, even if the CDF measurements of the A_ℓ asymmetry differ from the SM expectation by about 2 SD, Table 2.12. There exists some difficulty in the interpretation of the obtained results. It is related to the fact that leptonic asymmetries are measured in the phase space limited by the acceptance and then extrapolated to the full phase space. These acceptance cuts

are different in different measurements, e.g. CDF ℓ+jets measurement uses $|y| < 1.25$, D0 ℓ+jets measurement uses $|y| < 1.5$ and the asymmetry in the D0 dilepton channel is measured within the acceptance of $|y| < 2.0$. The extrapolation procedure is model dependent and done in a different way in the different measurements. Currently both experiments are working on the combination of measurements and defining the most appropriate extrapolation procedure.

At the LHC, the pp collisions are forward-backward symmetric, so no forward-backward asymmetry can be observed. It is possible to define a quantity similar to the forward-backward asymmetry at the Tevatron, called charge asymmetry, by:

$$A_C = \frac{N(\Delta|y| > 0) - N(\Delta|y| < 0)}{N(\Delta|y| > 0) + N(\Delta|y| < 0)} \tag{2.26}$$

where $\Delta|y| = |y_t| - |y_{\bar{t}}|$ is the difference in absolute rapidity of top and antitop quarks. Because $t\bar{t}$ events at the LHC are produced mainly by the gluon fusion process, but the asymmetry is caused by the $q\bar{q}$ annihilation, the total asymmetry at the LHC is small. The latest SM calculations for this quantity yield $(1.23 \pm 0.05)\%$ for the LHC 7 TeV and $(1.11 \pm 0.05)\%$ for the LHC 8 TeV [122]. Measurements at the LHC don't show any deviation from the SM prediction, [163], but the expected asymmetry is very low and the current precision of the measurements which is about 1%, is at the level of the expected asymmetry. At the LHC the most interesting direction of study is a measurement of the differential asymmetry as a function of the velocity or invariant $t\bar{t}$ mass [164]. The large statistics accumulated at the LHC makes possible the precise measurements in regions of the phase space where both SM and non-SM asymmetries are expected to be large. Up to now, no deviation from the expectations were found [165, 166].

In conclusion, we can say that a lot of effort has been made, both from the experimental and theoretical sides, to understand the earlier obtained difference between the measurements and SM expectation. Unfortunately, improvements in the experimental precision and in the theoretical prediction don't leave much space for a contribution from new physics, even if slightly higher values of the asymmetry are measured at the Tevatron compared to the SM prediction. For example, the naive average[9] of the four $A_{t\bar{t}}$ measurements from Table 2.12 gives a result of $13.6 \pm 2.3\%$ as compared to NNLO+EW expectation of $9.5 \pm 0.7\%$ [162].

[9]For this average we assume that both statistic and systematic uncertainties are not correlated between measurements.

Source	Year	Asymmetry in %		
		$A_{t\bar{t}}$	A_ℓ	$A_{\ell\ell}$
SM, NNLO + EW, [162]	2014	9.5 ± 0.7		
SM, NLO + EW, [122]	2012	8.8 ± 0.6	3.8 ± 0.3	4.8 ± 0.4
CDF ℓ+jets, 9.4 fb^{-1}	2012, 2013	16.4 ± 4.7 [160]	9.4 ± 3.0 [167]	
CDF $\ell\ell$, 5.1/9.1 fb^{-1}	2011, 2013	42 ± 16 [168]*	7.2 ± 6.0 [169]	7.6 ± 8.2 [169]
D0 ℓ+jets, 9.7 fb^{-1}	2014	10.6 ± 3.0 [161]	5.0 ± 3.6 [170]	
D0 $\ell\ell$, 9.7 fb^{-1},	2013, 2014	18.0 ± 6.9 [80]*	4.4 ± 3.9 [43]	12.3 ± 5.6 [43]

Table 2.12: The most recent measurements of the forward-backward asymmetry at the Tevatron and comparison with the SM expectations. Measurements marked with * are preliminary results, reported in a conference note only.

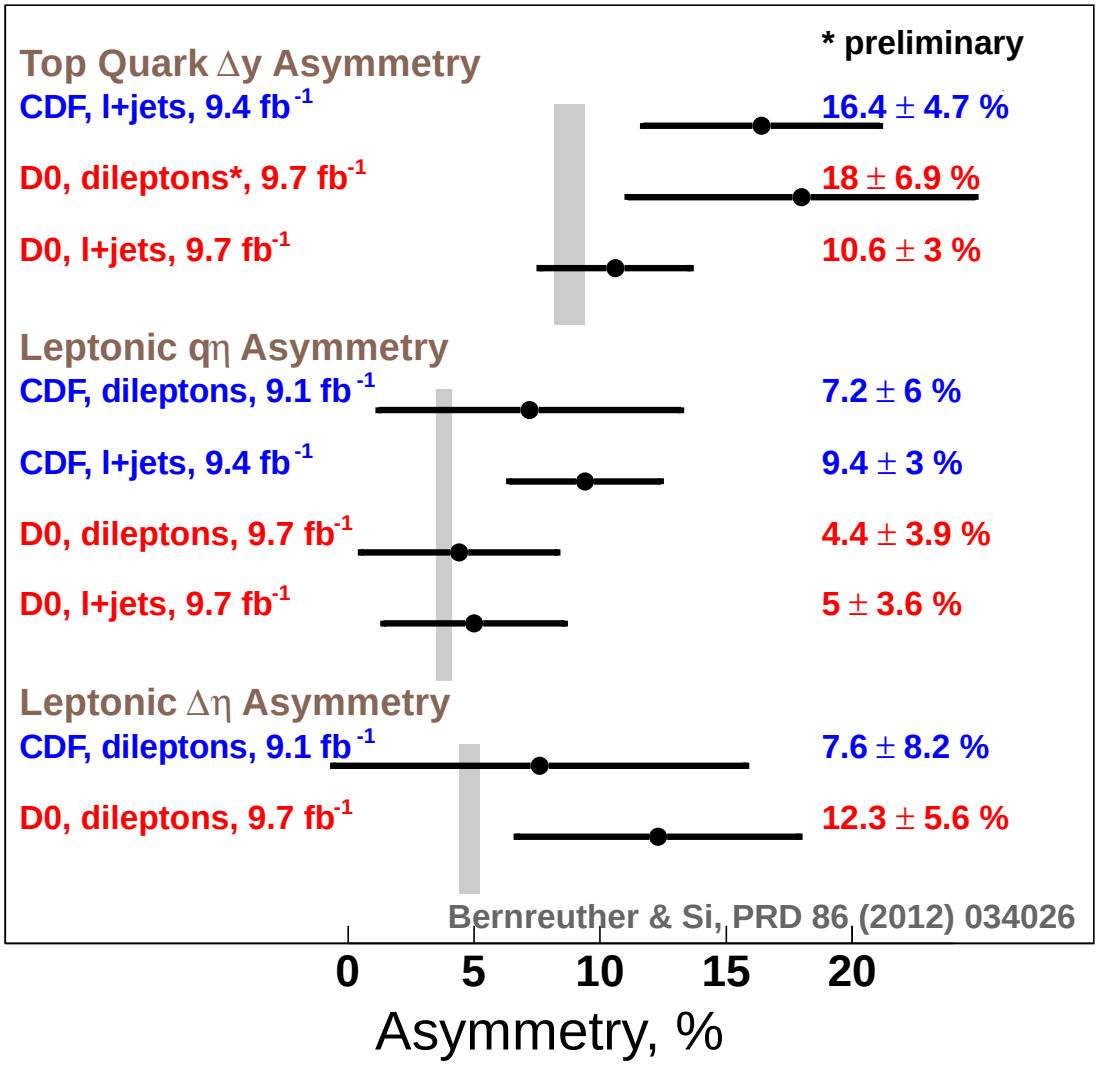

Figure 2.25: The most recent asymmetry measurements at the Tevatron and comparison to the theoretical prediction [122].

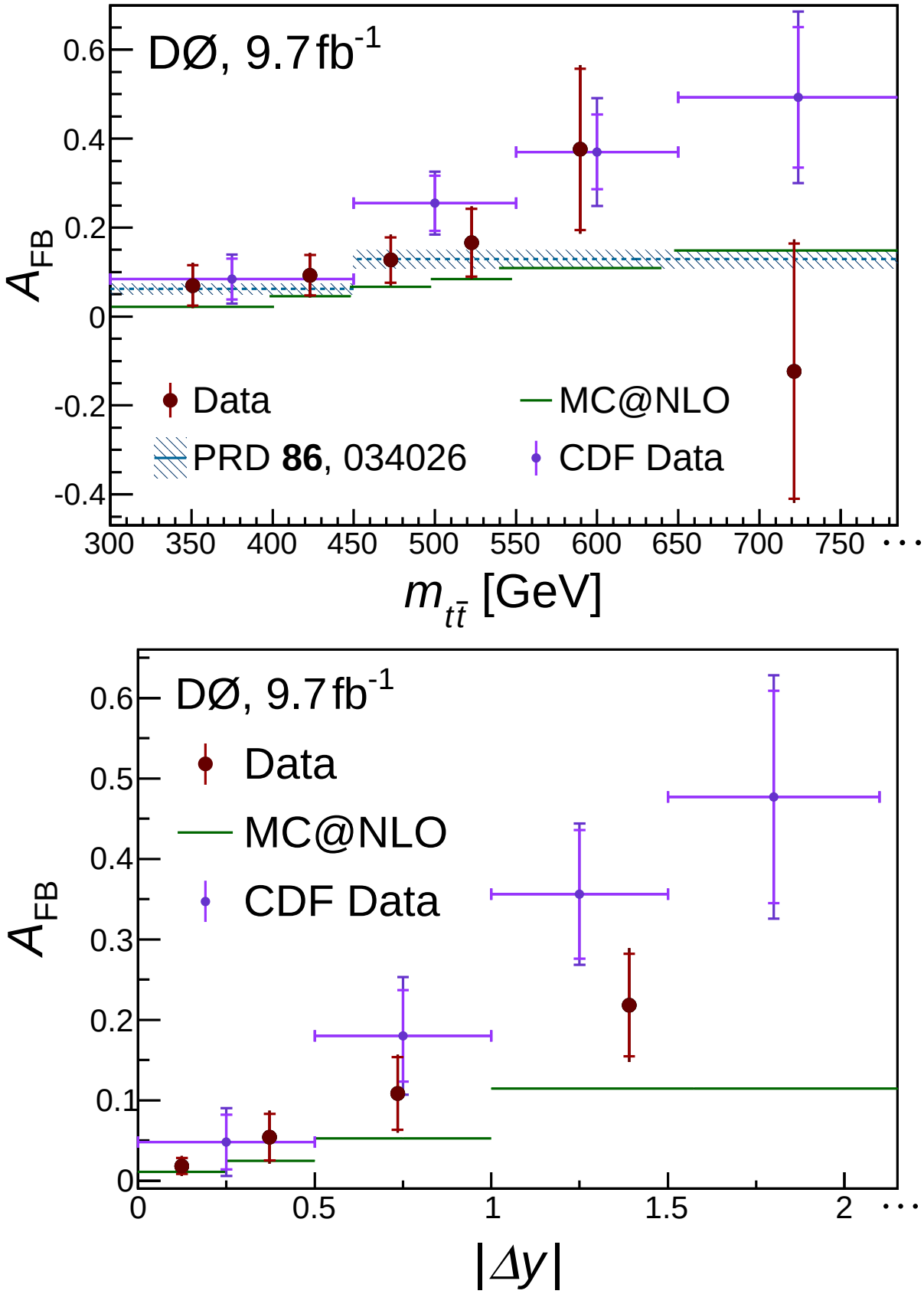

Figure 2.26: $A_{t\bar{t}}$ asymmetry distribution as a function of $m_{t\bar{t}}$ and $|\Delta y|$ as measured by the D0 and CDF experiments in the ℓ+jets final state [160, 161].

Bibliography

[1]K. Olive et al., "Review of Particle Physics", Chin.Phys. **C38**, 090001 (2014).

[2]CDF and D0 collaborations, "Combination of CDF and D0 results on the mass of the top quark using up to 9.7 fb^{-1} at the Tevatron", (2014), arXiv:`1407.2682 [hep-ex]`.

[3]S. Abachi et al., "Observation of the top quark", Phys. Rev. Lett. **74**, 2632–2637 (1995), arXiv:`hep-ex/9503003 [hep-ex]`.

[4]F. Abe et al., "Observation of top quark production in $\bar{p}p$ collisions", Phys. Rev. Lett. **74**, 2626–2631 (1995), arXiv:`hep-ex/9503002 [hep-ex]`.

[5]M. Kobayashi and T. Maskawa, "CP Violation in the Renormalizable Theory of Weak Interaction", Prog.Theor.Phys. **49**, 652–657 (1973).

[6]M. L. Perl, G. Abrams, A. Boyarski, M. Breidenbach, D. Briggs, et al., "Evidence for Anomalous Lepton Production in e+ - e- Annihilation", Phys. Rev. Lett. **35**, 1489–1492 (1975).

[7]S. Herb, D. Hom, L. Lederman, J. Sens, H. Snyder, et al., "Observation of a Dimuon Resonance at 9.5-GeV in 400-GeV Proton-Nucleus Collisions", Phys. Rev. Lett. **39**, 252–255 (1977).

[8]H. Behrend et al., "Search for New Heavy Quarks in e^+e^- Collisions Up to 46.78-GeV Center-of-mass Energy", Phys.Lett. **B144**, 297 (1984).

[9]B. Adeva et al., "Study of Hadron and Inclusive Muon Production From Electron Positron Annihilation at 39.79-GeV $\leq \sqrt{s} \leq$ 46.78-GeV", Phys. Rev. **D34**, 681–691 (1986).

[10]K. Abe et al., "Measurement of R and Search for New Quark Flavors Decaying Into Multi - Jet Final States in e^+e^- Collisions Between 54-GeV and 61.4-GeV c.m. Energies", Phys.Lett. **B234**, 382 (1990).

[11]G. Abrams, C. Adolphsen, D. Averill, J. Ballam, B. C. Barish, et al., "Searches for New Quarks and Leptons Produced in Z Boson Decay", Phys. Rev. Lett. **63**, 2447 (1989).

[12]D. Decamp et al., "A Search for New Quarks and Leptons From Z^0 Decay", Phys.Lett. **B236**, 511 (1990).

[13]P. Abreu et al., "Search for the T and b′ Quarks in Hadronic Decays of the Z^0 Boson", Phys.Lett. **B242**, 536–546 (1990).

[14]M. Akrawy et al., "A Search for the Top and b' Quarks in Hadronic Z^0 Decays", Phys.Lett. **B236**, 364 (1990).

[15]C. Albajar et al., "Search for new heavy quarks in proton - antiproton collisions at $\sqrt{s}$ = 0.63 TeV", Z.Phys. **C48**, 1–12 (1990).

[16]T. Akesson et al., "Search for Top Quark Production at the CERN $\bar{p}p$ Collider", Z.Phys. **C46**, 179 (1990).

[17]S. Willenbrock, "The Standard model and the top quark", (2002), arXiv:hep-ph/0211067 [hep-ph].

[18]M. E. Peskin and D. V. Schroeder, *An Introduction to quantum field theory* (Westview Press, 1995).

[19]V. Miransky, M. Tanabashi, and K. Yamawaki, "Dynamical Electroweak Symmetry Breaking with Large Anomalous Dimension and t Quark Condensate", Phys.Lett. **B221**, 177 (1989).

[20]V. Miransky, M. Tanabashi, and K. Yamawaki, "Is the t Quark Responsible for the Mass of W and Z Bosons?", Mod.Phys.Lett. **A4**, 1043 (1989).

[21]W. A. Bardeen, C. T. Hill, and M. Lindner, "Minimal Dynamical Symmetry Breaking of the Standard Model", Phys. Rev. **D41**, 1647 (1990).

[22]H. S. Fukano and S. Matsuzaki, "Top-Mode Pseudos at the LHC", (2014), arXiv:1401.6292 [hep-ph].

[23]M. Jezabek and J. H. Kuhn, "Semileptonic Decays of Top Quarks", Phys.Lett. **B207**, 91 (1988).

[24]M. Jezabek and J. H. Kuhn, "QCD Corrections to Semileptonic Decays of Heavy Quarks", Nucl. Phys. **B314**, 1 (1989).

[25]W. Bernreuther, A. Brandenburg, Z. G. Si, and P. Uwer, "Top quark pair production and decay at hadron colliders", Nucl. Phys. **B690**, 81–137 (2004), arXiv:hep-ph/0403035.

[26]M. Czakon, M. L. Mangano, A. Mitov, and J. Rojo, "Constraints on the gluon PDF from top quark pair production at hadron colliders", JHEP **1307**, 167 (2013), arXiv:1303.7215 [hep-ph].

[27]V. M. Abazov et al., "Electron and Photon Identification in the D0 Experiment", Nucl. Instrum. Meth. **A750**, 78–95 (2014), arXiv:1401.0029 [hep-ex].

[28]V. M. Abazov et al., "Muon reconstruction and identification with the Run II D0 detector", Nucl. Instrum. Meth. **A737**, 281–294 (2014), arXiv:1307.5202 [hep-ex].

[29]G. C. Blazey, J. R. Dittmann, S. D. Ellis, V. D. Elvira, K. Frame, et al., "Run II jet physics", 47–77 (2000), arXiv:hep-ex/0005012 [hep-ex].

[30]V. M. Abazov et al., "Jet energy scale determination in the D0 experiment", Nucl. Instrum. Meth. **A763**, 442 –475 (2014), arXiv:1312.6873 [hep-ex].

[31]V. Abazov et al., "b-Jet Identification in the D0 Experiment", Nucl. Instrum. Meth. **A620**, 490–517 (2010), arXiv:1002.4224 [hep-ex].

[32]V. M. Abazov et al., "Improved b quark jet identification at the D0 experiment", Nucl. Instrum. Meth. **A763**, 290 –303 (2014), arXiv:1312.7623 [hep-ex].

[33]M. L. Mangano, M. Moretti, F. Piccinini, R. Pittau, and A. D. Polosa, "ALPGEN, a generator for hard multiparton processes in hadronic collisions", JHEP **07**, 001 (2003), arXiv:hep-ph/0206293.

[34]T. Sjostrand, S. Mrenna, and P. Z. Skands, "PYTHIA 6.4 Physics and Manual", JHEP **0605**, 026 (2006), arXiv:hep-ph/0603175 [hep-ph].

[35]T. Affolder et al., "Charged jet evolution and the underlying event in $p\bar{p}$ collisions at 1.8 TeV", Phys. Rev. **D65**, 092002 (2002).

[36]P. M. Nadolsky, H.-L. Lai, Q.-H. Cao, J. Huston, J. Pumplin, et al., "Implications of CTEQ global analysis for collider observables", Phys. Rev. **D78**, 013004 (2008), arXiv:0802.0007 [hep-ph].

[37]R Brun and F. Carminati, "Geant: detector description and simulation tool", CERN Program Library Long Writeup W5013 (1993) (unpublished).

[38]R. Gavin, Y. Li, F. Petriello, and S. Quackenbush, "FEWZ 2.0: A code for hadronic Z production at next-to-next-to-leading order", Comput.Phys.Commun. **182**, 2388–2403 (2011), arXiv:1011.3540 [hep-ph].

[39]R. K. Ellis, "An update on the next-to-leading order Monte Carlo MCFM", Nucl. Phys. Proc. Suppl. **160**, 170–174 (2006).

[40]V. M. Abazov et al., "Measurement of the normalized $Z/\gamma^* \to \mu^+\mu^-$ transverse momentum distribution in $p\bar{p}$ collisions at $\sqrt{s} = 1.96$ TeV", Phys.Lett. **B693**, 522–530 (2010), arXiv:1006.0618 [hep-ex].

[41]V. Abazov et al., "Experimental discrimination between charge 2e/3 top quark and charge 4e/3 exotic quark production scenarios", Phys. Rev. Lett. **98**, 041801 (2007), arXiv:hep-ex/0608044 [hep-ex].

[42]V. Abazov et al., "Measurement of the $t\bar{t}$ production cross section and top quark mass extraction using dilepton events in $p\bar{p}$ collisions", Phys.Lett. **B679**, 177–185 (2009), arXiv:0901.2137 [hep-ex].

[43]V. M. Abazov et al., "Measurement of the asymmetry in angular distributions of leptons produced in dilepton $t\bar{t}$ final states in $p\bar{p}$ collisions at $\sqrt{s}$=1.96 TeV", Phys.Rev. **D88**, 112002 (2013), arXiv:1308.6690 [hep-ex].

[44]T. Aaltonen et al., "Higgs Boson Studies at the Tevatron", Phys. Rev. **D88**, 052014 (2013), arXiv:1303.6346 [hep-ex].

[45]M. Czakon, P. Fiedler, and A. Mitov, "Total Top-Quark Pair-Production Cross Section at Hadron Colliders Through O(alphaS4)", Phys. Rev. Lett. **110**, 252004 (2013), arXiv:1303.6254 [hep-ph].

[46]V. Ahrens, A. Ferroglia, M. Neubert, B. D. Pecjak, and L. L. Yang, "Renormalization-Group Improved Predictions for Top-Quark Pair Production at Hadron Colliders", JHEP **1009**, 097 (2010), arXiv:1003.5827 [hep-ph].

[47]V. Ahrens, A. Ferroglia, M. Neubert, B. Pecjak, and L. Yang, "Top-Quark Pair Production Beyond Next-to-Leading Order", Nucl. Phys.Proc.Suppl. **205-206**, 48–53 (2010), arXiv:1006.4682 [hep-ph].

[48]S. Moch and P. Uwer, "Theoretical status and prospects for top-quark pair production at hadron colliders", Phys. Rev. **D78**, 034003 (2008), arXiv:arXiv:0804.1476 [hep-ph].

[49]U. Langenfeld, S. Moch, and P. Uwer, "Measuring the running top-quark mass", Phys. Rev. **D80**, 054009 (2009), arXiv:0906.5273 [hep-ph].

[50]N. Kidonakis, "Next-to-next-to-leading soft-gluon corrections for the top quark cross section and transverse momentum distribution", Phys. Rev. **D82**, 114030 (2010), arXiv:1009.4935 [hep-ph].

[51]M. Cacciari, S. Frixione, M. L. Mangano, P. Nason, and G. Ridolfi, "Updated predictions for the total production cross sections of top and of heavier quark pairs at the Tevatron and at the LHC", JHEP **0809**, 127 (2008), arXiv:0804.2800 [hep-ph].

[52]M. Cacciari, S. Frixione, M. Mangano, P. Nason, and G. Ridolfi, "The $t\bar{t}$ cross-section at 1.8-TeV and 1.96-TeV: A Study of the systematics due to parton densities and scale dependence", JHEP **0404**, 068 (2004), arXiv:hep-ph/0303085 [hep-ph].

[53]N. Kidonakis and R. Vogt, "Next-to-next-to-leading order soft gluon corrections in top quark hadroproduction", Phys. Rev. **D68**, 114014 (2003), arXiv:hep-ph/0308222 [hep-ph].

[54]T. A. Aaltonen et al., "Combination of measurements of the top-quark pair production cross section from the Tevatron Collider", Phys. Rev. **D89**, 072001 (2014), arXiv:1309.7570 [hep-ex].

[55]V. M. Abazov et al., "Measurement of the $t\bar{t}$ production cross section using dilepton events in $p\bar{p}$ collisions", Phys.Lett. **B704**, 403–410 (2011), arXiv:1105.5384 [hep-ex].

[56]V. Abazov et al., "Combination of $t\bar{t}$ cross section measurements and constraints on the mass of the top quark and its decays into charged Higgs bosons", Phys. Rev. **D80**, 071102 (2009), arXiv:0903.5525 [hep-ex].

[57]V. Abazov et al., "Measurement of the $t\bar{t}$ production cross-section in $p\bar{p}$ collisions using dilepton events", Phys. Rev. **D76**, 052006 (2007), arXiv:0706.0458 [hep-ex].

[58]N. Cabibbo, "Unitary symmetry and leptonic decays", Phys. Rev. Lett. **10**, 531–533 (1963).

[59]J. Beringer et al., "Review of Particle Physics (RPP)", Phys. Rev. **D86**, 010001 (2012).

[60]J. Alwall, R. Frederix, J.-M. Gerard, A. Giammanco, M. Herquet, et al., "Is $\mathrm{V}(_{tb}) \simeq 1$?", Eur. Phys. J. **C49**, 791–801 (2007), arXiv:hep-ph/0607115 [hep-ph].

[61]V. Abazov et al., "Precision measurement of the ratio $\mathrm{B}(t \to Wb)/\mathrm{B}(t \to Wq)$ and Extraction of V_{tb}", Phys. Rev. Lett. **107**, 121802 (2011), arXiv:1106.5436 [hep-ex].

[62]G. J. Feldman and R. D. Cousins, "A Unified Approach to the Classical Statistical Analysis of Small Signals", Phys. Rev. **D57**, 3873–3889 (1998), arXiv:physics/9711021.

[63]V. M. Abazov et al., "Determination of the pole and MSbar masses of the top quark from the $t\bar{t}$ cross section", Phys.Lett. **B703**, 422–427 (2011), arXiv:1104.2887 [hep-ex].

[64]V. Abazov et al., "A precision measurement of the mass of the top quark", Nature **429**, 638–642 (2004), arXiv:hep-ex/0406031 [hep-ex].

[65]B. Abbott et al., "Direct measurement of the top quark mass at D0", Phys. Rev. **D58**, 052001 (1998), arXiv:hep-ex/9801025 [hep-ex].

[66]V. M. Abazov et al., "Measurement of the top quark mass in $p\bar{p}$ collisions using events with two leptons", Phys. Rev. **D86**, 051103 (2012), arXiv:1201.5172 [hep-ex].

[67]V. M. Abazov et al., "Precise measurement of the top quark mass in the dilepton channel at D0", Phys. Rev. Lett. **107**, 082004 (2011), arXiv:1105.0320 [hep-ex].

[68]V. M. Abazov et al., "Evidence for s-channel single top quark production in $p\bar{p}$ collisions at $\sqrt{s} = 1.96$ TeV", Phys.Lett. **B726**, 656–664 (2013), arXiv:1307.0731 [hep-ex].

[69]V. M. Abazov et al., "Measurement of spin correlation in $t\bar{t}$ production using a matrix element approach", Phys. Rev. Lett. **107**, 032001 (2011), arXiv:1104.5194 [hep-ex].

[70]V. M. Abazov et al., "Evidence for spin correlation in $t\bar{t}$ production", Phys. Rev. Lett. **108**, 032004 (2012), arXiv:1110.4194 [hep-ex].

[71]G. Lepage, "A new algorithm for adaptive multidimensional integration", Journal of Computational Physics **27**, 192–203 (1978).

[72]G. Lepage, *Vegas: an adaptive multi-dimensional integration program*, Cornell preprint CLNS 80-447, (1980)

[73]M. Galassi, J. Davies, J. Theiler, B. Gough, G. Jungman, P. Alken, M. Booth, and F. Rossi, *Gnu scientific library reference manual - third edition*, edited by B. Gough, ISBN 0954612078 (Network Theory Ltd, 2009).

[74]F. Fiedler, A. Grohsjean, P. Haefner, and P. Schieferdecker, "The Matrix Element Method and its Application in Measurements of the Top Quark Mass", Nucl. Instrum. Meth. **A624**, 203–218 (2010), arXiv:1003.1316 [hep-ex].

[75]J. Alwall, A. Freitas, and O. Mattelaer, "The Matrix Element Method and QCD Radiation", Phys. Rev. **D83**, 074010 (2011), arXiv:1010.2263 [hep-ph].

[76]K. Melnikov and M. Schulze, "Top quark spin correlations at the Tevatron and the LHC", Phys.Lett. **B700**, 17–20 (2011), arXiv:1103.2122 [hep-ph].

[77]G. Mahlon and S. J. Parke, "Angular correlations in top quark pair production and decay at hadron colliders", Phys. Rev. **D53**, 4886–4896 (1996), arXiv:hep-ph/9512264 [hep-ph].

[78]G. Mahlon and S. J. Parke, "Maximizing spin correlations in top quark pair production at the Tevatron", Phys.Lett. **B411**, 173–179 (1997), arXiv:hep-ph/9706304 [hep-ph].

[79]V. M. Abazov et al., "Measurement of spin correlation in $t\bar{t}$ production using dilepton final states", Phys.Lett. **B702**, 16–23 (2011), arXiv:1103.1871 [hep-ex].

[80]V Abazov et al., "Measurement of forward-backward asymmetry in $p\bar{p} \to t\bar{t}$ production in the dilepton final states using a matrix element technique", D0 Conference Note 6445 (2014).

[81]A. Hocker, J. Stelzer, F. Tegenfeldt, H. Voss, K. Voss, et al., "TMVA - Toolkit for Multivariate Data Analysis", PoS **ACAT**, 040 (2007), arXiv:physics/0703039 [PHYSICS].

[82]CMS Collaboration, "Search for ttH production using the Matrix Element Method", (2014).

[83]V. M. Abazov et al., "Precision measurement of the top-quark mass in lepton+jets final states", Phys. Rev. Lett. **113**, 032002 (2014), arXiv:1405.1756 [hep-ex].

[84]O. Brandt, G. Gutierrez, M. H. L. S. Wang, and Z. Ye, "Acceleration of matrix element computations for precision measurements", (2014), arXiv:1410.6319 [hep-ex].

[85]P. J. Lujan, "Precision measurement of the top quark mass in the lepton + jets channel using a matrix element method with Quasi-Monte Carlo integration", PhD thesis (2009).

[86]J. M. Campbell, W. T. Giele, and C. Williams, "The Matrix Element Method at Next-to-Leading Order", JHEP **1211**, 043 (2012), arXiv:1204.4424 [hep-ph].

[87]D. Schouten, A. DeAbreu, and B. Stelzer, "Accelerated Matrix Element Method with Parallel Computing", (2014), arXiv:1407.7595 [physics.comp-ph].

[88]C. Quigg, "Top-ology", Phys.Today **50N5**, 20–26 (1997), arXiv:hep-ph/9704332 [hep-ph].

[89]M. Baak et al., "The global electroweak fit at NNLO and prospects for the LHC and ILC", Eur. Phys. J. **C74**, 3046 (2014), arXiv:1407.3792 [hep-ph].

[90]Gfitter Collaboration, *Web page*, http://gfitter.desy.de/Standard_Model/.

[91]M. Awramik, M. Czakon, A. Freitas, and G. Weiglein, "Precise prediction for the W boson mass in the standard model", Phys. Rev. **D69**, 053006 (2004), arXiv:hep-ph/0311148 [hep-ph].

[92]ATLAS Collaboration, CDF Collaboration, CMS Collaboration, D0 Collaboration, "First combination of Tevatron and LHC measurements of the top-quark mass", (2014), arXiv:1403.4427 [hep-ex].

[93]G. Degrassi, S. Di Vita, J. Elias-Miro, J. R. Espinosa, G. F. Giudice, et al., "Higgs mass and vacuum stability in the Standard Model at NNLO", JHEP **1208**, 098 (2012), arXiv:1205.6497 [hep-ph].

[94]D. Buttazzo, G. Degrassi, P. P. Giardino, G. F. Giudice, F. Sala, et al., "Investigating the near-criticality of the Higgs boson", JHEP **1312**, 089 (2013), arXiv:1307.3536 [hep-ph].

[95]V. M. Abazov et al., "Precise measurement of the top-quark mass from lepton+jets events at D0", Phys. Rev. **D84**, 032004 (2011), arXiv:1105.6287 [hep-ex].

[96]V. M. Abazov et al., "Measurement of the top quark mass in final states with two leptons", Phys. Rev. **D80**, 092006 (2009), arXiv:0904.3195 [hep-ex].

[97]V. Abazov et al., "Precise measurement of the top quark mass from lepton+jets events at D0", Phys. Rev. Lett. **101**, 182001 (2008), arXiv:0807.2141 [hep-ex].

[98]S. Frixione and B. R. Webber, "The MC@NLO 3.4 Event Generator", (2008), arXiv:arXiv:0812.0770 [hep-ph].

[99]G. Corcella et al., "HERWIG 6.5: an event generator for Hadron Emission Reactions With Interfering Gluons (including supersymmetric processes)", JHEP **01**, 010 (2001), arXiv:hep-ph/0011363.

[100]B. Cooper, J. Katzy, M. Mangano, A. Messina, L. Mijovic, et al., "Importance of a consistent choice of alpha(s) in the matching of AlpGen and Pythia", Eur. Phys. J. **C72**, 2078 (2012), arXiv:1109.5295 [hep-ph].

[101]A. Banfi, S. Redford, M. Vesterinen, P. Waller, and T. Wyatt, "Optimisation of variables for studying dilepton transverse momentum distributions at hadron colliders", Eur. Phys. J. **C71**, 1600 (2011), arXiv:1009.1580 [hep-ex].

[102]V. M. Abazov et al., "Precise study of the Z/γ^* boson transverse momentum distribution in $p\bar{p}$ collisions using a novel technique", Phys. Rev. Lett. **106**, 122001 (2011), arXiv:1010.0262 [hep-ex].

[103]P. Z. Skands, "Tuning Monte Carlo Generators: The Perugia Tunes", Phys. Rev. **D82**, For the description of Perugia 2011 tunes, see arxive version., 074018 (2010), arXiv:1005.3457 [hep-ph].

[104]S. Schael et al., "Precision electroweak measurements on the Z resonance", Phys.Rept. **427**, 257–454 (2006), arXiv:hep-ex/0509008 [hep-ex].

[105]L. Lyons, D. Gibaut, and P. Clifford, "HOW TO COMBINE CORRELATED ESTIMATES OF A SINGLE PHYSICAL QUANTITY", Nucl. Instrum. Meth. **A270**, 110 (1988).

[106]A. Valassi, "Combining correlated measurements of several different physical quantities", Nucl. Instrum. Meth. **A500**, 391–405 (2003).

[107]T. Aaltonen et al., "Combination of the top-quark mass measurements from the Tevatron collider", Phys. Rev. **D86**, 092003 (2012), arXiv:1207.1069 [hep-ex].

[108]CMS Collaboration, "Measurement of the top-quark mass in $t\bar{t}$ events with lepton+jets final states in pp collisions at sqrt(s)=8 TeV", CMS note, CMS-PAS-TOP-14-001 (2014).

[109]T. Aaltonen et al., "Precision top-quark mass measurement at cdf", Phys. Rev. Lett. **109**, 152003 (2012).

[110]ATLAS Collaboration, "Measurement of the Top Quark Mass from $\sqrt{s} = 7$ TeV ATLAS Data using a 3-dimensional Template Fit", (2013).

[111]M. C. Smith and S. S. Willenbrock, "Top quark pole mass", Phys. Rev. Lett. **79**, 3825–3828 (1997), arXiv:`hep-ph/9612329 [hep-ph]`.

[112]A. H. Hoang and I. W. Stewart, "Top Mass Measurements from Jets and the Tevatron Top-Quark Mass", Nucl. Phys.Proc.Suppl. **185**, 220–226 (2008), arXiv:`0808.0222 [hep-ph]`.

[113]S. Moch, S. Weinzierl, S. Alekhin, J. Blumlein, L. de la Cruz, et al., "High precision fundamental constants at the TeV scale", (2014), arXiv:`1405.4781 [hep-ph]`.

[114]V. Abazov et al., "Measurement of the $t\bar{t}$ production cross section in $p\bar{p}$ collisions at $\sqrt{s} = 1.96$-TeV", Phys. Rev. Lett. **100**, 192004 (2008), arXiv:`0803.2779 [hep-ex]`.

[115]G. Aad et al., "Measurement of the $t\bar{t}$ production cross-section using $e\mu$ events with b-tagged jets in pp collisions at $\sqrt{s} = 7$ and 8 TeV with the ATLAS detector", (2014) `10.1140/epjc/s10052-014-3109-7`, arXiv:`1406.5375 [hep-ex]`.

[116]ATLAS collaboration, "Determination of the top-quark pole mass using tt t+1-jet events collected with the ATLAS experiment in 7 TeV pp collisions", ATLAS-CONF-2014-053, ATLAS-COM-CONF-2014-069 (2014).

[117]S. Chatrchyan et al., "Determination of the top-quark pole mass and strong coupling constant from the t t-bar production cross section in pp collisions at $\sqrt{s} = 7$ TeV", Phys.Lett. **B728**, 496–517 (2014), arXiv:`1307.1907 [hep-ex]`.

[118]A. H. Hoang and M. Stahlhofen, "The Top-Antitop Threshold at the ILC: NNLL QCD Uncertainties", JHEP **1405**, 121 (2014), arXiv:`1309.6323 [hep-ph]`.

[119]M. Martinez and R. Miquel, "Multiparameter fits to the $t\bar{t}$ threshold observables at a future e+ e- linear collider", Eur. Phys. J. **C27**, 49–55 (2003), arXiv:`hep-ph/0207315 [hep-ph]`.

[120]T. Horiguchi, A. Ishikawa, T. Suehara, K. Fujii, Y. Sumino, et al., "Study of top quark pair production near threshold at the ILC", (2013), arXiv:`1310.0563 [hep-ex]`.

[121]K. Seidel, F. Simon, M. Tesar, and S. Poss, "Top quark mass measurements at and above threshold at CLIC", Eur. Phys. J. **C73**, 2530 (2013), arXiv:`1303.3758 [hep-ex]`.

[122]W. Bernreuther and Z.-G. Si, "Top quark and leptonic charge asymmetries for the Tevatron and LHC", Phys. Rev. **D86**, 034026, 034026 (2012), arXiv:`1205.6580 [hep-ph]`.

[123]W. Bernreuther and Z.-G. Si, "Distributions and correlations for top quark pair production and decay at the Tevatron and LHC", Nucl. Phys. **B837**, 90–121 (2010), arXiv:`arXiv:1003.3926 [hep-ph]`.

[124]W. Hollik and D. Pagani, "The electroweak contribution to the top quark forward-backward asymmetry at the Tevatron", Phys.Rev. **D84**, 093003 (2011), arXiv:`1107.2606 [hep-ph]`.

[125]V. Ahrens, A. Ferroglia, M. Neubert, B. D. Pecjak, and L. L. Yang, "The top-pair forward-backward asymmetry beyond NLO", Phys.Rev. **D84**, 074004 (2011), arXiv:`1106.6051 [hep-ph]`.

[126]J. H. Kuhn and G. Rodrigo, "Charge asymmetries of top quarks at hadron colliders revisited", JHEP **1201**, 063 (2012), arXiv:`1109.6830 [hep-ph]`.

[127]L. G. Almeida, G. F. Sterman, and W. Vogelsang, "Threshold Resummation for the Top Quark Charge Asymmetry", Phys.Rev. **D78**, 014008 (2008), arXiv:0805.1885 [hep-ph].

[128]J. H. Kuhn and G. Rodrigo, "Charge asymmetry of heavy quarks at hadron colliders", Phys.Rev. **D59**, 054017 (1999), arXiv:hep-ph/9807420 [hep-ph].

[129]P. Ferrario and G. Rodrigo, "Massive color-octet bosons and the charge asymmetries of top quarks at hadron colliders", Phys.Rev. **D78**, 094018 (2008), arXiv:0809.3354 [hep-ph].

[130]P. Ferrario and G. Rodrigo, "Constraining heavy colored resonances from top-antitop quark events", Phys.Rev. **D80**, 051701 (2009), arXiv:0906.5541 [hep-ph].

[131]O. Antunano, J. H. Kuhn, and G. Rodrigo, "Top quarks, axigluons and charge asymmetries at hadron colliders", Phys. Rev. **D77**, 014003 (2008), arXiv:arXiv:0709.1652 [hep-ph].

[132]P. H. Frampton, J. Shu, and K. Wang, "Axigluon as Possible Explanation for $p\bar{p} \to t\bar{t}$ Forward-Backward Asymmetry", Phys.Lett. **B683**, 294–297 (2010), arXiv:0911.2955 [hep-ph].

[133]D.-W. Jung, P. Ko, J. S. Lee, and S.-h. Nam, "Model independent analysis of the forward-backward asymmetry of top quark production at the Tevatron", Phys.Lett. **B691**, 238–242 (2010), arXiv:0912.1105 [hep-ph].

[134]A. Arhrib, R. Benbrik, and C.-H. Chen, "Forward-backward asymmetry of top quark in diquark models", Phys.Rev. **D82**, 034034 (2010), arXiv:0911.4875 [hep-ph].

[135]A. Djouadi, G. Moreau, F. Richard, and R. K. Singh, "The forward-backward asymmetry of top quark production at the Tevatron in warped extra dimensional models", Phys. Rev. **D82**, 071702 (2010), arXiv:arXiv:0906.0604 [hep-ph].

[136]E. Alvarez, L. Da Rold, J. I. S. Vietto, and A. Szynkman, "Phenomenology of a light gluon resonance in top-physics at Tevatron and LHC", JHEP **1109**, 007 (2011), arXiv:1107.1473 [hep-ph].

[137]C.-H. Chen, G. Cvetic, and C. Kim, "Forward-backward asymmetry of top quark in unparticle physics", Phys.Lett. **B694**, 393–397 (2011), arXiv:1009.4165 [hep-ph].

[138]D.-W. Jung, P. Ko, and J. S. Lee, "Longitudinal top polarization as a probe of a possible origin of forward-backward asymmetry of the top quark at the Tevatron", Phys.Lett. **B701**, 248–254 (2011), arXiv:1011.5976 [hep-ph].

[139]J. Aguilar-Saavedra and M. Perez-Victoria, "Shaping the top asymmetry", Phys.Lett. **B705**, 228–234 (2011), arXiv:1107.2120 [hep-ph].

[140]G. Marques Tavares and M. Schmaltz, "Explaining the t-tbar asymmetry with a light axigluon", Phys.Rev. **D84**, 054008 (2011), arXiv:1107.0978 [hep-ph].

[141]R. Barcelo, A. Carmona, M. Masip, and J. Santiago, "Stealth gluons at hadron colliders", Phys.Lett. **B707**, 88–91 (2012), arXiv:1106.4054 [hep-ph].

[142]K. Cheung, W.-Y. Keung, and T.-C. Yuan, "Top Quark Forward-Backward Asymmetry", Phys.Lett. **B682**, 287–290 (2009), arXiv:0908.2589 [hep-ph].

[143]B. Xiao, Y.-k. Wang, and S.-h. Zhu, "Forward-backward Asymmetry and Differential Cross Section of Top Quark in Flavor Violating Z' model at $\mathcal{O}(\alpha_s^2\alpha_X)$", Phys.Rev. **D82**, 034026 (2010), arXiv:1006.2510 [hep-ph].

[144]Q.-H. Cao, D. McKeen, J. L. Rosner, G. Shaughnessy, and C. E. Wagner, "Forward-Backward Asymmetry of Top Quark Pair Production", Phys.Rev. **D81**, 114004 (2010), arXiv:1003.3461 [hep-ph].

[145]S. Jung, H. Murayama, A. Pierce, and J. D. Wells, "Top quark forward-backward asymmetry from new t-channel physics", Phys.Rev. **D81**, 015004 (2010), arXiv:0907.4112 [hep-ph].

[146]J. Cao, Z. Heng, L. Wu, and J. M. Yang, "Top quark forward-backward asymmetry at the Tevatron: A Comparative study in different new physics models", Phys.Rev. **D81**, 014016 (2010), arXiv:0912.1447 [hep-ph].

[147]V. Barger, W.-Y. Keung, and C.-T. Yu, "Asymmetric Left-Right Model and the Top Pair Forward-Backward Asymmetry", Phys.Rev. **D81**, 113009 (2010), arXiv:1002.1048 [hep-ph].

[148]P. Ko, Y. Omura, and C. Yu, "Top Forward-Backward Asymmetry and the CDF Wjj Excess in Leptophobic $U(1)'$ Flavor Models", Phys.Rev. **D85**, 115010 (2012), arXiv:1108.0350 [hep-ph].

[149]P. Ko, Y. Omura, and C. Yu, "Chiral U(1) flavor models and flavored Higgs doublets: The Top FB asymmetry and the Wjj", JHEP **1201**, 147 (2012), arXiv:1108.4005 [hep-ph].

[150]P. Ko, Y. Omura, and C. Yu, "Top A_{FB} at the Tevatron vs. Charge Asymmetry at the LHC in Chiral U(1) Flavor Models with Flavored Higgs Doublets", Eur.Phys.J. **C73**, 2269 (2013), arXiv:1205.0407 [hep-ph].

[151]M. Bauer, F. Goertz, U. Haisch, T. Pfoh, and S. Westhoff, "Top-Quark Forward-Backward Asymmetry in Randall-Sundrum Models Beyond the Leading Order", JHEP **1011**, 039 (2010), arXiv:1008.0742 [hep-ph].

[152]R. S. Chivukula, E. H. Simmons, and C.-P. Yuan, "Axigluons cannot explain the observed top quark forward-backward asymmetry", Phys.Rev. **D82**, 094009 (2010), arXiv:1007.0260 [hep-ph].

[153]I. Dorsner, S. Fajfer, J. F. Kamenik, and N. Kosnik, "Light colored scalars from grand unification and the forward-backward asymmetry in t t-bar production", Phys.Rev. **D81**, 055009 (2010), arXiv:0912.0972 [hep-ph].

[154]J. Shu, T. M. Tait, and K. Wang, "Explorations of the Top Quark Forward-Backward Asymmetry at the Tevatron", Phys.Rev. **D81**, 034012 (2010), arXiv:0911.3237 [hep-ph].

[155]J. Aguilar-Saavedra and M. Perez-Victoria, "Simple models for the top asymmetry: Constraints and predictions", JHEP **1109**, 097 (2011), arXiv:1107.0841 [hep-ph].

[156]V. M. Abazov et al., "Forward-backward asymmetry in top quark-antiquark production", Phys.Rev. **D84**, 112005 (2011), arXiv:1107.4995 [hep-ex].

[157]T. Aaltonen et al., "Evidence for a Mass Dependent Forward-Backward Asymmetry in Top Quark Pair Production", Phys.Rev. **D83**, 112003 (2011), arXiv:1101.0034 [hep-ex].

[158]A. Falkowski, M. L. Mangano, A. Martin, G. Perez, and J. Winter, "Data driving the top quark forward–backward asymmetry with a lepton-based handle", Phys.Rev. **D87**, 034039 (2013), arXiv:1212.4003 [hep-ph].

[159]S. Frixione and B. R. Webber, "Matching NLO QCD computations and parton shower simulations", JHEP **06**, 029 (2002), arXiv:hep-ph/0204244.

[160]T. Aaltonen et al., "Measurement of the top quark forward-backward production asymmetry and its dependence on event kinematic properties", Phys.Rev. **D87**, 092002 (2013), arXiv:1211.1003 [hep-ex].

[161]V. M. Abazov et al., "Measurement of the forward-backward asymmetry in top quark-antiquark production in ppbar collisions using the lepton+jets channel", Phys.Rev. **D90**, 072011 (2014), arXiv:1405.0421 [hep-ex].

[162]M. Czakon, P. Fiedler, and A. Mitov, "Resolving the Tevatron top quark forward-backward asymmetry puzzle", (2014), arXiv:1411.3007 [hep-ph].

[163]"Combination of ATLAS and CMS $t\bar{t}$ charge asymmetry measurements using LHC proton-proton collisions at $\sqrt{s} = 7$ TeV", (2014).

[164]J. Aguilar-Saavedra, D. Amidei, A. Juste, and M. Perez-Victoria, "Asymmetries in top quark pair production", (2014), arXiv:1406.1798 [hep-ph].

[165]C. Collaboration, "Measurement of the ttbar charge asymmetry with lepton+jets events at 8 TeV", (2013).

[166]ATLAS collaboration, "Measurement of the top quark pair production charge asymmetry in proton-proton collisions at $sqrts = 7$ TeV using the ATLAS detector", (2013).

[167]T. A. Aaltonen et al., "Measurement of the leptonic asymmetry in $t\bar{t}$ events produced in $p\bar{p}$ collisions at $\sqrt{s} = 1.96$ TeV", Phys. Rev. **D88**, 072003 (2013), arXiv:1308.1120 [hep-ex].

[168]T. Aaltonen et al., (2011), eprint: CDFnote10436.

[169]T. A. Aaltonen et al., "Measurement of the inclusive leptonic asymmetry in top-quark pairs that decay to two charged leptons at CDF", Phys.Rev.Lett. **113**, 042001 (2014), arXiv:1404.3698 [hep-ex].

[170]V. M. Abazov et al., "Measurement of the forward-backward asymmetry in the distribution of leptons in $t\bar{t}$ events in the lepton+jets channel", Phys.Rev. **D90**, 072001 (2014), arXiv:1403.1294 [hep-ex].

Conclusion

In this manuscript I describe my research in the D0 experiment.

My contribution to the operation of the D0 detector and data taking consisted in the operation of the D0 calorimeter, development of the calorimeter on-line and off-line monitoring software with the automatic identification of hardware problems and presence of external noise. Studies of different sources of data quality problems in the calorimeter allowed me to identify several sources of noise and develop the corresponding identification algorithms for the following failures: rings of fire, hot cells, hot towers, coherent pedestal shifts in ADC, missing crates, noon noise. I contributed to the development of the D0 wide strategy for the data quality improvement and of the procedure for selecting the data with good quality and to the development of a corresponding software. As a result of these efforts D0 improved the fraction of lost data due to calorimeter problems from 10% in the beginning of the data taking to 2–3% in the end of data taking. For all subsystems combined, the improvement is going from 15% to 5%. This corresponds to about 715 pb^{-1} of recovered integrated luminosity, or about 6 months of Tevatron running at the end of the data taking period.

One more contribution to the D0 experiment was the work on the off-line processing of the collected data, data preparation for the different D0 analyses, contribution to development of common analysis framework and development of common analysis tools. These framework and tools were used for most of the analyses since 2007 and allowed to provide certified selections and MC corrections with well established uncertainties, tools for MC studies and data processing. I also provided a D0 wide user support for the analysis framework for many years. I coordinated the common analysis activity as a convener of the common samples group in 2007—2009 and the V+jets group in 2009—2010.

For many years I carried out a study of the top quark in the D0 experiment. My personal contributions focused mainly on the precision measurements of the top quark properties in the dilepton final state, but I also participated in many other measurements via discussions, analysis reviews, definition of the strategies for the measurements as a top group convener (2011 – 2014). I participated in the measurements of the top pair production cross section in the dilepton final state, started from the analysis with an integrated luminosity of 425 pb^{-1} and a precision of the 23%. The most recent measurement used an integrated luminosity of 5.4 pb^{-1} and achieved a precision of 12%. Combination with the lepton+jets final state, allowed to reach a precision of 8% and combination with the CDF experiment reduced the uncertainty on the $t\bar{t}$ production cross section measurement to 5.4%. The combination of lepton+jet and dileptons finals states has been used to search for a charged Higgs boson and measurement of the ratio of the branching fractions $R = \mathcal{B}(t \to Wb)/\mathcal{B}(t \to Wq)$ achieved a precision of 0.04, still the most precise measurement of this quantity at D0. The measurement of the mass of the top quark in the dilepton final state uses the most precise technique, the matrix element method, and reached a precision of 1.4%. My contribution to this technique allowed to speed-up the calculation by a factor of 100 and is still used for analyses of the full available D0 data

set, currently on-going. For the first time, we adapted the matrix element technique to the differential measurement, in particular, for the measurement of the $t\bar{t}$ asymmetry with 9.7 fb^{-1}. This measurement has a precision of about 7% and is the only measurement in D0 of this quantity in the dilepton final state. I contributed also to the measurements of the asymmetry of the distribution of leptons in the $t\bar{t}$ dilepton final state. These two asymmetry measurements, as well as two D0 measurements in the lepton+jet final state, are in good agreement with the most up-to-date theoretical predictions and resolve the long standing puzzle of the asymmetry in the top quark pair production.

I am participating in several other measurements with the full D0 statistics, currently in internal D0 review. We expect to be able to publish soon the spin correlation measurement in the dilepton and lepton+jets final states, the measurement of the top quark mass in the dilepton channel and the measurement of the $t\bar{t}$ production cross section in the dilepton and lepton+jets final states. Those measurements will end the top quark program at D0, but the top quark studies is continuing at the LHC experiments and, in the future, will be continued by the currently discussed e^+e^- collider(s).